CO_2 DISPLACEMENT MECHANISMS: PHASE EQUILIBRIA EFFECTS AND CARBON DIOXIDE SEQUESTRATION STUDIES

by

Sangeetha M. Pasala

A dissertation submitted to the faculty of
The University of Utah
in partial fulfillment of the requirements for the degree of

Doctor of Philosophy

Department of Chemical Engineering

The University of Utah

December 2010

The University of Utah Graduate School

STATEMENT OF DISSERTATION APPROVAL

The dissertation of **Sangeetha M. Pasala**

has been approved by the following supervisory committee members:

Milind D. Deo	, Chair	**07/08/2010** Date Approved
Craig B. Forster	, Member	**05/23/2005** Date Approved
JoAnn S. Lighty	, Member	**05/23/2005** Date Approved
Richard Peterson	, Member	**05/23/2005** Date Approved
William T. Parry	, Member	Date Approved

and by **JoAnn S. Lighty**, Chair of the Department of **Department of Chemical Engineering**

and by Charles A. Wight, Dean of The Graduate School.

ABSTRACT

Supercritical carbon dioxide is injected into underground formations to enhance oil recovery and for subsurface sequestration to minimize the impact of CO_2 emissions due to global warming. The complex phase behavior of CO_2 with oil determines the effectiveness of the CO_2 injection for enhanced oil recovery. The injection of CO_2 into the subsurface is also affected by the large and small scale heterogeneities in the formations. These two aspects of CO_2 injection are examined in this research.

Development of multiple-contact miscibility is important in the success of a carbon dioxide enhanced oil recovery. CO_2 displacements are often designed to operate above the minimum miscibility pressure (MMP) to ensure the development of multiple contact miscibility between the oil and CO_2. Compositional histories in different parts of a two-dimensional domain are examined in this study in relation to displacement pressure employed.

The second part of this dissertation deals with the effect of faults on the CO_2 sequestration process and on the integrity of storage. Outcrop-based studies of faulted, aeolian Navajo sandstone provide detailed, quantitative insight regarding the range of fault characteristics that might be encountered as injected CO_2 migrates through the faulted aquifer.

Faults can act as barriers, conduits, or integrated barrier-conduit systems. Uncertainty in knowing whether a subsurface fault will act as a barrier or conduit leads to uncertainty in evaluating the likelihood for economically sequestering CO_2 in sandstone aquifers.

Eclipse® black oil reservoir simulator is used to explore how different, 3-D, fault-related permeability/porosity structures might impact CO_2 injection into, migration through, and leakage from a sequestration aquifer. Sandstone permeability

values range from 10s to 1000s of mD. Simulator output shows how fault conduits and barriers can restrict migration of CO_2 through the aquifer as a consequence of bypassing (conduits) or compartmentalization (barriers). In addition, the simulation results reveal how the geoscientists' ability to quantify and discriminate between high-permeability versus low-permeability faults in sandstone aquifers can play an important role in designing CO_2 sequestration operations.

Dedicated to my parents,

and

my husband,

for their endless love

CONTENTS

ABSTRACT . . . . . **iii**

LIST OF FIGURES . . . . . **ix**

LIST OF TABLES . . . . . **xii**

ACKNOWLEDGEMENTS . . . . . **xiii**

CHAPTERS

1. INTRODUCTION **1**

1.1 Miscibility and compositional effects in carbon dioxide flooding 2
1.2 CO_2 injection for carbon sequestration 3

2. MISCIBILITY AND COMPOSITIONAL EFFECTS IN CO_2 FLOODING **5**

2.1 Previous efforts to simulate miscibility and compositional effects in CO_2 flooding 6
2.2 Carbon dioxide flooding 7
2.3 Phase behavior of oil and carbon dioxide 7
2.4 Approach 9

3. COMPOSITIONAL RESERVOIR SIMULATIONS **11**

3.1 Setting up the reservoir simulator: one-dimensional simulations 11
3.2 Two-dimensional simulations 12
3.3 Simulation analysis 13
3.3.1 Normalized compositional profiles 13
3.3.2 Compositional path along the length of the reservoir 14
3.4 Three component one-dimensional simulations results 14
3.5 Three component two-dimensional simulation results 18
3.6 Thirteen component one-dimensional simulation results 22
3.7 Thirteen component two-dimensional simulation results 23
3.8 Composition path along the length of the reservoir 28
3.9 Water Alternating Gas injection studies - Introduction 30

3.10 Thirteen component two-dimensional WAG simulations 30
3.11 Simulation analysis 31
3.12 Composition path along the length of the reservoir for WAG simulations 33

4. CO_2 INJECTION FOR CARBON SEQUESTRATION 34

4.1 Previous efforts to simulate subsurface CO_2 injection for CO_2 sequestration 34
4.2 Approach 35

5. PROPERTIES OF RESERVOIR ROCK 37

5.1 Aeolian Navajo sandstone properties 37
5.2 Properties of fault affected rocks 39

6. ESTIMATING PETROPHYSICAL PROPERTIES FOR RESERVOIR GRID BLOCKS 41

6.1 Permeability and porosity 41
6.2 Relative permeability and capillary pressures relationships 45

7. SETTING UP THE RESERVOIR SIMULATOR 51

7.1 Horizontal injection wells 54
7.2 Stacked reservoirs with intervening, horizontal seal 54
7.3 Large reservoir model 55
7.4 Reservoir fluid properties 55

8. RESERVOIR SIMULATION RESULTS 58

8.1 High and low permeability faults without seal 58
8.2 Horizontal well injection studies 64
8.3 Stacked reservoirs with intervening, horizontal seal 66
8.4 Low permeability sandstone reservoir 71
8.5 Impact of relative permeability relationships 73
8.6 Impact of permeability anisotropy within the fault zone 75
8.6.1 Homogeneous, anisotropic fault zone permeability 75
8.6.2 Conduit barrier faults 77
8.7 Larger reservoir model 82

9. DISCUSSION 87

10. CONCLUSIONS **91**
10.1 Phase equilibria effects 91
10.2 CO_2 sequestration 92
REFERENCES **94**

LIST OF FIGURES

3.1 Normalized compositions of C_4 and C_{10} at 1500 psia in one-dimensional system. 14

3.2 Normalized compositions of C_4 and C_{10} at 1700 psia in one-dimensional system. 15

3.3 Normalized compositions of C_4 and C_{10} at 1900 psia in one-dimensional system. 16

3.4 Recovery plots at 1500, 1700, 1900 psia for one-dimensional system . . 17

3.5 Normalized compositions of C_4 and C_{10} in the top layer at 1500 psia in two-dimensional system. 19

3.6 Normalized compositions of C_4 and C_{10} in the middle layer at 1500 psia in two-dimensional system. 19

3.7 Normalized compositions of C_4 and C_{10} in the bottom layer at 1500 psia in two-dimensional system. 20

3.8 Normalized compositions of C_4 and C_{10} in the top layer at 1900 psia in two-dimensional system. 20

3.9 Normalized compositions of C_4 and C_{10} in the middle layer at 1900 psia in two-dimensional system. 21

3.10 Normalized compositions of C_4 and C_{10} in the bottom layer at 1900 psia in two-dimensional system. 21

3.11 Normalized compositions at 1500 psia in one-dimensional system. 23

3.12 Normalized compositions at 2500 psia in one-dimensional system. 24

3.13 Normalized compositions at 3500 psia in one-dimensional system. 24

3.14 Recovery plots at 1500, 2500, 3500 psia for one-dimensional system . . 25

3.15 Normalized compositions in the top layer at 1500 psia in two-dimensional system. 25

3.16 Normalized compositions in the middle layer at 1500 psia in two-dimensional system. 26

3.17 Normalized compositions in the bottom layer at 1500 psia in two-dimensional system. 26

3.18 Normalized compositions in the top layer at 3500 psia in two-dimensional system. 27

3.19 Normalized compositions in the middle layer at 3500 psia in two-dimensional system. 27
3.20 Normalized compositions in the bottom layer at 3500 psia in two-dimensional system. 28
3.21 Recovery plots at 1500 and 3500 psia for two-dimensional system 29
3.22 Composition trajectory at 1900 psia in the bottom layer. 29
3.23 Normalized compositions of the top layer at 3500 psia. 31
3.24 Normalized compositions of the middle layer at 3500 psia. 32
3.25 Normalized compositions of the bottom layer at 3500 psia. 32
3.26 Composition trajectory at 1900 psia in the bottom layer. 33
5.1 Typical arrangements of deformation-induced features in faulted sandstone. Arrows show direction of fault slip. Black features are individual/amalgamated deformation bands. White features are open fractures. 38
6.1 Variation in equivalent porosity and permeability of a $1m^3$ rock block for two different host rocks as low-k deformation bands (DBs: ϕ = 0.07, k = 500 mD, 1 mm thick) and high-k fractures (Fracs: aperture = 0.1 mm) are added. The upper line is for host k of 500mD and porosity of 25%. The lower line is for host k of 50 mD and ϕ = 0.15. 'DB' identifies deformation bands and ' Frac' identifies fractures. 44
6.2 Porosity-Permeability relationship for the 500md host rock 46
6.3 Relative permeability curve for the host rock 48
6.4 Relative permeability curve for a fracture-filled fault 49
6.5 Relative permeability curve for a deformation band filled fault 50
7.1 Top and front view of the reservoir simulation volume 53
7.2 Front view of the reservoir simulator set-up in the reservoir with horizontal injector wells case 54
7.3 Front view of the reservoir simulator set-up in the reservoir with horizontal seal case 55
7.4 Top and front view of the large reservoir simulation model 56
8.1 Dissolved CO_2 distribution after 100 days of low k, no fault, and high k fault. 59
8.2 Free CO_2 distribution after 100 days of low k, no fault, and high k fault. 60
8.3 Dissolved CO_2 distribution after 500 days of low k, no fault, and high k fault. 60
8.4 Free CO_2 distribution after 500 days of low k, no fault, and high k fault. 61

8.5 Dissolved and Free CO_2 distribution for Zone-1 of the reservoir where, 'Frac' = Fractures , 'DB' = Deformation bands, and 'Unf.' = Unfaulted 62

8.6 Bottom Hole Pressure of low k, no fault, and high k fault. 64

8.7 Dissolved and Free CO2 distribution for Zone-1 of the reservoir in a deformation band fault case where, 'Hor' = Horizontal Wells, 'Diss' = Dissolved Gas , and 'Ver' = Vertical Wells 65

8.8 Bottom Hole Pressure (BHP) Distribution in the deformation band fault case where 'Ver' = Vertical and 'Hor' = Horizontal 65

8.9 Dissolved CO2 distribution in a stacked reservoir system after 100 days for a deformation band fault case. 67

8.10 Dissolved CO2 distribution in a stacked reservoir system after 500 days for a deformation band fault case. 68

8.11 Dissolved CO2 distribution in a stacked reservoir system after 100 days for a fractured fault case. 69

8.12 Dissolved CO2 distribution in a stacked reservoir system after 500 days for a fractured fault case. 70

8.13 Volume of CO2 sequestered in the top, middle, and bottom layers in a deformation band, and a fractured fault case. 70

8.14 Total (Dissolved and Free) CO2 distribution for Zone-1 of the reservoir 72

8.15 Dissolved and Free CO2 distribution in zone-1 for a deformation band and a fractured filled fault scenario where 'Diss' = Dissolved Gas for both single and multiple relative permeability curves. 74

8.16 Dissolved and Free CO2 distribution for Zone-1 of the reservoir for the isotropic and the two anisotropic cases in a deformation band fault where, 'Aniso'= Anisotropic , 'Iso' = Isotropic, and 'Diss.' = Dissolved 77

8.17 Conduit-Baffle fault 78

8.18 Reservoir model design 79

8.19 Dissolved CO2 distribution after 100 days 81

8.20 Dissolved CO2 distribution after 500 days 82

8.21 Dissolved and Free CO2 distribution in zone-1 of the reservoir volume where 'Diss'=Dissolved, 'H-L-H' = High-Low-High Fault Case, and 'Equi'=Equivalent Permeability Case 83

8.22 Dissolved CO_2 distribution after 11 years 84

8.23 Dissolved CO_2 distribution after 30 years 85

8.24 Free CO_2 saturation after 11 years. 85

8.25 Free CO_2 saturation after 30 years. 86

LIST OF TABLES

3.1 Percentage recovery and displacement mechanisms at different pressures, where IMM - Immiscible, MCM - Multiple Contact Miscible, and FCM - First Contact Miscible 17

6.1 Isotropic grid block permeability and porosity of a 1m cube with increasing deformation band where, V = Volume, Ints = intersections, n = porosity, am = arithmetic mean, and hm = harmonic mean. 43

6.2 Isotropic grid block permeability and porosity of a 1m cube with increasing fractures where, V = Volume, Ints = intersections, n = porosity, am = arithmetic mean, and hm = harmonic mean. 43

8.1 Permeability and Porosity properties in the three cases where md = milli Darcy. 59

8.2 Dissolved and Free Gas in DB filled faults, fractured filled faults, and the Unfaulted case for Zone-1 where 'Ttl'=total, 'Diss'=dissolved. . . . 62

8.3 Dissolved and Free Gas in 5md and 500md host rock cases for Zone-1 where 'Ttl'=total, 'Diss'=dissolved 72

8.4 Dissolved and Free gas in zone-1 for a fracture-filled fault with single and multiple relative permeability curves where 'Ttl'=Total and 'Diss'=Dissolved 73

8.5 Dissolved and Free gas in zone-1 for a deformation band-filled fault with single and multiple relative permeability curves 74

8.6 Permeability and Porosity properties of all the three cases where md = milli Darcy, No. = Number, DBs = Deformation Bands, k = Permeability 76

8.7 Permeability and Porosity properties of the host rock and fault, for the conduit barrier fault case, where md = milli Darcy, k = Permeability 79

8.8 Dissolved and Free gas in Zone-1 of the reservoir volume for the High-Low-High Fault Case, and the Equivalent Permeability Case, where 'Diss'=Dissolved, 'H-L-H' = High-Low-High , 'Equi'=Equivalent, 'k' = Permeability, 'Ttl'=total, 'Diss'=dissolved 81

8.9 Permeability and Porosity properties of the host rock and fault, for the larger reservoir case, where md = milli Darcy, k = Permeability . 83

9.1 Dissolved and Free Gas in zone-1 of the reservoir volume where 'Diss'=Dissolved, 'H-L-H' = High-Low-High Fault Case, 'Equi'=Equivalent Permeability Case, 'ttl'=total. 88

ACKNOWLEDGEMENTS

My deepest, heartfelt gratitude to my advisor and mentor, Prof. Milind D. Deo, for his enormous support during my doctoral studies. He provided me with an abundant amount of opportunities, freedom, and resources, which most graduate students can only dream of. I am thankful to him forever.

My special thanks to Prof. Craig B. Forster for his helpful suggestions and advice. I am also thankful to Dr. William T. Parry for providing experimental data and helpful comments on the thesis. I would also like to acknowledge the committee members for their valuable time.

This work owes its entire existence to my parents, my husband, and my uncle, Appa Rao Rayavarupu, who have given me more love and encouragement than I have ever known. I have no words to express my gratitude towards them.

This work is financially supported by the Office of Basic Energy Science, U. S. Department of Energy under Award Nos. DE-FG03-00ER15042 and DE-FG03-95ER14526.

Special thanks to all my friends and colleagues who have contributed to this work in many useful ways.

CHAPTER 1

INTRODUCTION

Carbon dioxide (CO_2) injection into subsurface geologic formations plays an important role in two applications:

1. Enhanced oil recovery (EOR) from petroleum reservoirs, and
2. Subsurface sequestration of industrially-emitted CO_2 to minimize the impact of CO_2 emissions in global warming.

CO_2 injection has been used as a commercial process for enhanced oil recovery (EOR) since the 1970s. It is estimated that 80% of oil reservoirs worldwide might be suitable for CO_2 injection based on oil recovery criteria alone. Moreover, the process is widely applicable in both sandstone and carbonate formations with a variety of permeabilities and thickness of hydrocarbon bearing zones.

CO_2 injection process is technically challenging for the following reasons:

1. The flow of CO_2 is governed by its phase behavior with the resident fluids; this phase behavior is often very complex, involving multiple liquid and vapor phases.
2. There are complex interactions between flow and phase behavior. For example, the CO_2 -laden phases are often much lighter, tending to migrate upward in the formation. Interactions of gravity and phase behavior can create unexpected recovery patterns. This is true even in homogeneous, geologically simple formations.
3. Geologic complexity adds another dimension to the process. It is challenging to determine flow distributions in an environment comprised of complex faults and fractures.

This work is primarily divided into two sections: miscibility and compositional effects for enhanced oil recovery and sequestration studies.

1.1 Miscibility and compositional effects in carbon dioxide flooding

CO_2 flooding under miscible conditions is an important enhanced oil recovery process. Carbon dioxide is usually not miscible on first contact with the reservoir oil. However, at sufficiently high pressures, CO_2 achieves miscibility with oil for a broad spectrum of reservoirs. Under favorable conditions, the gas will vaporize the low to medium fractions of the reservoir crude. After multiple contacts between the oil and carbon dioxide, a bank of light hydrocarbons and CO_2 will form, and this mixture promotes miscibility between the CO_2 and the remaining crude oil.

Miscible displacement processes, which rely on multiple contacts of injected gas and reservoir oil to develop an in situ solvent, generally have been recognized by the petroleum industry. More recently, CO_2 flooding has advanced to the position of being the most economically attractive of the multiple contact miscibility processes. Knowledge of multiple contact miscible mechanisms will give the petroleum industry a better understanding of the CO_2 process, which in turn will lead to better evaluation and design of enhanced oil recovery.

The understanding of the multiphase, multicomponent flow taking place in any miscible displacement process is essential for successful design of gas-injection projects. Due to complex reservoir geometry and reservoir fluid properties, numerical simulations of the flow processes are usually conducted to obtain such understanding. In principle, compositional simulation could be used to study such problems.

Numerical compositional simulations can be used to help distinguish between the various miscible mechanisms. One of the aims of this study is to develop and distinguish the various miscible displacements using numerical compositional simulations. One-dimensional (1-D) and two-dimensional (2-D) simulations were performed and compared to determine the different miscibility mechanisms and gravity effects. In the first section of this dissertation, an attempt is made to resolve three major issues:

1. Can the generation of miscibility be determined by using numerical simu-

lations during CO_2 flooding? Compositionally, do different portions of the reservoir undergo different types of displacements?

2. Does gravity play a major role on reservoir compositions in 2-D domains? Can the compositional differences be observed by performing numerical experiments?
3. It is known that Water Alternating Gas (WAG) operation improves CO_2 sweep efficiency in 2-D simulations. Does WAG injection have a significant improvement on the compositional profiles in two- and three-dimensional displacements?

Compositional simulations combined with detailed analysis can lead to better understanding of the generation of miscibility.

1.2 CO_2 injection for carbon sequestration

Sequestration of CO_2 in deep geological formations is an important application of CO_2 injection operations. Despite uncertainty in estimating the impact of CO_2 emissions on future climate, general scientific consensus holds that CO_2 emissions should be minimized. One element of a multifaceted strategy for limiting CO_2 emissions is to sequester CO_2 in geologic formations. CO_2 can be stored in the subsurface as (1) a dissolved constituent in naturally occurring ground water, (2) free CO_2 in the pore spaces of reservoir rock, and (3) mineral precipitates produced by chemical reactions [1], [2], [3], [4], [5], [6], [7]. The process of collecting the CO_2 at a point source (e.g., a power plant or gas field production well), transporting it to a well site, and injecting it into a subsurface reservoir is commercially proven and commercial geologic sequestration has already begun [8].

Deep sequestration of CO_2 in depleted oil and gas fields, or deep aquifers, may provide a cost effective, technically feasible method to limit CO_2 emissions. The volume available for storage depends on the reservoir structure, rock porosity, and permeability features. Faults with widely varying sizes and fluid flow properties are common features in most rock formations. They can act to impede or enhance fluid flow, thereby playing an important role in reservoir performance. Sequestration

studies are becoming increasingly valuable; therefore, understanding the effect of faults and fractures on storage performance is essential to properly manage CO_2 sequestration. CO_2 storage capacity depends greatly on the presence of faults and/or fractures, since they have a great impact on the fluid flow in the reservoir. Deformation bands can reduce the effective permeability of faulted sandstone by one or more orders of magnitude while fractures can locally enhance the effective permeability of the host sandstone by similar magnitudes. An incomplete understanding of the presence of faults and/or fractures and their impact on reservoir performance may lead to the risk of injected CO_2 leaking into the atmosphere. Incorrectly identifying the rates of injection, pressure buildup in the reservoir, and other factors like fault properties may lead to erroneous estimates of CO_2 storage potential. In some cases, the pressure build up in the reservoir during CO_2 injection may help reservoir managers to detect the presence of faults and appropriately modify their reservoir management strategies.

The research presented in this section combines detailed study of:

1. 3-D numerical simulations used to study the volumes of CO_2 that might be sequestered in different faulted / fractured reservoirs
2. Levels of risk of leakage that may be associated with faulted systems.
3. How the presence/absence, of faults might affect design of CO_2 injection schemes.
4. Evaluating potential pathways for leakage and performing analyses that help to determine the likely physical and chemical behavior of CO_2 introduced to the reservoir-seal system.

Reservoir simulations combined with detailed analysis can lead to better understanding of the overall effect of faults and fractures on sequestration.

CHAPTER 2

MISCIBILITY AND COMPOSITIONAL EFFECTS IN CO_2 FLOODING

CO_2 flooding under miscible conditions is an important and widely used process for enhanced oil recovery throughout the world. The understanding of the multiphase, multicomponent flow taking place in any miscible displacement process is essential for successful design of gas-injection projects. Due to complex reservoir geometry and reservoir fluid properties, numerical simulations of the flow processes are usually conducted to obtain such understanding. In principle, compositional simulation could be used to study such problems.

Carbon dioxide is usually not miscible on first contact with the reservoir oil. However, at sufficiently high pressures, CO_2 achieves miscibility with oil for a broad spectrum of reservoirs. Under favorable conditions, the gas will vaporize the low to medium fractions of the reservoir crude. After multiple contacts between the oil and carbon dioxide, a bank of light hydrocarbons and CO_2 will form, and this mixture promotes miscibility between the CO_2 and the remaining crude oil.

Numerical compositional simulations can be used to help distinguish between the various miscible mechanisms. One of the aims of this study is to develop and distinguish the various miscible displacements using numerical compositional simulations. One-dimensional (1-D) and two-dimensional (2-D) simulations were performed and compared to determine the different miscibility mechanisms and gravity effects. In this dissertation, an attempt is made to resolve three major issues:

1. Can the generation of miscibility be determined by using numerical simulations during CO_2 flooding? Compositionally, do different portions of the

reservoir undergo different types of displacements?

2. Does gravity play a major role on reservoir compositions in 2-D domains? Can the compositional differences be observed by performing numerical experiments?
3. It is known that WAG operation improves CO_2 sweep efficiency in 2-D simulations. Does WAG injection have a significant improvement on the compositional profiles in two- and three-dimensional displacements?

Compositional simulations combined with detailed analysis can lead to better understanding of the generation of miscibility.

A simple three component case, followed by a more complicated multicomponent (thirteen component) system is analyzed for the one- and two-dimensional studies. Normalized Compositional plots are analyzed for these two cases. Simulation results are discussed in detail in Chapter 2. The generation of miscibility was determined by using the compositional profiles from the simulations. One-dimensional and two-dimensional compositional simulations results are compared and analyzed to study the effect of gravity during CO_2 flooding. Water Alternating Gas injection simulations of the thirteen component system are also discussed. Simulated 1-D and 2-D analysis permitted determination of gravity effects in the reservoir. Differences between first contact, multiple contact, and immiscible displacement were examined. WAG injection helps improve sweep efficiency and recovery of miscible or immiscible gas floods where gravity effects are less significant. The proposed research intended to develop a better understanding of the miscibility effects in the reservoir, specifically methods to improve sweep efficiency and recovery.

2.1 Previous efforts to simulate miscibility and compositional effects in CO_2 flooding

Several researchers have used various analyses to describe the CO_2 miscible process. Rathmell [9] reported that a positive indication of an immiscible displacement was the presence of an increase in methane concentration prior to CO_2 breakthrough. When this salting out of methane was stopped by increasing the pressure of the displacement, one could establish the minimum pressure required

for miscibility. Metcalfe and Yarborough [10] have shown experimentally that at least two multiple contact miscible mechanisms - vaporization and condensation can be identified and that the phase equilibria data can be used as a basis for describing the mechanisms. Fluid channeling due to permeability heterogeneity and gravity segregation can be severe in miscible floods because of the high adverse mobility ratios and large density contrasts between injected gas and reservoir oil. K.K. Pande et al. used a compositional simulator to investigate the effect of solvent composition on displacement performance in two-dimensional(x-z) flow where both viscous and gravity forces can cause transverse transport or cross flow of fluids.

2.2 Carbon dioxide flooding

Carbon dioxide is highly soluble in oil and to a lesser extent in water. Carbon dioxide improves oil recovery by the following mechanisms: reduction in crude oil viscosity; swelling of crude oil; reduction in oil density; and miscibility effects. Complete miscibility between the oil and CO_2 or hydrocarbon solvents eliminates interfacial tension and capillary forces and could help recover, in theory, all of the residual oil. When CO_2 and oil are mixed, two physical changes occur, leading to enhanced oil recovery. First, the CO_2-oil mixture has a lower viscosity than the original oil, which makes it easier for the contacted oil to flow in the porous medium. Second, the high solubility of CO_2 in oil causes significant swelling, which means some fluid must migrate because of expansion. Injection of CO_2 into an oil reservoir causes a complicated series of interactions between CO_2, oil, and water. The efficiency with which an injected gas (CO_2) displaces a liquid (Oil / Water) depends strongly on the phase behavior and fluid flow properties of the gas - liquid mixtures.

2.3 Phase behavior of oil and carbon dioxide

The phase behavior of a CO_2-oil system can be very complex. When the injection gas and reservoir oil, mixed in any ratio, form a single phase, they are said to be first contact miscible. First contact miscibility can be achieved only for highly hydrocarbon rich gases, or at very high pressures for lean systems. Carbon dioxide

is not first contact miscible with most reservoir oils even at fairly high operating pressures. CO_2 can develop miscibility through multiple contacts under specific conditions of pressure and temperature and specific oil compositions. Miscibility could be generated by two different mechanisms: (1) The vaporizing gas drive process (VGD) in which the gas phase is enriched through extraction of the light and intermediate fractions of oil. The original oil is in contact with the vapor phase generated from the previous mixture. The vapor phase eventually gets so rich in light and intermediate hydrocarbons that it becomes completely miscible with the reservoir crude. The minimum pressure required to achieve this is called the minimum miscibility pressure (MMP). The CO_2 minimum miscibility pressure (MMP) is an important parameter for screening and selecting reservoirs for the CO_2 injection process. For the highest recovery, a candidate reservoir must be capable of withstanding an average reservoir pressure greater than the CO_2 MMP. Both experimental slim tube measurements and properly interpreted slim tube simulations provide reliable determination of minimum miscibility conditions for a system, without assuming anything about the displacement mechanism or path of developed miscibility. (2) In situ transfer of the intermediate molecular hydrocarbon fraction from the injected gas into the oil can also generate miscible displacement between reservoir oil and hydrocarbon gases. This mechanism of miscibility generation is called condensing gas drive (CGD). Carbon dioxide flooding is typically a VGD process.

As CO_2 is injected into the reservoir rock containing oil and water, components present in the gas dissolve in the oil (and to a much lesser extent in the water), while some components present in the oil transfer to vapor phase. Because these phases have different saturations, they move at different rates under the imposed pressure gradient, and generally, the lower viscosity vapor phase moves ahead and contacts fresh oil in the reservoir. Those phases mix and equilibrium is established again, and new liquid and vapor phases flow ahead, contacting the fluids in the reservoir. This interaction of phase equilibrium and flow causes components to separate as they propagate through the reservoir [11] [12] [13] [14].

Precipitation of solids believed to be asphaltenes is a common problem during carbon dioxide flooding. Precipitation of solids believed to be asphaltenes has been reported at various stages of oil production [15]. Precipitation is almost universal in gas flooding applications but is also observed in the primary production of under-saturated crude oils [16]. Deposited asphaltenes can reduce effective oil mobility by blocking pore throats and adsorbing onto the rock, thus changing the formation wettability from water-wet to oil-wet.

2.4 Approach

In this study, a series of numerical compositional simulations were performed to help distinguish various miscible mechanisms. Numerical simulations of CO_2 injection were performed to distinguish the various miscible displacements. One-dimensional (1-D) and two-dimensional (2-D) simulations were performed and compared to determine the different miscibility mechanisms and gravity effects.

Reservoir rock and fluid properties were determined by literature review, due to lack of appropriate data. A set of simple calculations were performed to calculate the equivalent permeabilities and porosities. Simple averaging methods were used to compute the equivalent porosities and permeabilities. These are discussed in detail in the next section. The CO_2 flood sample at Rangely, Colorado, operated by Chevron Oil Company is used in the project.

The other goal of this project was to gain insight about the compositional behavior of the fluids in the reservoir and the different displacement processes. Several simulations for one-dimensional (1-D) and two-dimensional (2-D) analysis were developed. It was conclusively shown that different portions of the reservoir undergo different types of displacements. This basically showed that the 1-D and 2-D displacements are fundamentally different. Numerical simulations combined with detailed analysis would aid in determining the phase behavior and the displacement mechanisms the reservoir undergoes.

Various one-dimensional (1-D) and two-dimensional (2-D) scenarios were investigated incorporating these fluid flow properties. Two different systems are studied

for the phase behavior analysis. First, a simple three component case is studied in both one and two dimensions. Second, a more complicated multicomponent (thirteen component) system is analyzed for the one- and two-dimensional studies. Compositional profiles for each component were obtained from the simulation output as a function of the hydrocarbon pore volume of CO_2 injected. These profiles were analyzed to determine if different portions of the reservoir undergo different types of displacements and the effect of gravity in 2-D simulations.

This study is then extended to Water Alternating Gas (WAG) injection studies. In order to stabilize the upward trending CO_2 profile, WAG injection studies were performed , where water is injected alternately with CO_2.

CHAPTER 3

COMPOSITIONAL RESERVOIR SIMULATIONS

A compositional simulator, GEM®, developed by the Computer Modeling Group (CMG) was used for all the simulations. GEM®, an efficient, multidimensional, equation-of- state (EOS) compositional simulator, can simulate all the important mechanisms of a miscible gas injection process, i.e., vaporization and swelling of oil, condensation of gas, viscosity and interfacial tension reduction, and the formation of a miscible solvent bank through multiple contacts.

The two different reservoir scenarios for phase behavior effects analyzed in the next sections are:

1. A simple three component system in both one and two dimensions.
2. Secondly, a more complicated multicomponent (thirteen component) system is analyzed for the one- and two-dimensional studies.

3.1 Setting up the reservoir simulator: one-dimensional simulations

A reservoir with a 20 X 1 X 1 Cartesian grid is modeled in all of the one-dimensional studies. The aerial dimension of the reservoir is 60 X 0.0025 feet. The thickness of the reservoir is considered to be 0.0025 feet. The dimensions in y and z directions were considered as small as possible to make the system one-dimensional. A constant porosity of 0.3 and a permeability of 1000 md in all directions were used in the entire reservoir. The pressure was maintained constant at 1500 psia initially along the length of the reservoir bed. Different simulations were run at varying pressures to study various miscibility mechanisms. There were two operating wells in the field. In well I, the injector is opened as a gas injector and never in production.

Well P is the production well for oil production.

For the three component oil system, CO_2 / butane / decane were considered in this study. The initial compositions of CO_2 / NC_4 / NC_{10} were 0.0, 0.40, and 0.60, respectively. The thirteen component oil system consisted of CO_2, CH_4, NC_2, NC_3, NC_5, NC_6, NC_7, FC_{10}, FC_{15}, FC_{20}, FC_{28}, FC_{35}, and FC_{45} components. The initial compositions are 0.0, 0.23, 0.01, 0.01, 0.06, 0.05, 0.03, 0.23, 0.15, 0.12, 0.04, 0.04 and 0.03, respectively. These compositions were obtained from a sample of the Rangely crude oil. Pure CO_2 is injected into the reservoir.

3.2 Two-dimensional simulations

In two-dimensional studies, the reservoir is a 20 X 1 X 5 Cartesian grid. The aerial dimension of the reservoir is 2000 X 1 foot. The thickness of the reservoir is considered to be 150 feet. The 5 layers in the reservoir are divided into 3 parts. This is done to analyze the phase behavior in each layer separately. The first layer is termed as the Top Layer, the third layer is termed as the Middle Layer, and the fifth layer as the Bottom Layer. The initial conditions of the reservoir were also maintained the same as the one-dimensional studies. An effort was made to represent the same reservoir properties for the one- and two-dimensional systems in order to compare both. Similar components and compositions were used for both the three and thirteen component analysis. Pure CO_2 is injected in both the cases.

Three runs with different initial injection pressures but the same dimensions and other initial conditions were considered. These were termed as Run-1, Run-2, and Run-3 with initial injection pressures of 1500psia, 1700psia, and 1900psia, respectively, for the three component simulations. The three runs for the thirteen component system has initial pressures of 1500psia, 2500psia, and 3500psia, respectively. The pressures considered here are higher than the three component systems. Such high pressures were necessary to achieve the miscibility for this composition of the oil. Simulation results were analyzed for the phase behavior and different miscibility displacements.

If CO_2 is completely miscible, i.e., only a single phase is formed over the range

of pressures and temperatures present in the reservoir, then the displacement is said to be first contact miscible (FCM) and the residual oil saturation in a swept zone is theoretically zero. In many cases, however, miscibility is achieved in situ after the carbon dioxide has contacted the oil repeatedly and mass transfer occurs between the injected solvent and the oil in place. These cases are referred to as multiple-contact-miscible (MCM). If miscibility is never achieved for the range of pressures and compositions in a particular displacement, then the displacement is referred to as being immiscible (IMM), although mass transfer still occurs between the flowing phases [11].

3.3 Simulation analysis

The results from the simulations were analyzed for the type of miscibility that took place in the three displacements.

3.3.1 Normalized compositional profiles

Compositional profiles from the simulation results predict the generation of miscibility. Normalized Compositions (Molar composition of the component / Initial molar composition of the component) versus pore volume of the CO_2 injected into the reservoir were plotted. The compositions were normalized (C/C_0) to show the trends more clearly. The compositions in the middle block (the 10th block) of the reservoir is considered for analysis. The GEM simulator generates very large output files of the order of 50,000-100,000 lines. The necessary information, i.e., pore volume of the carbon dioxide injected and the global compositions of each of the components, were extracted from the output files. Basically, the data were stored as global compositions of each component as a function of time for each grid block of the reservoir. The data obtained from the simulator are directly imported into spreadsheets. The molar compositions were then converted to normalized compositions and the required plots were made which can be compared for analysis.

3.3.2 Compositional path along the length of the reservoir

Compositions were examined along the entire length of the reservoir to determine the flow of the components at different time steps. These plots are used to show the compositional path of the injected CO_2 and the hydrocarbons initially in place.

3.4 Three component one-dimensional simulations results

Figure 3.1 shows the normalized compositions of each of the components at 1500 psia, and is termed Run-1. Results of this model were in close agreement with the results of previous experimental studies [10]. It is clear from these figures that the compositional profiles in all three cases are very different. In Run-1, all the

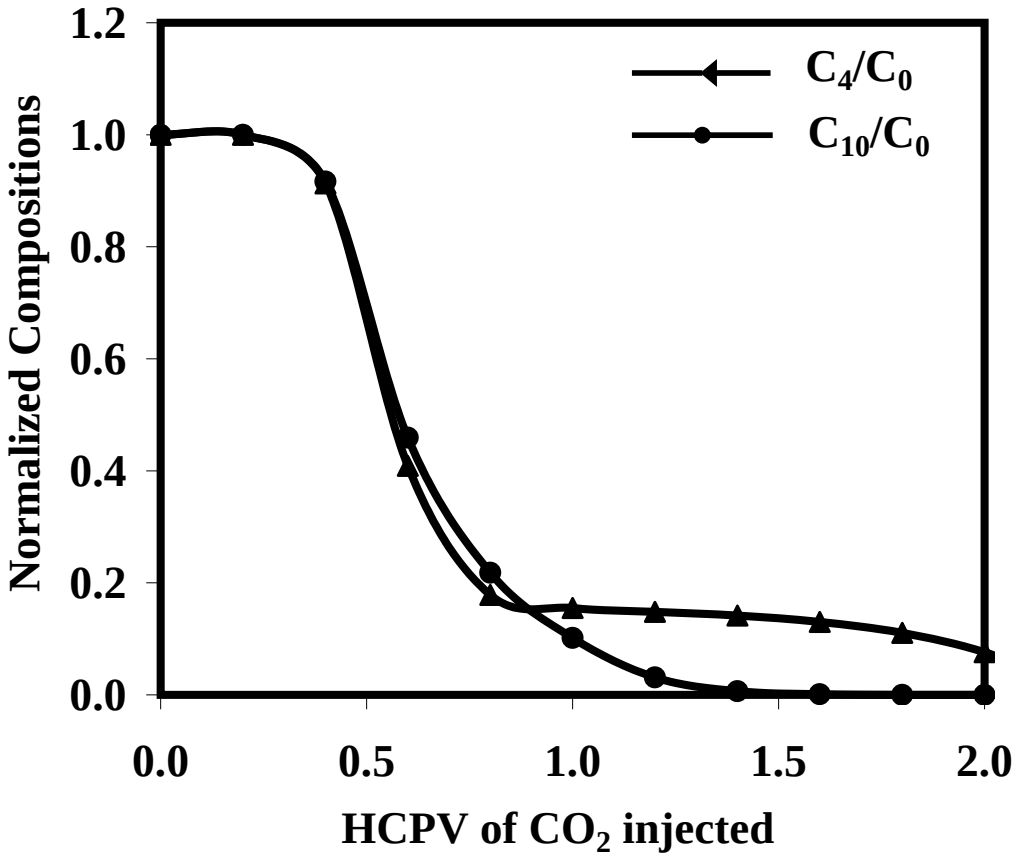

Figure 3.1. Normalized compositions of C_4 and C_{10} at 1500 psia in one-dimensional system.

components of oil are not completely recovered. The lighter component (butane) is recovered completely at 1.4 pore volume(PV) of CO_2 injected. But, not much of the C_{10} is recovered even at pore volumes as high as 2PV of CO_2 injected. An indication of a leading C1 bank can be observed in an immiscible displacement (Run-1). Also, this displacement has a decreased recovery and an increased transition length, which are both indicative of an immiscible displacement.

Figures 3.2 and 3.3 show the normalized compositions of each of the components at 1700, 1900 psia, and are termed as Run-2 and Run-3, respectively. Run-3 shows that all the components of oil including C_{10} are recovered completely at 1PV. Run-3 is a clear indication of first contact miscibility scenario in which all the components of oil are recovered in a single contact. It is clear from these figures

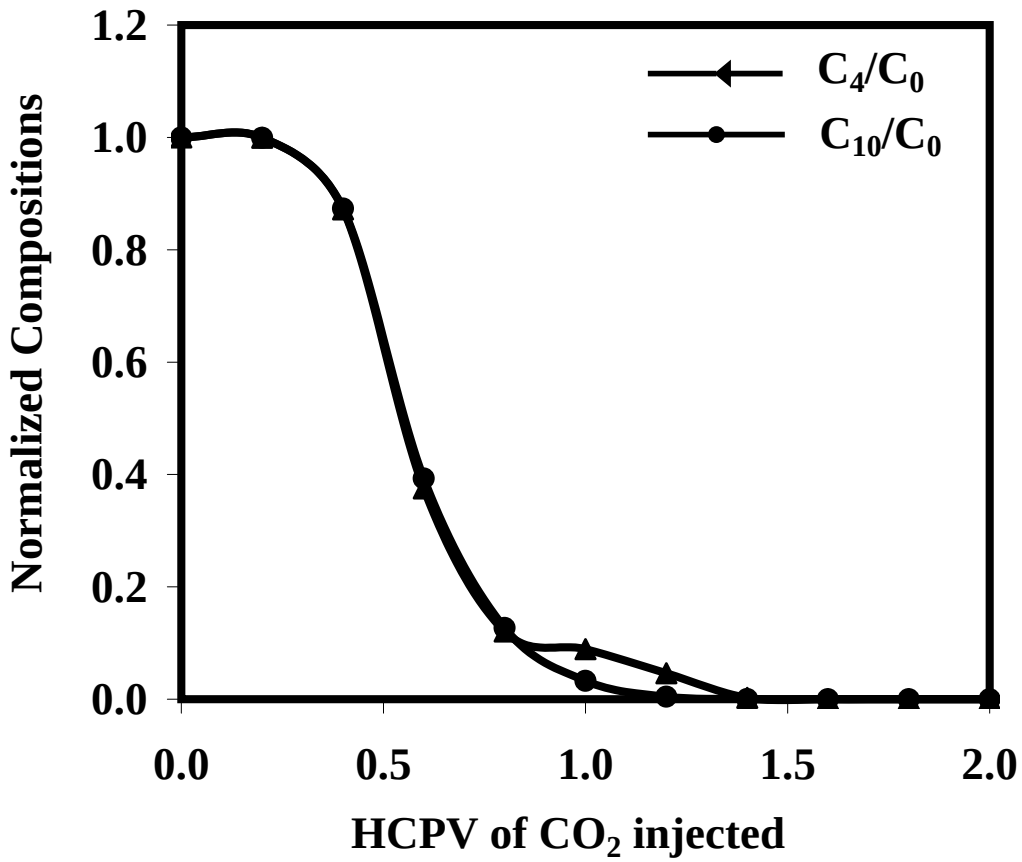

Figure 3.2. Normalized compositions of C_4 and C_{10} at 1700 psia in one-dimensional system.

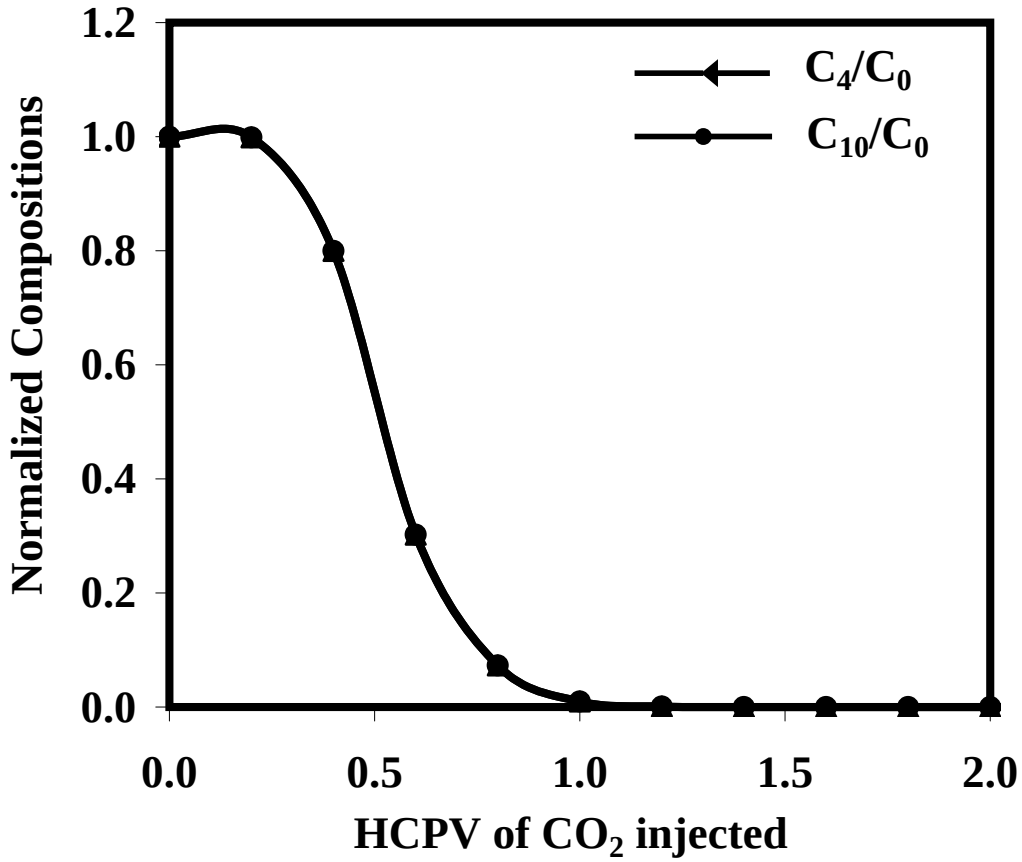

Figure 3.3. Normalized compositions of C_4 and C_{10} at 1900 psia in one-dimensional system.

that as the pressure is decreased, there is a transition from first-contact miscible to multicontact miscible to immiscible displacements.

In Run-3, CO_2 is mixed with the oil and is miscible on first contact. The system pressure is such that only a single-phase fluid results at all combinations of oil and CO_2. Hence, this is a case of first-contact miscible (FCM) displacement. For Run-2, the simulation results reveal a MCM displacement mechanism of the displaced oil. For each displacement, two phases eventually developed in each grid block; upon continued injection into and production from that grid block, the two phases became indistinguishable, i.e., a point of miscibility developed. Table 3.1 shows the simulation runs at different pressures and temperatures, and the corresponding miscibility mechanisms. Figure 3.4 shows the comparison of percentage recovery in

Table 3.1. Percentage recovery and displacement mechanisms at different pressures, where IMM - Immiscible, MCM - Multiple Contact Miscible, and FCM - First Contact Miscible

Run	Pressure(psig)	Temperature(F)	Mechanisms	Recovery (%)
1	1500	160	IMM	86.45
2	1700	160	MCM	92.15
3	1900	160	FCM	93.29

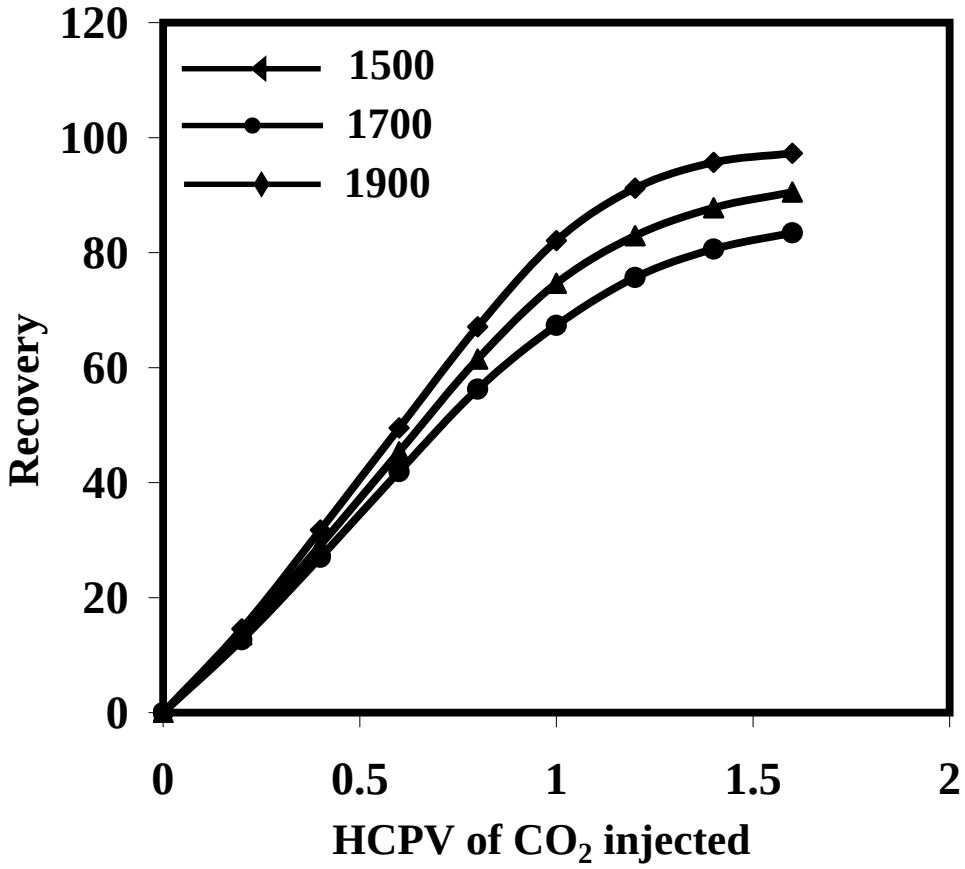

Figure 3.4. Recovery plots at 1500, 1700, 1900 psia for one-dimensional system

all three cases.

The percentage recovery is calculated by dividing the total oil production by the original oil in place (OOIP). Percentage recovery is plotted against the hydrocarbon pore volume of CO_2 injected. This figure clearly illustrates that the FCM system has greater recovery compared to the MCM and the IMM systems, indicating that an IMM is much less efficient. The FCM system has higher pressure compared to the other two scenarios; at higher pressure, CO_2 achieves miscibility with oil and this allows for more recovery.

3.5 Three component two-dimensional simulation results

Figures 3.5, 3.6, 3.7, 3.8, 3.9, and 3.10 show the normalized compositions of each of the oil components in the top, middle, and bottom layers at 1500 psia and 1900 psia. These figures clearly illustrate that the compositional profiles in the three layers are very different. In 2-D simulations, it is observed that the top, middle, and bottom layers have different phase behaviors and compositional profiles. It is clear that at 1900 psia, all the components are recovered completely by 1PV in the top and middle layers, but the bottom layer takes up to 4PV for complete recovery. Firstly, mobility of the fluids is less in the bottom layers. Since CO_2 is a gas, it tends to move upwards and sweep the upper portions of the reservoir. The mobility of the injected CO_2 phase is higher, particularly in the upward direction. Due to gravitational forces, most of the oil flows to the bottom layers and hence a poor distribution of fluids in this layer. Hence, the bottom layer undergoes a different type of displacement compared to the top and middle layers. In order to stabilize the upward trending CO_2 profile, WAG injection studies are performed. This is discussed in detail in the next section.

C_4 is recovered completely from the top portion of the reservoir and not much of it is recovered from the bottom layers. So, what exactly is happening in 2-D simulations? First, the fluid flow in each part of the reservoir is very different. CO_2 is injected constantly into all the layers of the reservoir simultaneously. As CO_2 is injected into the reservoir, most of the oil flows from the top layers to the

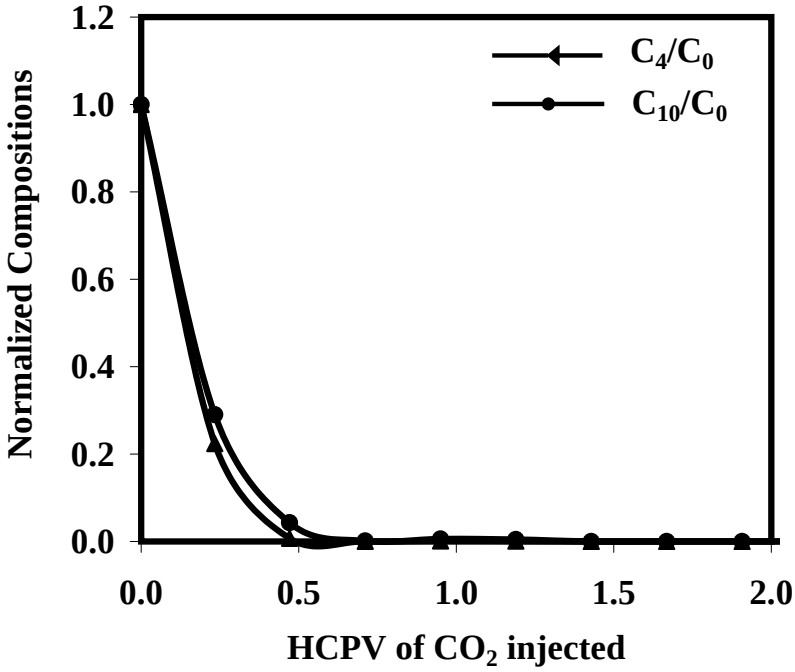

Figure 3.5. Normalized compositions of C_4 and C_{10} in the top layer at 1500 psia in two-dimensional system.

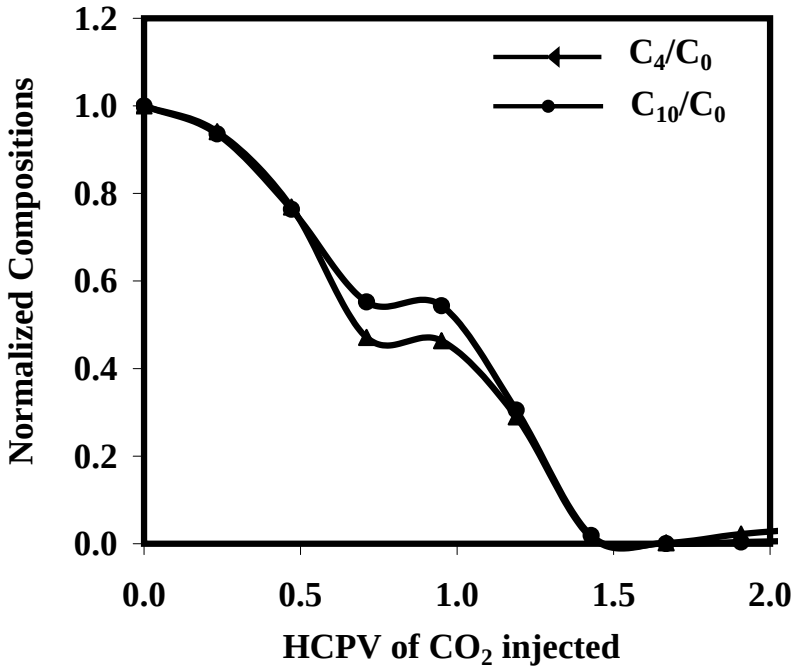

Figure 3.6. Normalized compositions of C_4 and C_{10} in the middle layer at 1500 psia in two-dimensional system.

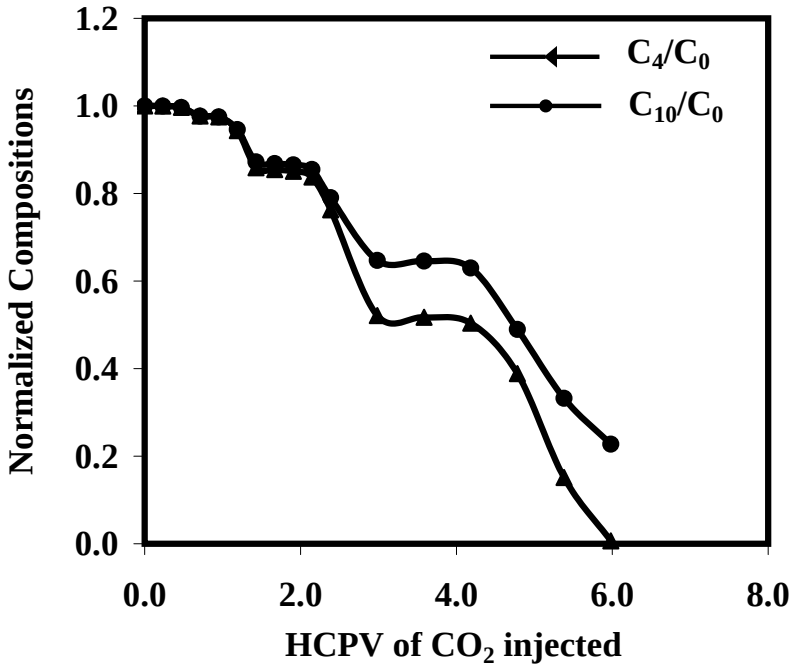

Figure 3.7. Normalized compositions of C_4 and C_{10} in the bottom layer at 1500 psia in two-dimensional system.

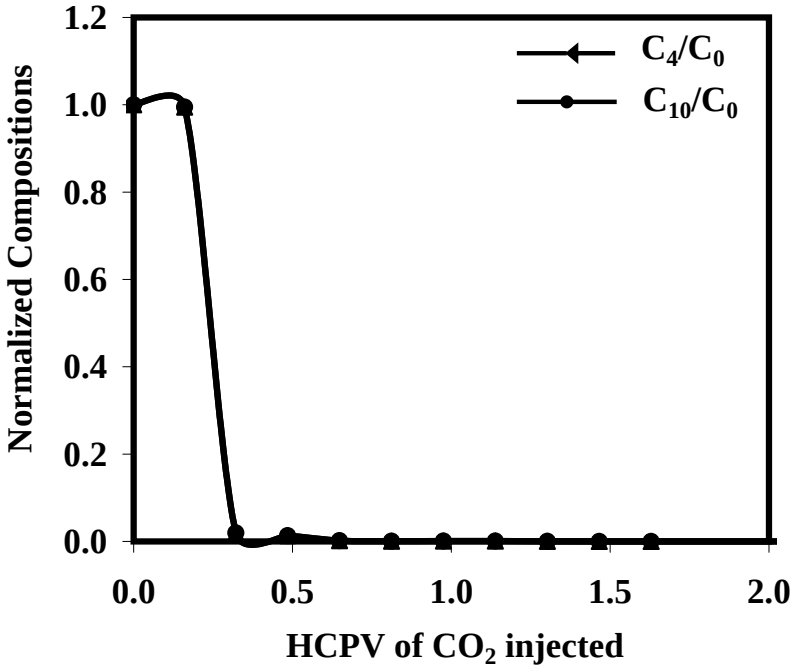

Figure 3.8. Normalized compositions of C_4 and C_{10} in the top layer at 1900 psia in two-dimensional system.

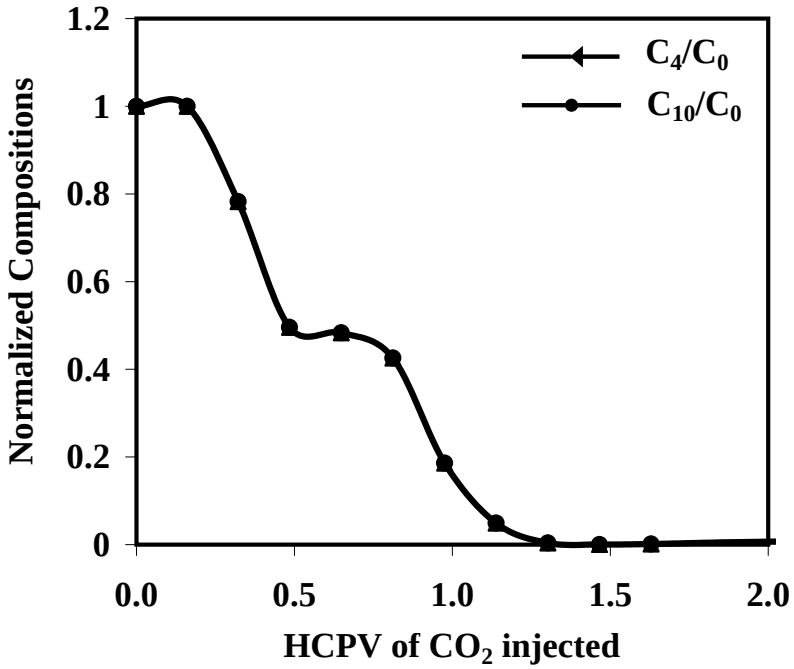

Figure 3.9. Normalized compositions of C_4 and C_{10} in the middle layer at 1900 psia in two-dimensional system.

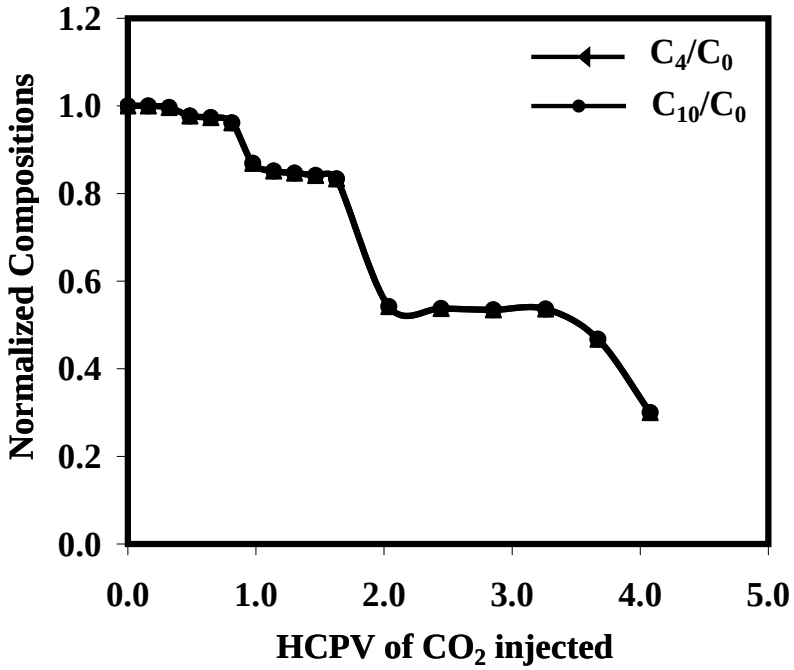

Figure 3.10. Normalized compositions of C_4 and C_{10} in the bottom layer at 1900 psia in two-dimensional system.

middle and bottom layers. So, at any period of time, the amount of oil present in the bottom layer is much higher than the top and middle layers. As it can be seen in the results, the reservoir oil is almost completely recovered in the top and middle layers by 1PV of injected CO_2. But this is not the case in bottom layers. The bottom layer has more oil (current oil in place) than the original oil in place. This is due to gravity segregation and hence leads to a poor performance in the reservoir. These results showed that different portions of the reservoir are being subjected to a different compositional history. As a result, the bottom portions of the reservoir are more susceptible to the formation of solids.

In order to see if these compositions could be evened out, Water Alternating Gas injection studies were performed, where water is injected alternately with CO_2 to stabilize the upward trending CO_2 profile. This is a simple case of three components scenario. More complicated thirteen component simulations were performed in the next section to determine if the same issues prevail.

3.6 Thirteen component one-dimensional simulation results

Figures 3.11, 3.12, and 3.13 show the normalized compositions for all the components at 1500, 2500, and 3500 psia (Run1, Run2, Run3), respectively. Similar observations were made as in the previous section for the three component systems. Miscibility is achieved at a much higher pressure compared to the three component systems. The miscibility pressure was determined using WinProp from CMG for the thirteen components. WinProp is used to analyze the phase behavior of reservoir gas and oil systems, and to generate component properties for CMG's compositional simulator GEM. In Run-1, all the components are not completely recovered. The lighter components (CH_4, NC_2, and NC_3) are recovered completely at 1PV of CO_2 injected. But, not much of the heavier components are recovered even at higher pore volumes as 2PV of CO_2 injected. An indication of a leading C_1 bank can be observed in an immiscible displacement (Run-1). However, the zone does not completely disappear until the displacement is first contact miscible. Also, this displacement has a decreased recovery and an increased transition length, which

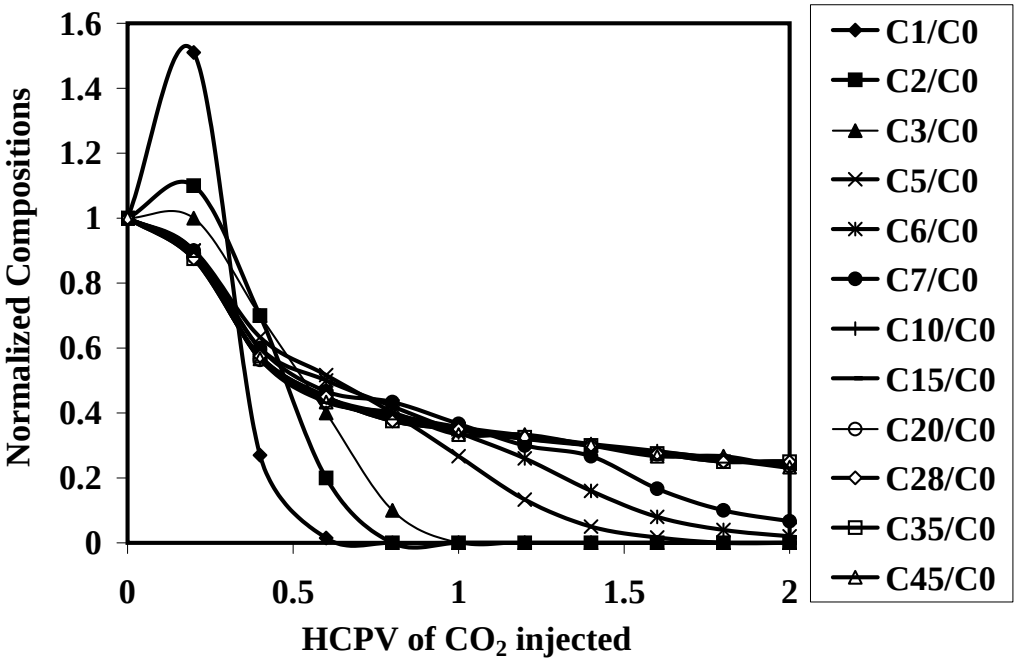

Figure 3.11. Normalized compositions at 1500 psia in one-dimensional system.

are both indicative of an immiscible displacement.

Run 3 (Figure 3.13) shows that all the components are recovered completely at 1.5PV. Run 3 is a clear indication of first contact miscibility scenario in which all the components of oil are recovered in a single contact. It is clear from these figures that as the pressure is increased, there is a transition from immiscible to multiple-contact miscible to first-contact miscible displacements.

Figure 3.14 shows the comparison of percentage recovery in all three cases. This figure clearly illustrates that the FCM system has greater recovery compared to the MCM and the IMM systems, indicating that an IMM displacement mechanism is much less efficient. Also, as the pressure is increased, there is greater recovery, as observed in the three-dimensional system.

3.7 Thirteen component two-dimensional simulation results

Figures 3.15, 3.16, 3.17, 3.18, 3.19, and 3.20 show the normalized compositions of each of the oil components in the top, middle, and bottom layers at 1500psia and

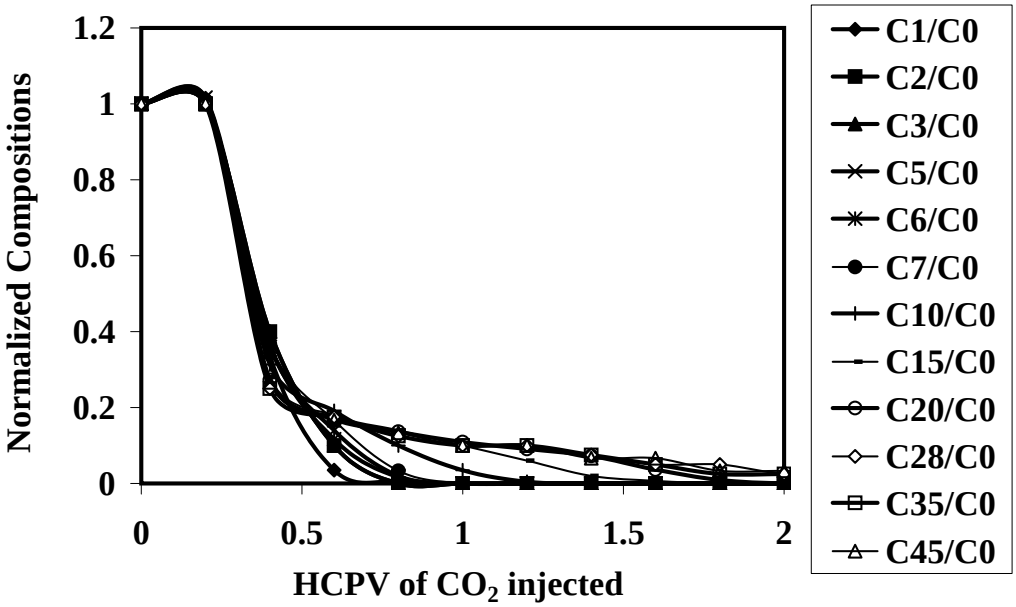

Figure 3.12. Normalized compositions at 2500 psia in one-dimensional system.

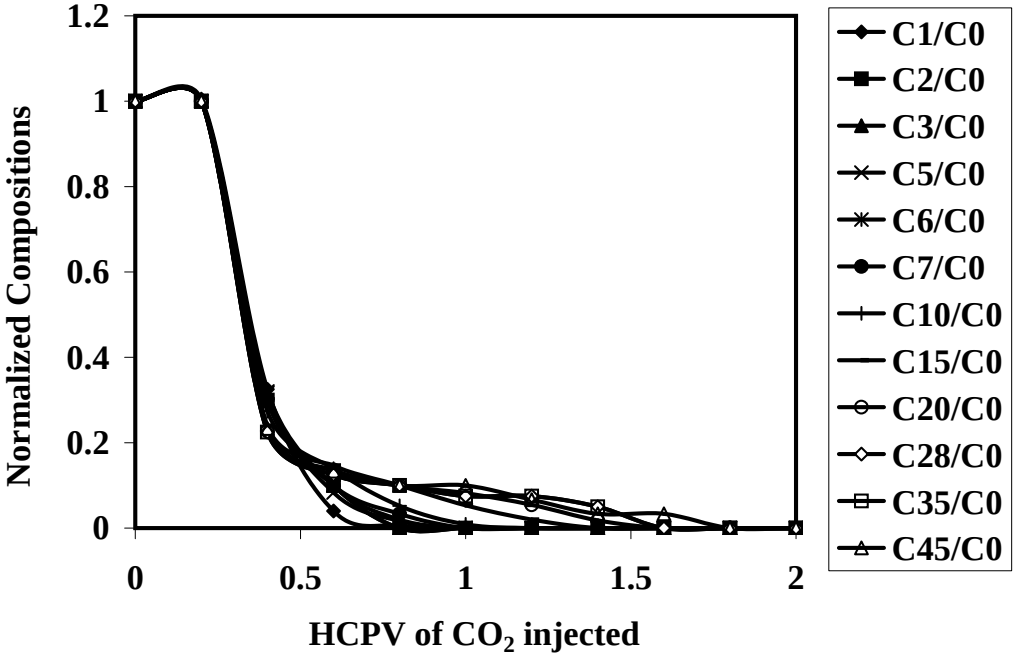

Figure 3.13. Normalized compositions at 3500 psia in one-dimensional system.

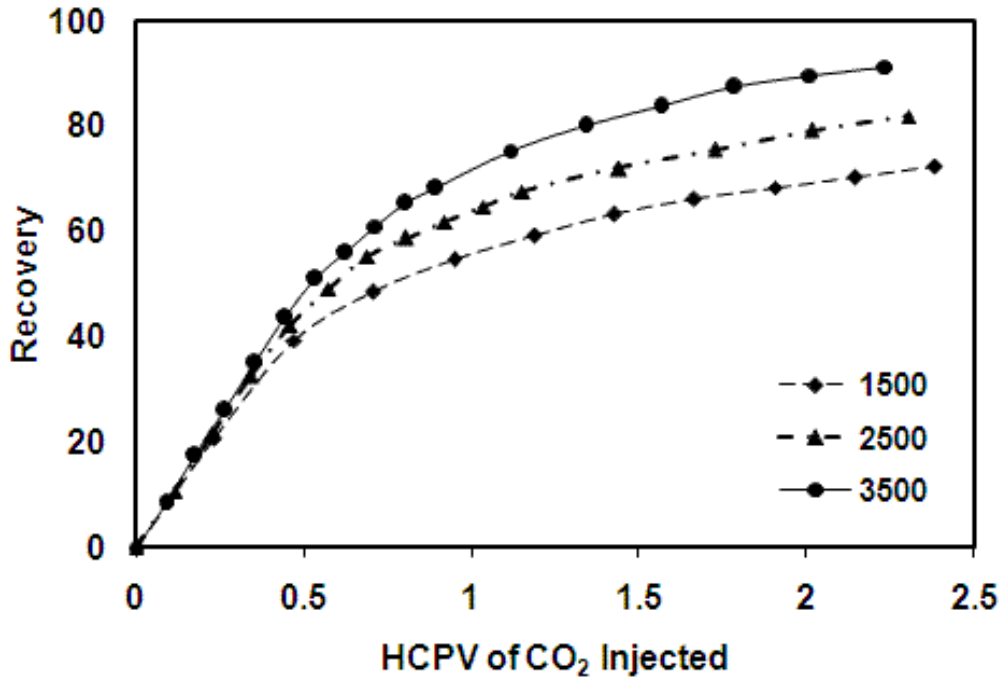

Figure 3.14. Recovery plots at 1500, 2500, 3500 psia for one-dimensional system

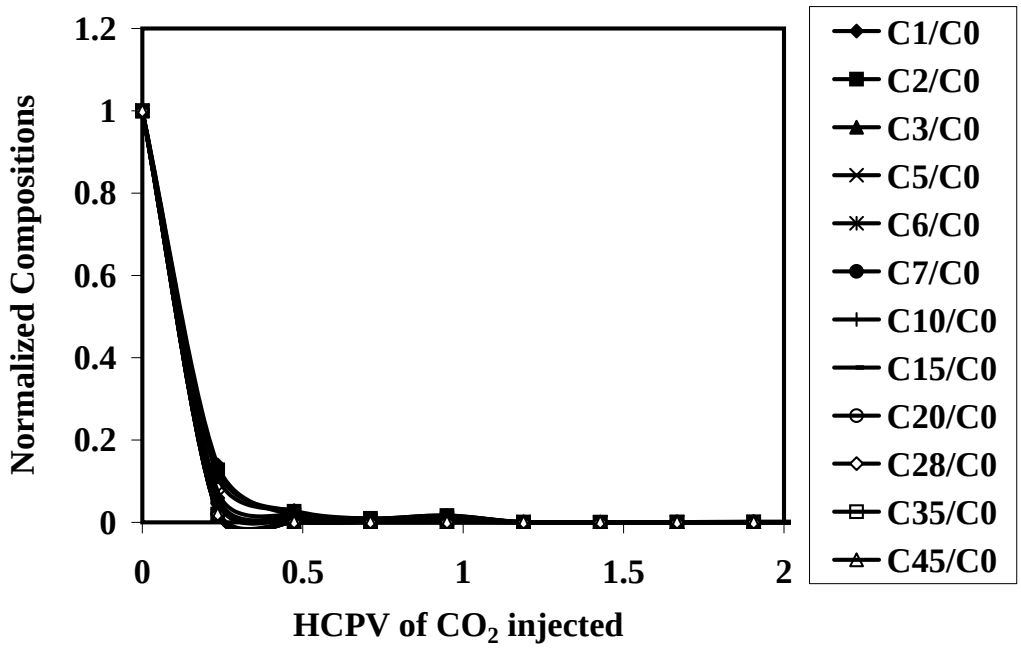

Figure 3.15. Normalized compositions in the top layer at 1500 psia in two-dimensional system.

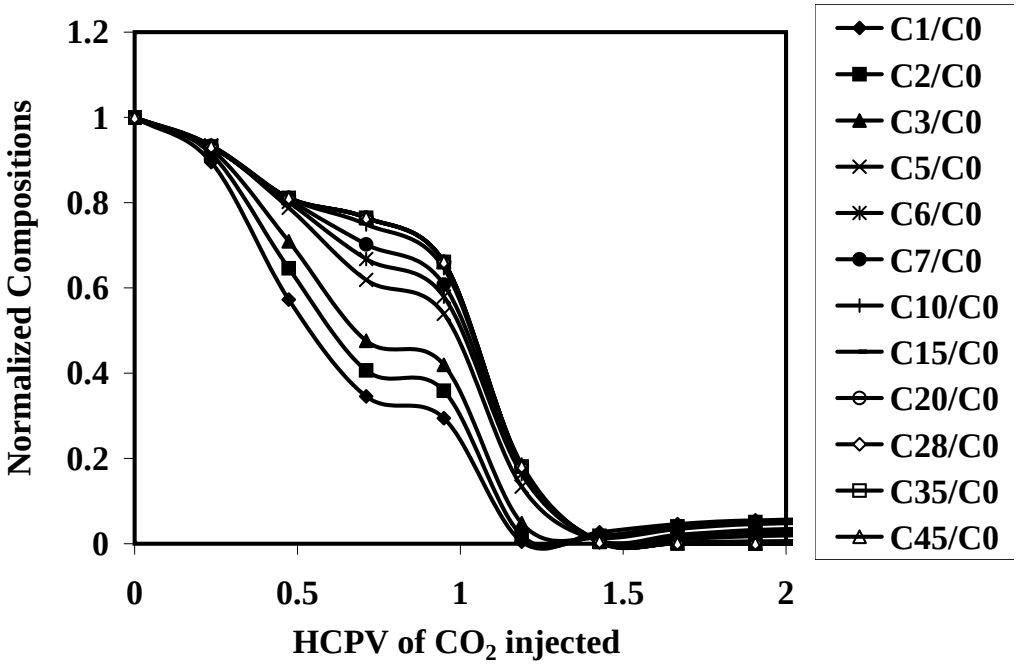

Figure 3.16. Normalized compositions in the middle layer at 1500 psia in two-dimensional system.

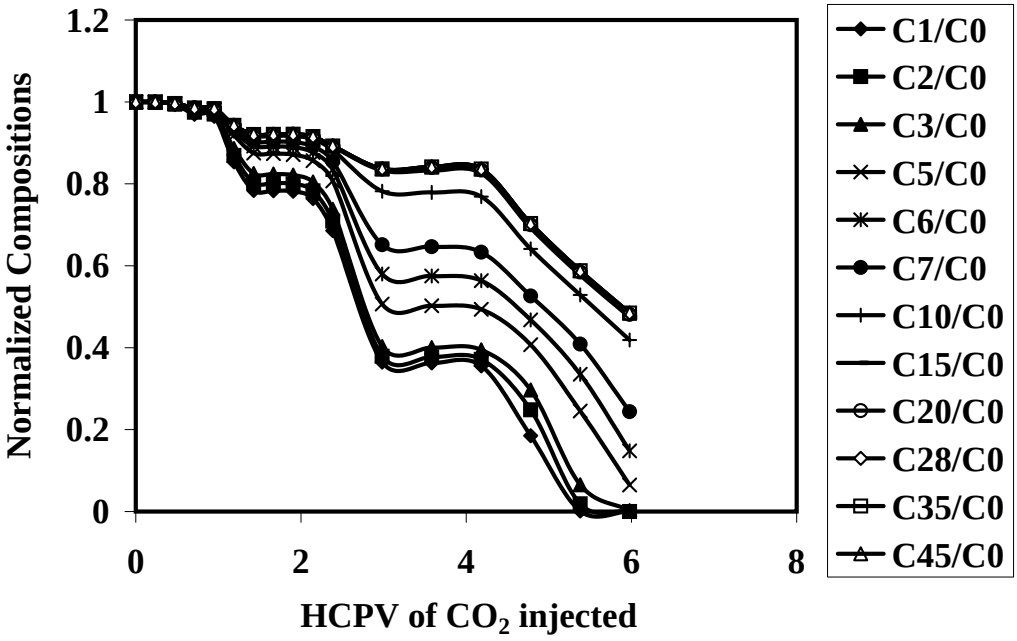

Figure 3.17. Normalized compositions in the bottom layer at 1500 psia in two-dimensional system.

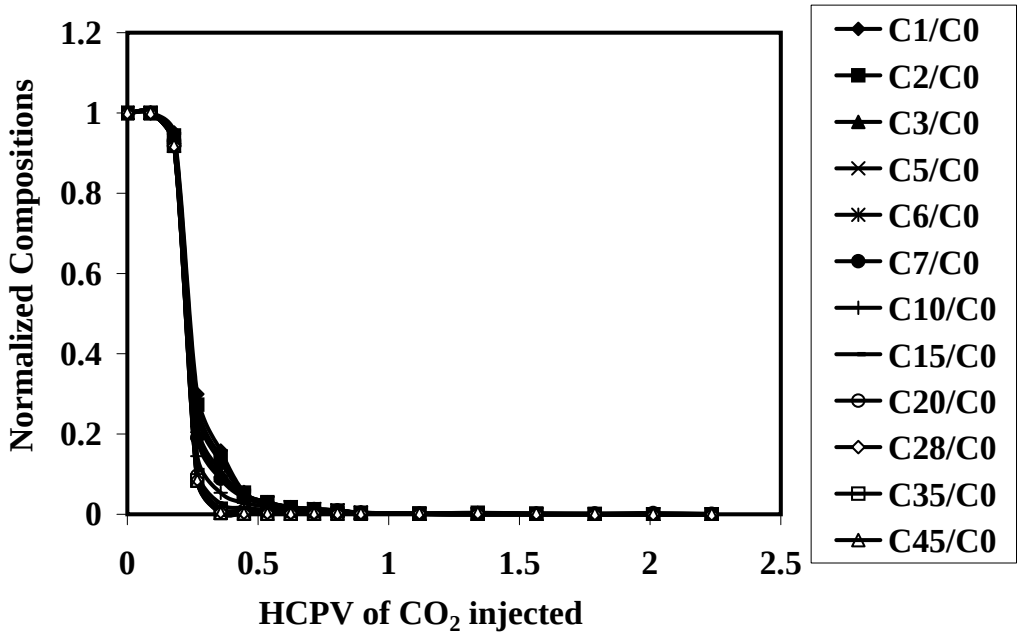

Figure 3.18. Normalized compositions in the top layer at 3500 psia in two-dimensional system.

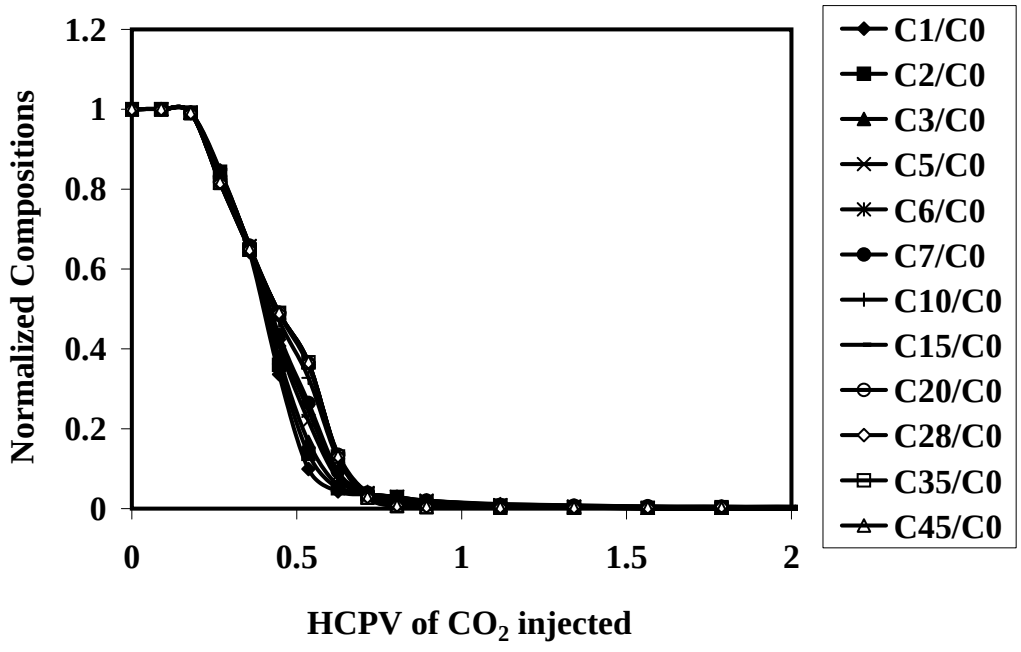

Figure 3.19. Normalized compositions in the middle layer at 3500 psia in two-dimensional system.

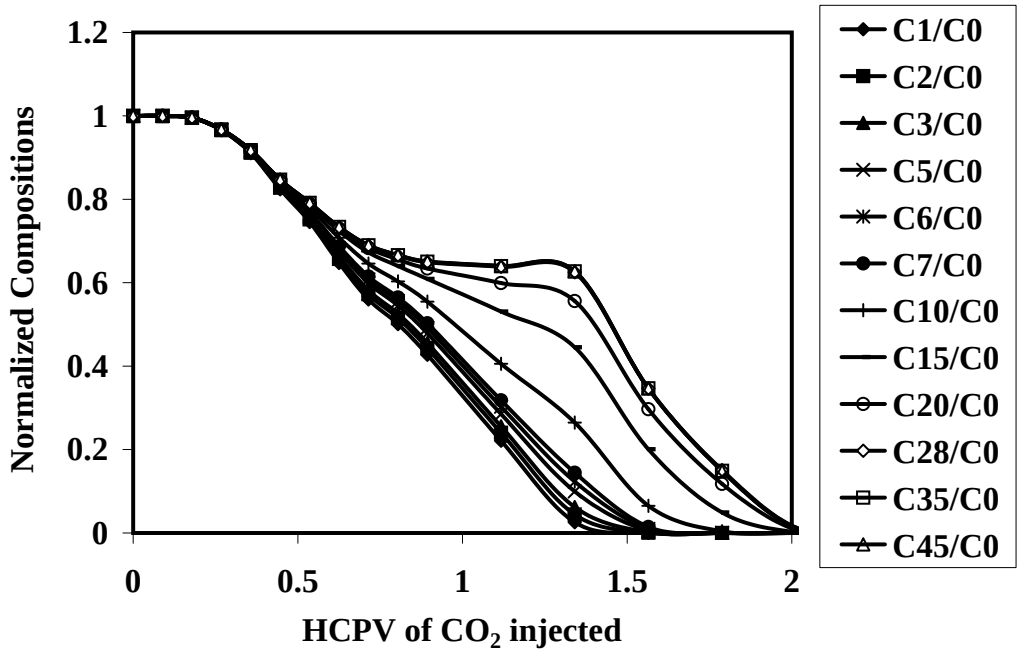

Figure 3.20. Normalized compositions in the bottom layer at 3500 psia in two-dimensional system.

3500 psia. These figures clearly illustrate that the compositional profiles in all three layers are very different. In 2-D simulations, it is observed that the top, middle, and bottom layers have different compositional profiles. Figure 3.21 shows the recovery at 1500 and 3500 psia. Similar observations were made as the one-dimensional studies; as pressure is increased, there is greater recovery.

3.8 Composition path along the length of the reservoir

The compositional path of C_4 and C_{10} is shown in Figure 3.22. This figure shows the front view of the reservoir at 0.48PV and 0.71PV of CO_2 injected.

Figure 3.22 shows that at 0.23PV of CO_2 injected C_4 is recovered completely from the top portion of the reservoir and not much of it is recovered from the bottom layers. The fluid flow in each part of the reservoir is very different. CO_2 is injected constantly into all the layers of the reservoir simultaneously. As CO_2 is injected into the reservoir, most of the oil flows from the top layers to the middle and bottom layers. So, at any period of time, the amount of oil present in the bottom layer is much higher than the top and middle layers. As it can be seen in

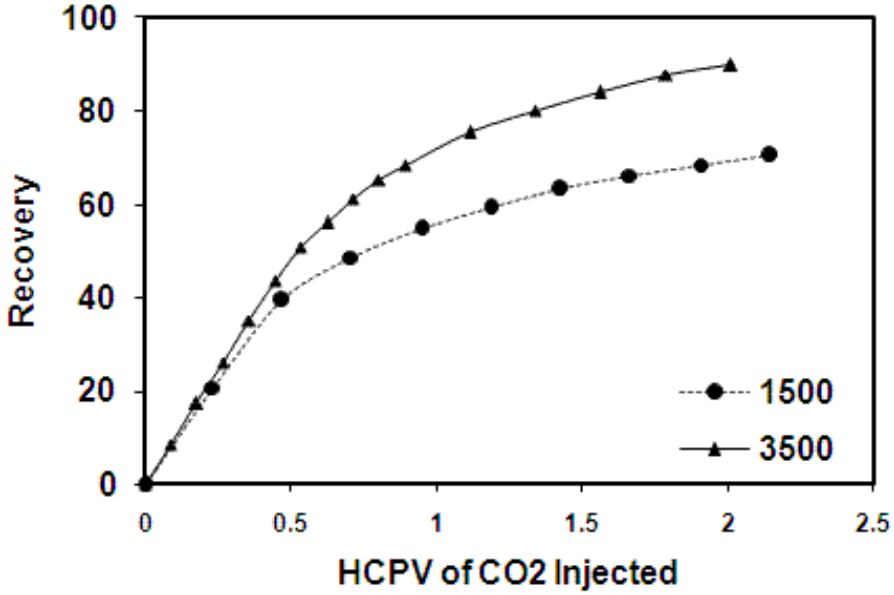

Figure 3.21. Recovery plots at 1500 and 3500 psia for two-dimensional system

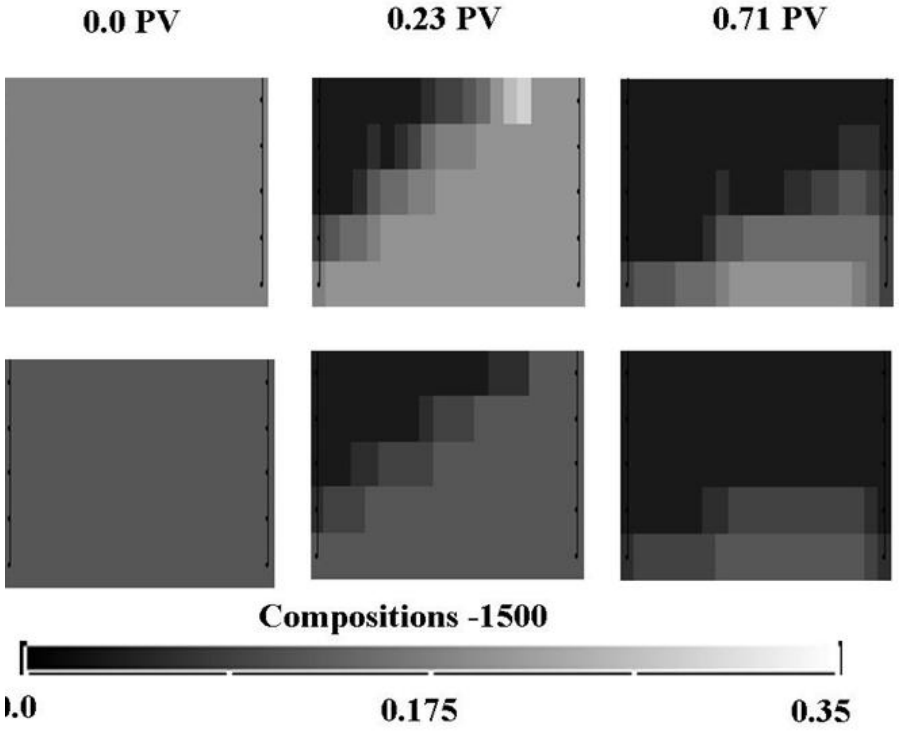

Figure 3.22. Composition trajectory at 1900 psia in the bottom layer.

the results, the reservoir oil is almost completely recovered in the top and middle layers by 1PV of injected CO_2. But this is not the case in bottom layers. The bottom layer has more oil (current oil in place) than the original oil in place. This is due to gravity segregation and hence leads to a poor performance in the reservoir. These results showed that different portions of the reservoir are being subjected to a different compositional history. As a result, the bottom portions of the reservoir are more susceptible to the formation of solids.

In order to see if these compositions could be evened out, Water Alternating Gas injection studies were performed, where water is injected alternately with CO_2 to stabilize the upward trending CO_2 profile.

3.9 Water Alternating Gas injection studies - Introduction

In most practical enhanced oil recovery operations, water is injected alternately with CO_2 to stabilize the upward trending CO_2 profile. This process is called Water Alternating Gas injection. The injection of water followed by gas and again by water causes significant redistribution of the fluids in the reservoir. Hence, the oil which otherwise would not be mobile under either gas injection or water injection alone is mobilized and produced [13] [14] [12].

The objective is to conduct a study which will investigate the WAG process in enhanced oil recovery (EOR) process. The hypothesis is to determine if the displacement in the bottom layer is improved with WAG injection, compared to only gas injection in 2-D displacement studies.

3.10 Thirteen component two-dimensional WAG simulations

The components in the model were chosen to be similar to the thirteen components (CO_2, CH_4, NC_2, NC_3, NC_5, NC_6, NC_7, FC_{10}, FC_{15}, FC_{20}, FC_{28}, FC_{35}, and FC_{45}) used in the previous 2-D simulation studies. Similar reservoir properties and initial conditions were used as the two-dimensional studies. The reservoir is a 20 X 1 X 5 Cartesian grid.

3.11 Simulation analysis

Similar comparisons were performed as the previous studies. Normalized compositions were plotted as a function of hydrocarbon pore volume of CO_2 injected in each of the three layers (upper, middle, and bottom layers). The compositions for the middle block (the 10th block) are considered for analysis. Water is injected into the reservoir followed by gas and again by water. Simulation results were analyzed for the phase behavior and different miscibility displacements.

Figures 3.23, 3.24, and 3.25 show the normalized compositions of each of the oil components in the top, middle, and bottom layers at 1500psia. These figures clearly illustrate, all of the components are recovered completely in less than 1PV of CO_2 injected. The recovery of the components is also much higher in WAG compared to gas injection. Also, the sweep efficiency is improved by WAG injection. Components in the bottom layers are recovered at as early as 0.2 PV.

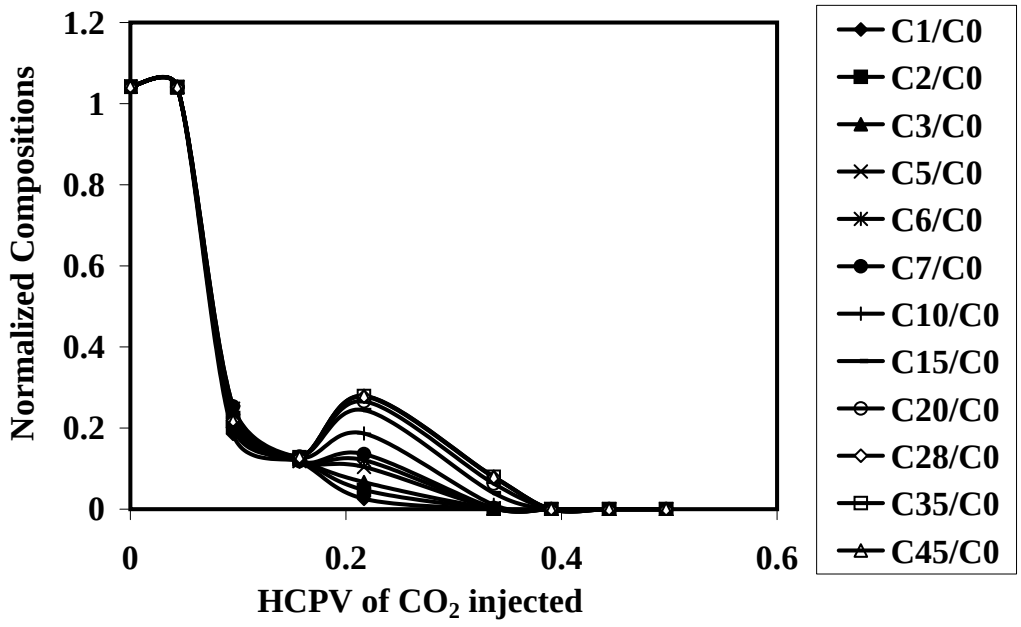

Figure 3.23. Normalized compositions of the top layer at 3500 psia.

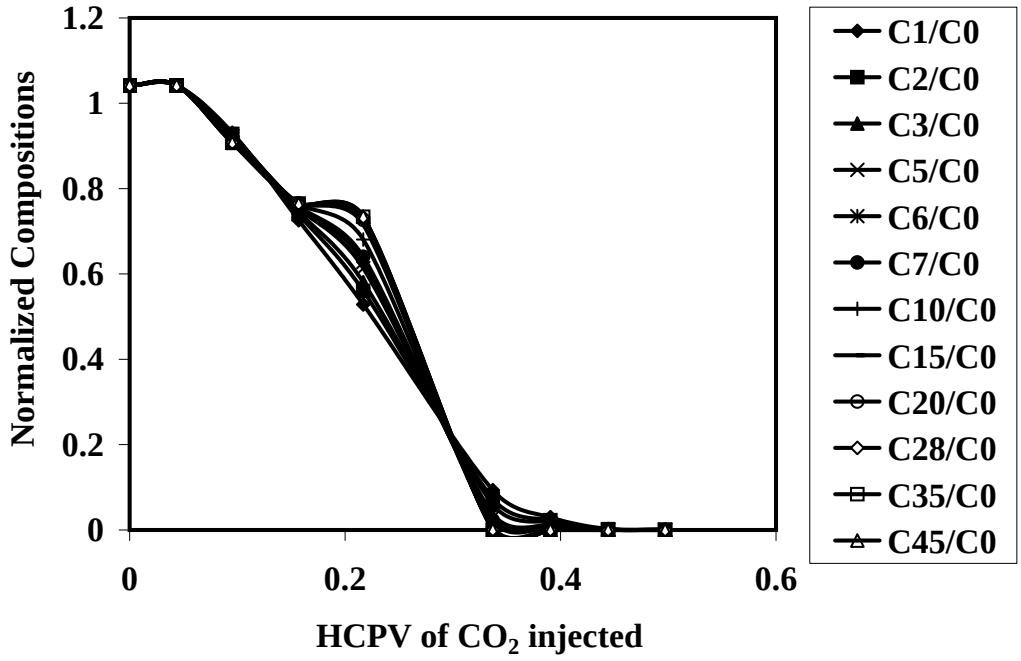

Figure 3.24. Normalized compositions of the middle layer at 3500 psia.

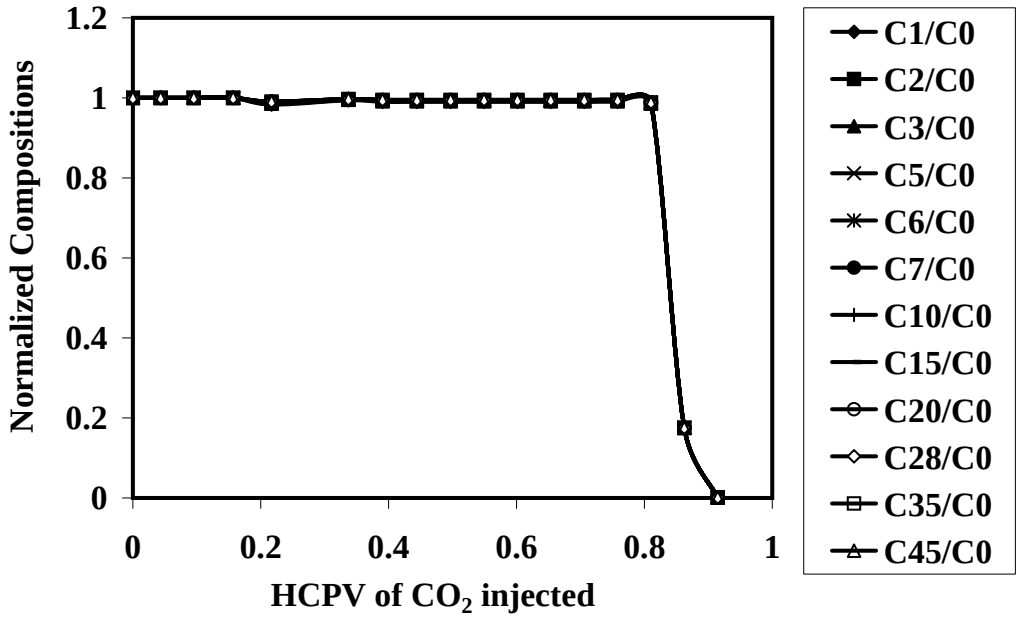

Figure 3.25. Normalized compositions of the bottom layer at 3500 psia.

3.12 Composition path along the length of the reservoir for WAG simulations

The compositional path of C_4 and C_{10} is shown in Figure 3.26. This figure shows the front view of the reservoir at 0.23PV and 0.71PV of CO_2 injected.

Figure 3.26 shows that, all of the components are recovered completely in less than 1PV of CO_2 injected. The recovery of the components is also much higher in WAG compared to gas injection.

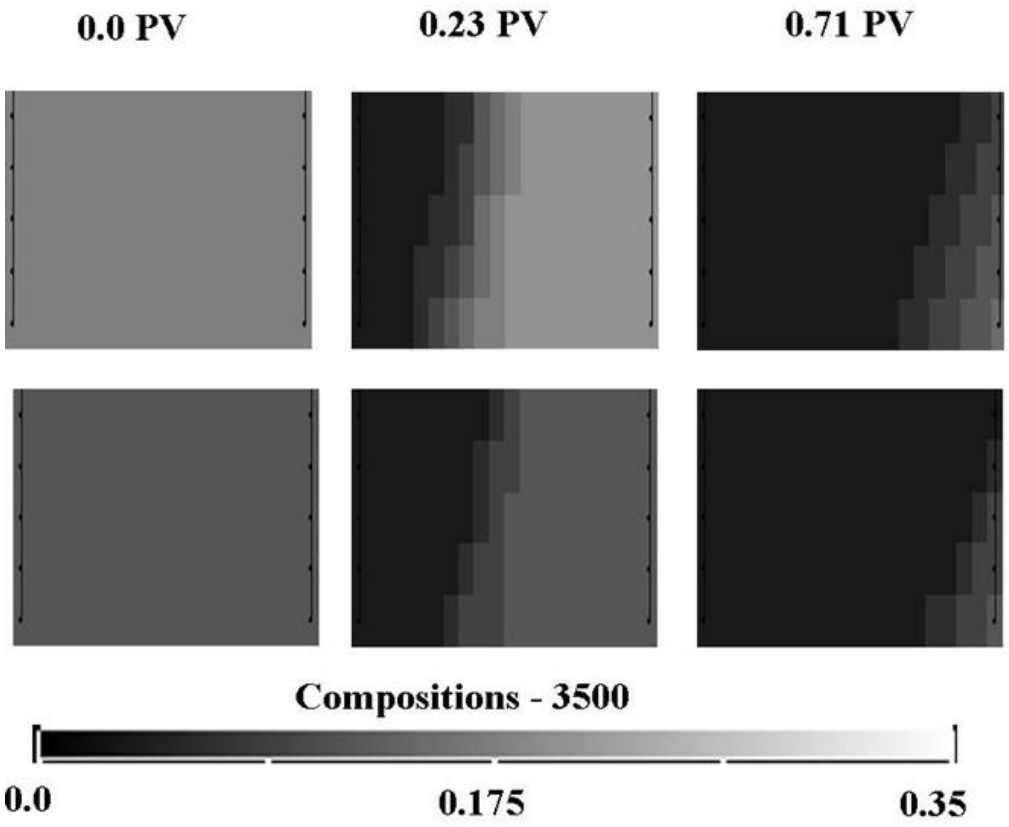

Figure 3.26. Composition trajectory at 1900 psia in the bottom layer.

CHAPTER 4

CO_2 INJECTION FOR CARBON SEQUESTRATION

4.1 Previous efforts to simulate subsurface CO_2 injection for CO_2 sequestration

[17] presented a numerical modeling study of CO_2 injection and sequestration using the reservoir simulator TOUGH2, without considering the dissolution of CO_2 and its escape through leaks. [18] used the Eclipse® reservoir simulator to model the escape of CO_2 from aquifers. [3] used a two-dimensional numerical model to assess the hydrodynamic trapping capacity of two aquifers in Canada. [19] also used TOUGH2® reservoir simulator to model the sequestration of CO_2 in the Powder River Basin, Wyoming. These studies show that regional-scale sedimentary aquifers in subsurface geological structures offer a large storage capacity for CO_2.

Detailed simulation studies may provide useful information regarding the potential sites for CO_2 sequestration and sites where leakage might occur. A very detailed study of various aspects of faults in sandstone reservoirs and the numerical results for these studies is presented in the next sections.

The fraction of pore space that can be filled with injected gas is controlled largely by reservoir heterogeneity, gravity segregation, and the efficiency that the injected gas displaces whatever pore fluids are present. Knowledge of the pressure distribution in the CO_2 phase around the injection well is essential for modeling of critical injection-related phenomena such as well stimulation [20] and fracturing [21] [4].

Methods outlined by [22] and [23] are used to estimate the permeability tensors for deformation bands and joint zones. Weighted harmonic averaging is used to estimate the effective permeability of the faults. The impact of fault zones on fluid

flow has been addressed in numerous modeling studies [24] , [25], [26], [27], [28], [29].

[30] have extensively studied and developed a general modeling capability for analyzing CO_2 sequestration in geologic formations. They developed an internationally recognized suite of reactive transport simulators (GIMRT, NUFT), supporting geochemical software (SUPCRT92), and thermodynamic-kinetic databases (GEMBOCHS). Using this integrated toolbox, they identified the geochemical hydrologic and structural constraints on successful CO_2 sequestration. The CO_2 migrates by displacing ambient water, with which it is largely immiscible, and by rising relative to this water, owing to its lower density. It also moves faster than the ambient fluid because of its lower viscosity. Understanding the relative effectiveness of these competing migration and sequestration processes is the key to identifying sites that will provide optimal sequestration performance. Preliminary, two-dimensional NUFT and GIMRT simulations of CO_2 injection were performed by Johnson and colleagues to illustrate the relative effectiveness of various sequestration processes after one year of injection.

Faults and fractures provide one of the primary risk factors for leakage in an engineered system. In this research, faults in various settings are examined to determine their influence on CO_2 flow with reservoir rock and fault-affected rock. Fluid flow simulation results in this study help to constrain how engineered sites might best be designed to reduce the risk of leakage, and to examine the possible consequences of a leaking system.

4.2 Approach

In this study, a series of reservoir simulations were performed to determine the feasibility of sequestering CO_2 in faulted sandstone with a range of high to low matrix permeability values that represent different depositional environments. (e.g., windborne aeolian sand, waterborne fluvial sand, or delta sands). Numerical simulations of CO_2 injection and migration in a faulted sandstone reservoir/aquifer were performed to assess how unseen, or poorly characterized, faults might com-

promise CO_2 sequestration operations.

Values of a number of poorly known reservoir rock and fluid properties were determined by literature review, due to lack of appropriate data. A set of simple calculations were performed to calculate the equivalent permeabilities and porosities. Simple averaging methods were used to compute the equivalent porosities and permeabilities. These are discussed in detail in the next section.

Various reservoir scenarios were investigated incorporating these fault-related fluid flow properties. Unfaulted sandstone reservoirs with low and high permeability scenarios were considered. Two end member fault types were considered: low-permeability faults dominated by deformation-band networks and high-permeability faults dominated by fracture networks. CO_2 is injected into the reservoir using vertical wells. Certain problems such as reservoir pressure build-up arise when low-permeability faults are encountered. These issues are solved to some extent when vertical wells are replaced by horizontal wells. Comparisons of the various injection strategies were performed and analyzed. This study is then extended to a case where faults cut the reservoir and allow CO_2 gas to escape by flow along the faults, thereby breaking the seal. A sealed case with a high permeability fault and its impact on the CO_2 leakage is investigated. Relative permeability and capillary pressure issues for the different types of faults were analyzed. Fault permeability anisotropy is then analyzed and compared for the different types of faults.

This study is then extended to a larger reservoir volume for longer periods of time. Different fault scenarios were then investigated with the larger volume for as long as 10 years of injection. The simulation was run until 30 years after the CO_2 injection was stopped, to illustrate the CO_2 migration in the reservoir.

CHAPTER 5

PROPERTIES OF RESERVOIR ROCK

The reservoir in this study is comprised of both unfaulted and fault-affected sandstone. The reservoir used in the simulation study is not a real reservoir; however, the rock properties are based on that of the Navajo sandstone encountered both in the subsurface and outcrop. In situ and laboratory tests conducted [22], [25], [26] provide a context for assigning rock properties in the reservoir simulator.

5.1 Aeolian Navajo sandstone properties

The Navajo sandstone is a good analog for reservoir simulation and study. Porosity values of the Navajo sandstone can be as large as 20 to 30% [31]. Permeability values measured in the Navajo sandstone typically range from 100 to 1000 millidarcies (md), with values as large as 8000md [32]. [33] and [34] report average permeability values for Navajo sandstone of 450 to 860 md, respectively.

1. Enhance permeability with open joints or
2. Reduce permeability with deformation bands

Joints are extension-induced mode I fractures that exhibit only opening displacement (white features in Figure 5.1). Deformation bands are planar, light-colored, vein-like features formed of ground and crushed sandstone grains and fine powder (dark features in 5.1). Both joints and deformation bands are found as single features, or in networks, aligned subparallel to fault zones (Figure 5.1). Joints or deformation bands may be found alone, or together, leading to the possibility of a wide range of deformation-induced permeability variation within and near faults [22], [35].

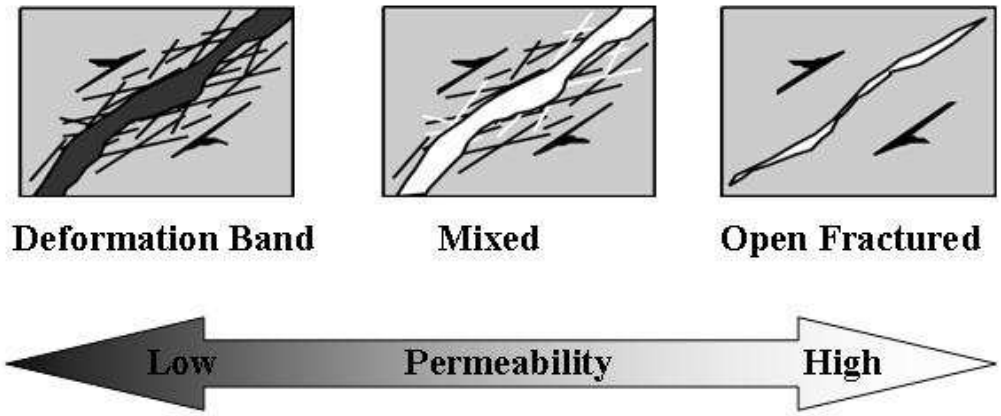

Figure 5.1. Typical arrangements of deformation-induced features in faulted sandstone. Arrows show direction of fault slip. Black features are individual/amalgamated deformation bands. White features are open fractures.

The relative permeability and capillary pressures of the sandstone rock are unknown. But, here the generic nature of the curves is employed considering the permeability and porosity of the Navajo sandstone. These curves are discussed in Section 8.2.

5.2 Properties of fault affected rocks

Fault zone permeability is a function of fault zone architecture and the intrinsic properties of the fault-related rocks. Fault zones can be barriers to fluid flow, conduits, or a mixture of barriers and conduits. The properties of architectural elements reflect the nature and distribution of damage elements [22]. The fault characteristics considered are derived from outcrop studies and shallow drilling of the Jurassic Navajo sandstone of the Colorado Plateau [32], [36]. The major components of the fault zone are:

1. Host rock
2. Deformation band networks
3. Fracture networks

This section discusses permeability and porosity elements. The main questions addressed here are:

1. What are the properties of fault affected rocks?
2. How do porosity and permeability vary with increasing number of deformation bands or fractures?

[22] suggests that faults formed in brittle host rock (e.g., sandstone) comprise two distinct components: fault core and damage zone. The fault core, where most fault displacement is accommodated, contains fault rocks that have undergone the greatest degree of deformation. The core may include high-permeability slip-surface fractures or low-permeability crushed rock gouge zones. The fault damage zone is a network of high- and low-permeability subsidiary structures (fractures, veins, and folds) that is interfingered with the fault core. The fault core and damage zones are surrounded by relatively undeformed host rock.

The permeability within a deformation band filled faults can be reduced by at least 3 orders of magnitude with respect to the host rock[31]. Computed k across the fault zone is typically about 60 mD, or 0.1 to 0.01 times the permeability of the host sandstone. These structures represent an important impediment to fluid flow. Fracture networks are usually observed within and along the edges of clusters of deformation bands. Primary porosity of the Navajo Sandstone ranges from 13-25%; deformation bands have porosities of 3-13% and host rock between deformation bands exhibits porosities of 4-18% [32]. Individual deformation bands are typically 1 mm thick but may amalgamate in zones greater than 1 m wide. The aperture of open fractures is difficult to assess, but is likely less than 1 mm.

In situ cross-well injection tests show how sparse fractures provide enhanced, localized connectivity within the low-k fault [32]. The presence of fractures in an intact rock mass may enhance rock permeability. It depends on the aperture and infilling of these joints, as well as their interconnectivity. However, the presence of such fractures does not always imply that the flow will be enhanced. Apparently, other parameters may play a role, such as porosity, water content, and mineralogical composition. Deformation bands can reduce the effective permeability of faulted sandstone by one or more orders of magnitude while fractures can locally enhance the effective permeability of the host sandstone by similar magnitudes. These two-end member cases were studied in detail.

CHAPTER 6

ESTIMATING PETROPHYSICAL PROPERTIES FOR RESERVOIR GRID BLOCKS

From an idealized point of view, the two end member types of fault-affected sandstone outlined above are dominated by either fractures or deformation bands.

6.1 Permeability and porosity

The calculation of bulk permeability and porosity of the fault zone grid blocks is discussed in this section. Such calculations are required to incorporate fault zones into reservoir models [37]. A simple averaging approach is used to compute equivalent permeability values for 1-m blocks containing either joints or deformation bands (Figure 6.1). If the host rock is homogeneous and isotropic, adding a different number of features (deformation bands or fractures) in each orientation (Figure 6.1) will lead to permeability anisotropy. Starting with a homogeneous, host rock sandstone with permeability of 500 md and porosity of 20%, fractures (0.1 mm aperture) or deformation bands (1mm thick with permeability = 0.1 md and porosity = 7%) are progressively added (in orthogonal networks) to the 1-m block. Assumptions made in the calculation include the following:

1. Enhance permeability with open joints or
2. Reduce permeability with deformation bands
3. Host rock between the fractures or deformation bands is undamaged
4. A weighted harmonic mean produces a reasonable effective permeability while a weighted arithmetic mean produces a reasonable effective porosity

The weighed arithmetic mean represents the permeability of the fault, when flow parallels the fault [38], [39], [40]. In this case:

$$k_{am} = \sum_{n}^{1} \frac{k_i h_i}{\sum h_i} \tag{6.1}$$

For flow normal to the fault, the weighed harmonic mean estimates the bulk permeability as:

$$k_{hm} = \frac{\sum_{n}^{1} h_i}{\sum_{n}^{1} \frac{h_i}{k_i}} \tag{6.2}$$

where k_{am} is the arithmetic mean permeability, k_{hm} is the harmonic mean permeability k_i is the permeability of the i-th fault component, and h_i is the thickness of the i-th component.

The isotropic permeability in a system with three orthogonal fractures set where each set has the same number of fractures is computed. This is done by first computing arithmetic mean along the direction of flow and then by computing the harmonic mean in the orthogonal directions.

The permeability of the host rock is assumed to be 500md with porosity of 20%; 0.1md and 7% are assumed for the deformation bands. The thickness of the deformation band is 1mm. The bulk permeabilities of the fault block were calculated by increasing the number of features (deformation bands) in Table 6.1. Intersections were also accounted for when computing the volumes of the cube. Similar computations were performed for fractures and the results are summarized in Table 6.2. The fracture aperture is assumed to be $100\mu m$ with a porosity of 100%. The permeability of the fractures in units of md is calculated by:

$$k = \frac{b^2}{12}\ 10^{15} \tag{6.3}$$

where b is the fracture aperture in meters.

Porosity averages are computed by a simple volume-weighed arithmetic average of the porosities of all block components.

Figure 6.1 shows the progressive change in sandstone permeability and porosity as the number of deformation bands or fractures are increased. The heterogeneous

Table 6.1. Isotropic grid block permeability and porosity of a 1m cube with increasing deformation band where, V = Volume, Ints = intersections, n = porosity, am = arithmetic mean, and hm = harmonic mean.

Number of DB's	Number of Ints	V_{host} (m^3)	$V_{DB's}$ (m^3)	n_{am}	k_{hm} (md)	k_{am} (md)
0	0	1	0	0.2	500	500
120	4800	0.88	0.12	0.18	23.9	22.9
900	270000	0.24	0.77	0.1	3.32	2.62

Table 6.2. Isotropic grid block permeability and porosity of a 1m cube with increasing fractures where, V = Volume, Ints = intersections, n = porosity, am = arithmetic mean, and hm = harmonic mean.

Number of fr's	Number of Ints	V_{host} (m^3)	$V_{fr's}$ (m^3)	n_{am}	k_{hm} (md)	k_{am} (md)
0	0	1	0	0.2	500	500
120	4800	0.99	0.01	0.21	502	7167
900	270000	0.91	0.09	0.27	515	50500

permeability and porosity structures of faults can be constructed by assembling groups of blocks with different, fault-related effective properties assigned to each block.

Increasing the number of structural features in each of the orthogonal sets leads to decreasing porosity and permeability, adding deformation bands (DBs), or increasing porosity and permeability, adding fractures (Figure 6.1). The number of features and the characteristics of each feature are the same for each set; hence, the computed equivalent permeability values for the $1m^3$ block are isotropic. The

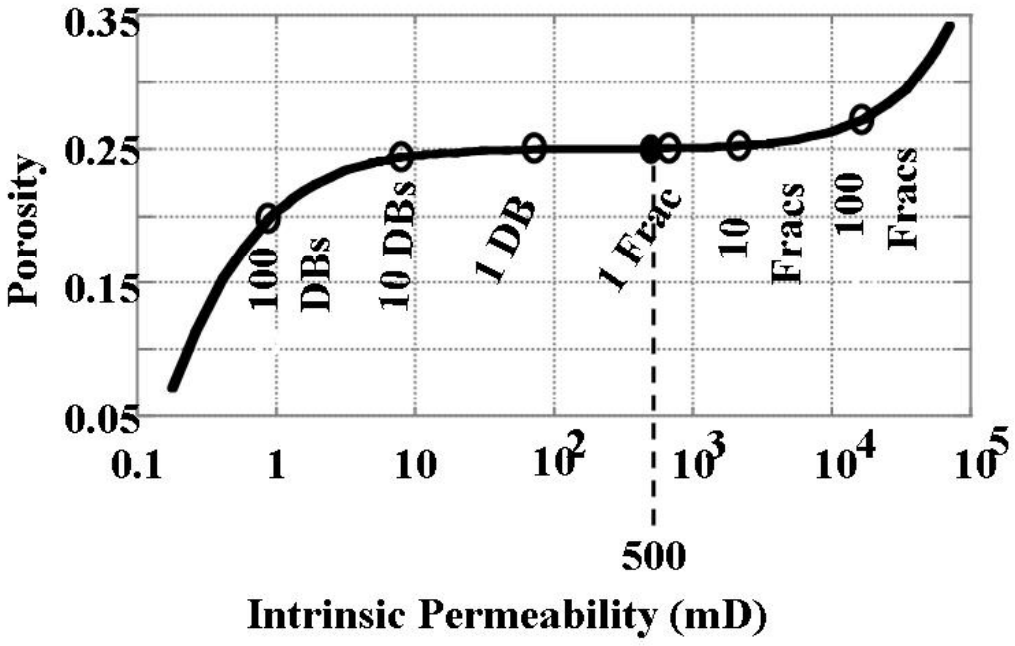

Figure 6.1. Variation in equivalent porosity and permeability of a $1m^3$ rock block for two different host rocks as low-k deformation bands (DBs: $\phi = 0.07$, k = 500 mD, 1 mm thick) and high-k fractures (Fracs: aperture = 0.1 mm) are added. The upper line is for host k of 500mD and porosity of 25%. The lower line is for host k of 50 mD and $\phi = 0.15$. 'DB' identifies deformation bands and ' Frac' identifies fractures.

upper line plotted in Figure 6.1 shows that the equivalent porosity of 25% porous host rock changes little as 10 fractures or 10 DBs are added for each orthogonal set of structural features. Adding 100 structural features to each set yields a significant change in the porosity: increase of 0.02 with fractures and decrease of 0.05 with deformation bands. In contrast to the relatively small changes in the porosity caused by adding a small number of structural features, the equivalent permeability of the sandstone block is strongly affected by adding a few deformation bands or fractures. For example, adding 10 DBs to the block yields about 2 orders of magnitude reduction in equivalent permeability. Adding the same number of

fractures yields a smaller (less than one order magnitude), but still significant, increase in equivalent permeability (Figure 6.1).

Adding structural features to a 1-m sandstone cube with lower porosity yields similar changes in porosity (lower line plotted in Figure 6.1) as obtained for a higher porosity sandstone (upper line plotted in Figure 6.1). The corresponding lower permeability of the lower porosity host rock, however, causes the addition of deformation bands to have a lesser impact (factor of 10 reduction with 10 DBs) while adding fractures has a greater impact (factor of 100 increase with 10 fractures) (Figure 6.1).

6.2 Relative permeability and capillary pressures relationships

The relative permeability curves for the CO_2-water in sandstone system were poorly known. Several researchers have used the Van Genuchten [41] relationship for the water relative permeability and Corey's form for the gas relative permeability [42]. Two-phase flow functions, capillary pressure and relative permeabilities, are typically determined through analyses of data acquired from measurements on some flooding process in the laboratory. It is well known that capillary pressure relationships may vary with both porosity and permeability, even when cores from the same lithology are considered [17]. The capillary pressure functions will then be different in grid blocks with different permeability and/or porosity.

This modeling study uses two different relative permeability curves for the host rock and the faulted zone. The relative permeability curves were developed using data from the literature for rocks that have similar properties to the Navajo sandstone for the CO_2-water system. Figure 6.2 shows the permeability-porosity relationship developed for a 500md host rock case after adding fractures or deformation bands.

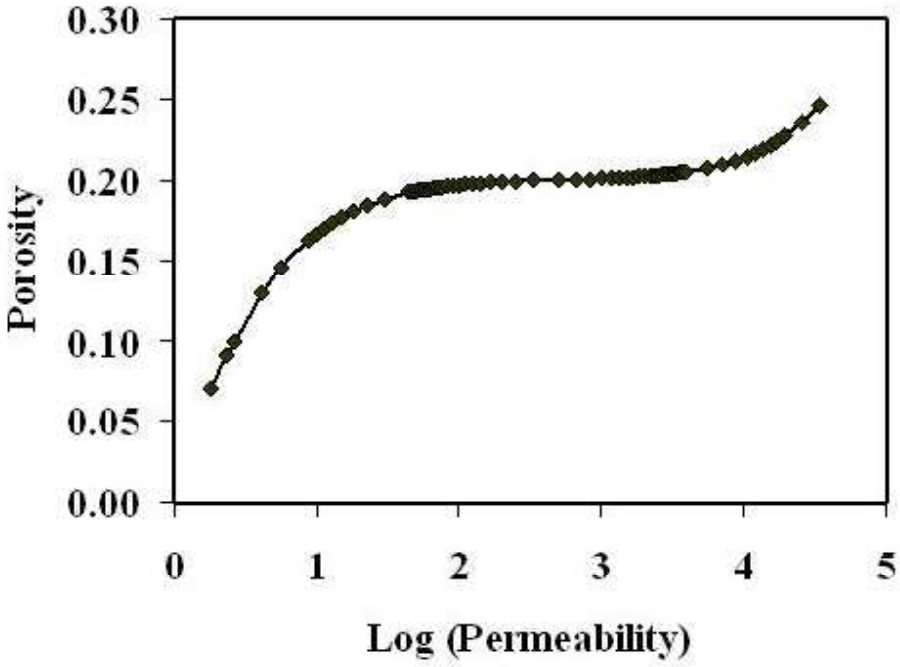

Figure 6.2. Porosity-Permeability relationship for the 500md host rock

When considering CO_2 injection into a sandstone reservoir, relative permeability relationships for the sandstone with respect to water and CO_2 must be identified because the relative proportion of water and liquid CO_2 in the pore space will vary as a function of time and space in the reservoir. Unfortunately, few data are available for estimating these relationships for CO_2-water systems. As a consequence, curves that represent similar rock type and properties of the Navajo sandstone for CO_2-water systems from literature were used for the relative permeability curves. Figures 6.3, 6.4 and 6.5 present the relative permeability curves used for the host rock, deformation band faults, and fractured faults, respectively.

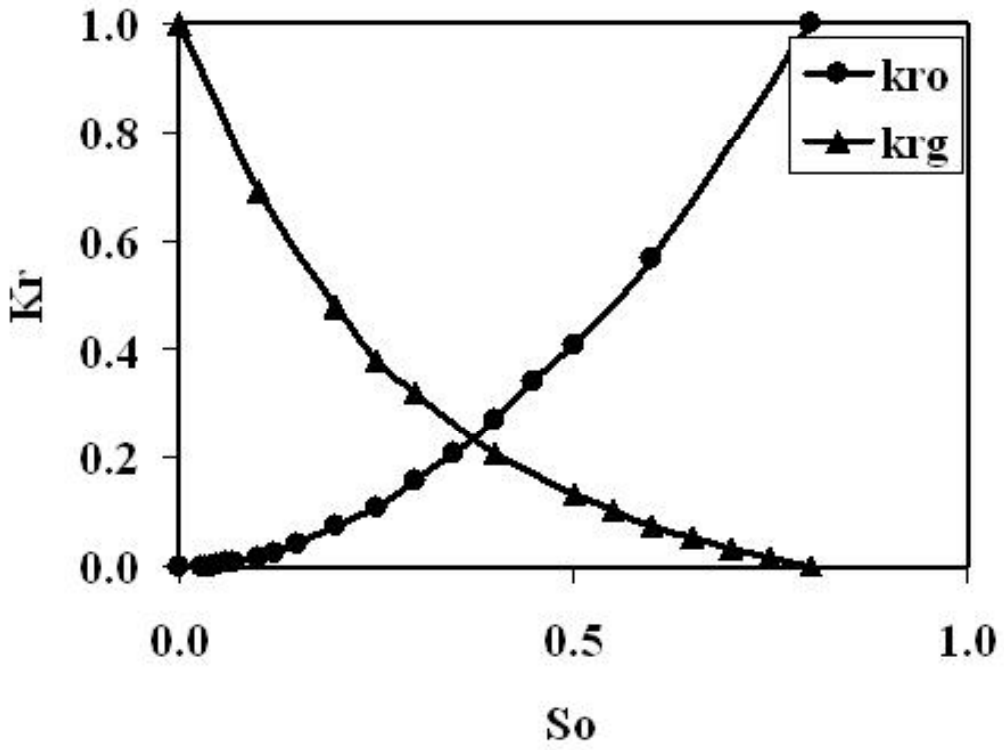

Figure 6.3. Relative permeability curve for the host rock

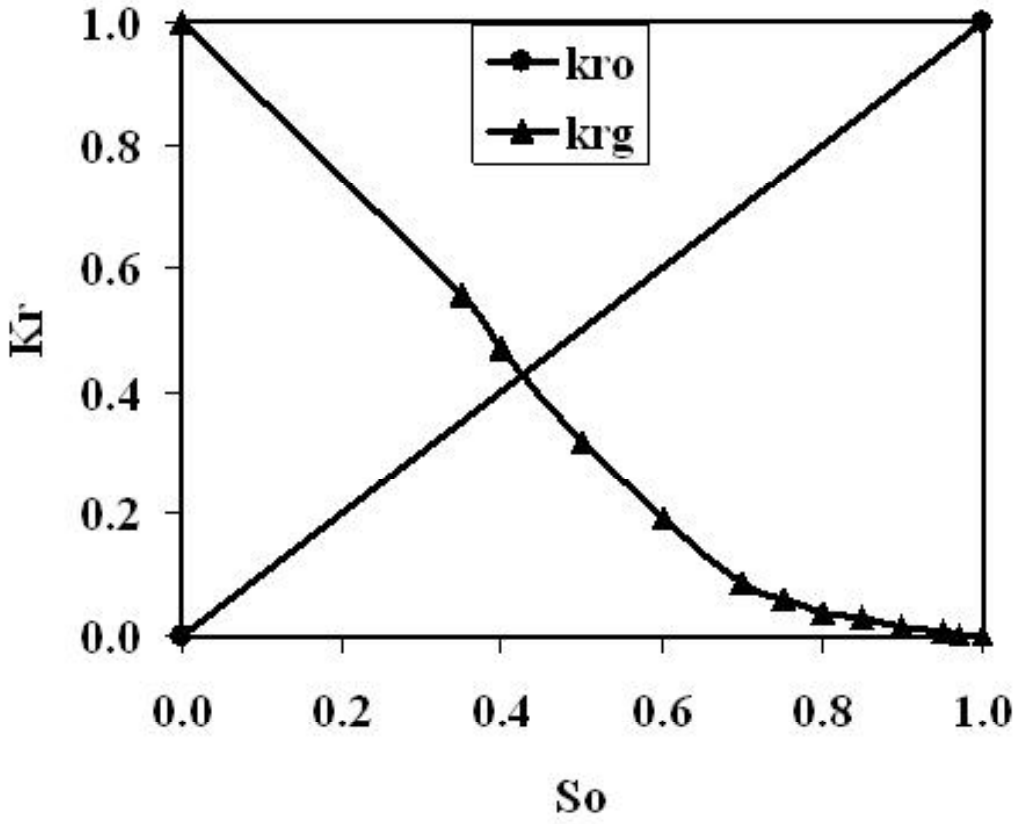

Figure 6.4. Relative permeability curve for a fracture-filled fault

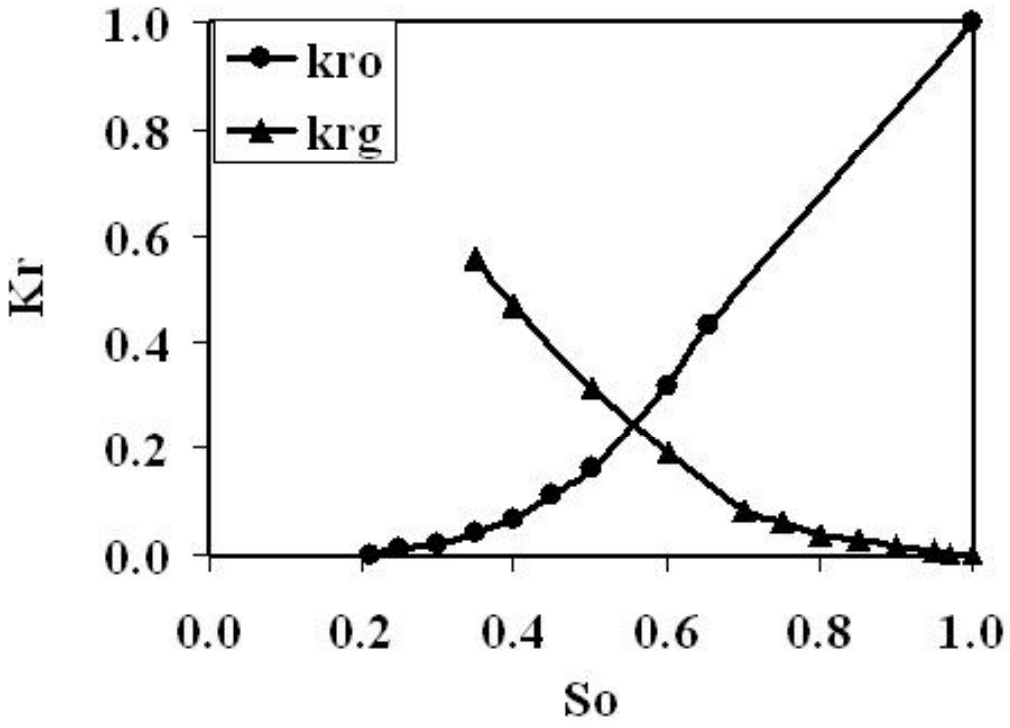

Figure 6.5. Relative permeability curve for a deformation band filled fault

CHAPTER 7

SETTING UP THE RESERVOIR SIMULATOR

Numerical simulations of CO_2 injection and migration in fresh-to-saline sandstone aquifers are performed to assess how unseen faults might compromise CO_2 sequestration. Presence or absence of these features (deformation bands or fractures) might have a great impact on the volume sequestered. Additionally, comparisons between various simulated results yields insight regarding the relative impact of different features (deformation bands or fractures) on the volumes sequestered. The results of simulated CO_2 supercritical fluid injection into a faulted sandstone aquifer reveal a typical distribution of free and dissolved CO_2 that should be anticipated during sequestration.

A black oil simulator, Eclipse®, was used for all the simulations. As this is a black oil type simulator, a two-phase gas-oil description was used to simulate CO_2 and water. Gas in the model was specified with CO_2 properties and oil was specified with water properties. This was necessary to describe the effect of the solubility of CO_2 in water.

The various reservoir scenarios for sequestration effects analyzed in the next sections are:

1. High and low permeability without seal
2. Horizontal wells
3. Stacked reservoirs with intervening horizontal seal
4. Low permeability sandstone reservoir
5. Impact of relative permeability relationships
6. Impact of capillary pressure relationships

7. Impact of permeability anisotropy within the fault zone
8. Large reservoir model

The model volume used in all of the above simulations except the stacked reservoirs with horizontal seal and large reservoir model is 600.5 feet by 420 feet in plan and 140 feet thick The simulation volume is assumed to be located near the tip of a normal fault with geometry similar to that seen in the outcrop at the Big Hole fault [36]. Vertical, impermeable faults are assumed to surround a sandstone aquifer that is sealed by low permeability rocks both above and below the aquifer. A 35 X 60 X 20 (42,000 grid blocks) Cartesian grid, is used for all simulations.

The 35 grid blocks in the X direction are of lengths 16 X 25, 3 X 15, 7.5, 5.0, 3.5, 2.25, 1.5, 1.0, 1.5, 2.25, 3.5, 5.0, 7.5, 15, and 4 X 25 feet. The 60 grid blocks in the Y direction are of lengths of 7 feet each. This makes the areal dimension of the field 600.5 X 420 feet. In the vertical (Z) direction, there are 20 layers of 7 feet each. A vertical, north-south trending fault is located 100 feet west of the injection well and fully penetrates the reservoir/aquifer (Figure 7.1). The fault is 15.5 feet wide. Fault grid blocks with sides as small as 1 foot are included in the model. Such fine grid blocks resolutions are needed to capture the small physical size of fault zone details.

Individual volumes of the reservoir are analyzed to determine how CO_2 is distributed throughout the entire reservoir. The reservoir is divided into three parts. The region between the injection well and faulted zone is termed as Zone-1, the faulted region as Zone-2, and the other part of the reservoir as Zone-3. The amount of CO_2 (both dissolved and free) sequestered in Zone-1 is an important indicator of how faults affect the aquifer filling behavior and is the focus of this study. Filling the greatest vertical extent of the aquifer is of key interest. In each of the above discussed scenarios, the same volume of CO_2 is injected; the difference shows up in the way that the CO_2 leaves Zone-1. This also yields insight regarding strategies for placing injection wells in the faulted aquifer.

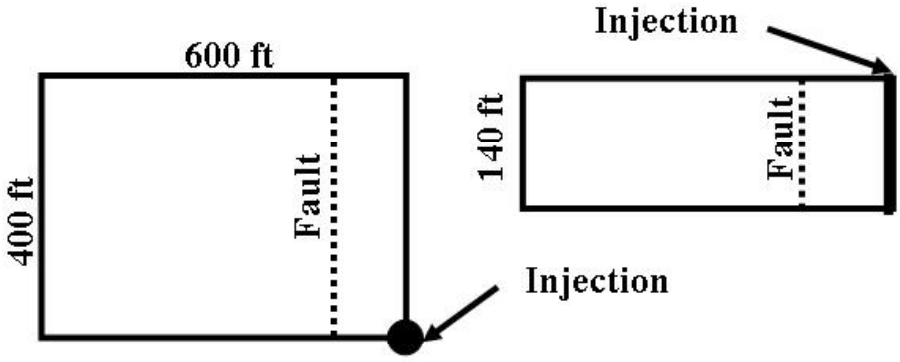

Figure 7.1. Top and front view of the reservoir simulation volume

7.1 Horizontal injection wells

The model volume in the reservoir with horizontal wells is similar to the above discussed volume except that there are a series of 5 drainage wells branching off from a horizontal well in the East-West direction as shown in Figure 7.2 .

7.2 Stacked reservoirs with intervening, horizontal seal

The model volume in the reservoir with a horizontal seal is similar to the above discussed volume in plan view, except the depth of the reservoir is 280 feet. This yields a 35 X 60 X 40 Cartesian grid, with a total of 84,000 grid blocks. In the vertical (z) direction, there are 40 layers of 7 feet each. The reservoir is basically divided into three sections, upper reservoir, sealed middle section, and lower reservoir, as shown in Figure 7.3. The lower reservoir is similar to the reservoir described previously for all the other cases (Figure 7.3). The thickness of the upper reservoir and middle seal is 70 feet each.

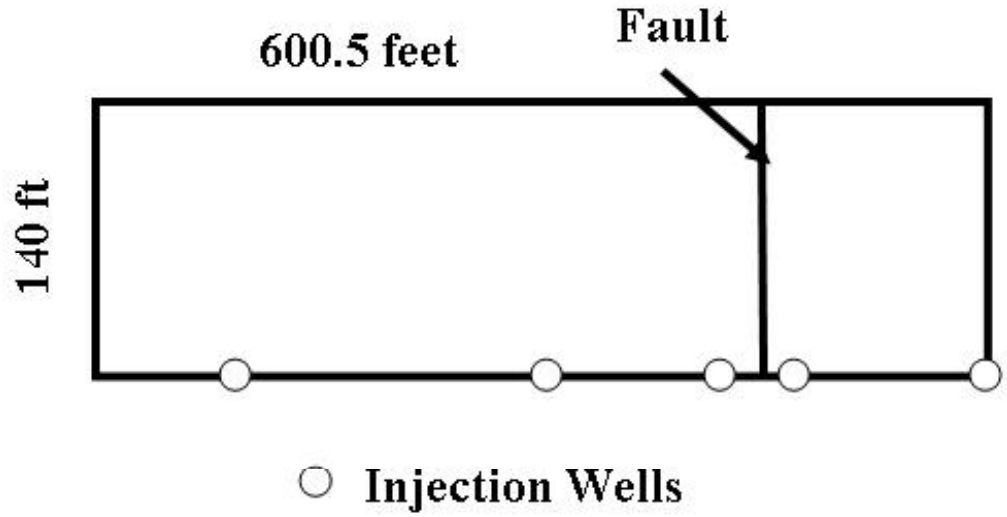

Figure 7.2. Front view of the reservoir simulator set-up in the reservoir with horizontal injector wells case

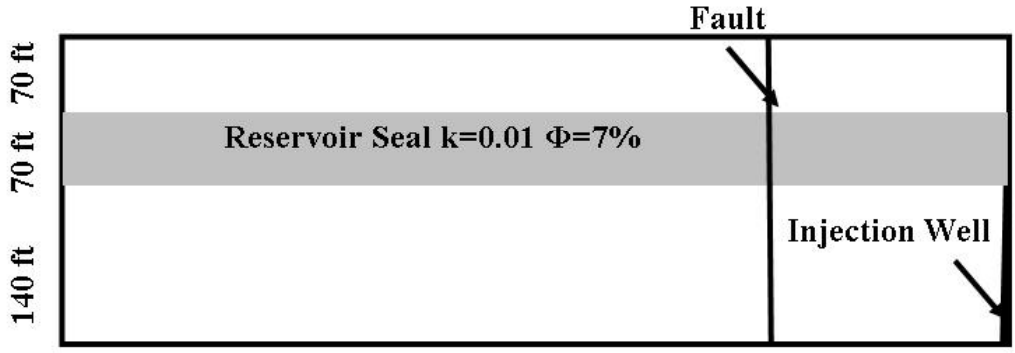

Figure 7.3. Front view of the reservoir simulator set-up in the reservoir with horizontal seal case

7.3 Large reservoir model

The total areal dimension of the larger reservoir is 1500 by 900 ft as shown in Figure 7.4. In this study, the simulator with a 48 X 30 X 14 (20,160 grid blocks) Cartesian grid is developed. As a reference, 600.5 X 420 feet aerial dimension is used, in order to compare the results with the smaller model. The 48 and 30 grid blocks are of lengths 18*50ft, 30*20ft in the X-direction and 10*50ft, 20*20ft in the Y-direction. In the vertical (Z) direction there are 14 layers of 10 feet each. A vertical, north-south trending fault is located 120 feet west of the injection well and fully penetrates the reservoir/aquifer. Injection is uniform and is selected to occur over the entire depth of the reservoir for 11 years. Injection is then stopped and the simulation is run for another 30 years. This is done to study CO_2 migration and storage after injection.

7.4 Reservoir fluid properties

The solubility of CO_2 in water found in sandstone aquifers is a function of temperature, pressure of CO_2, and salinity of the water. The likely temperature range for sequestration is from surface temperature of approximately 20 ^{0}C to a temperature of 80 ^{0}C at a depth of a few kilometers. Maximum CO_2 pressure would

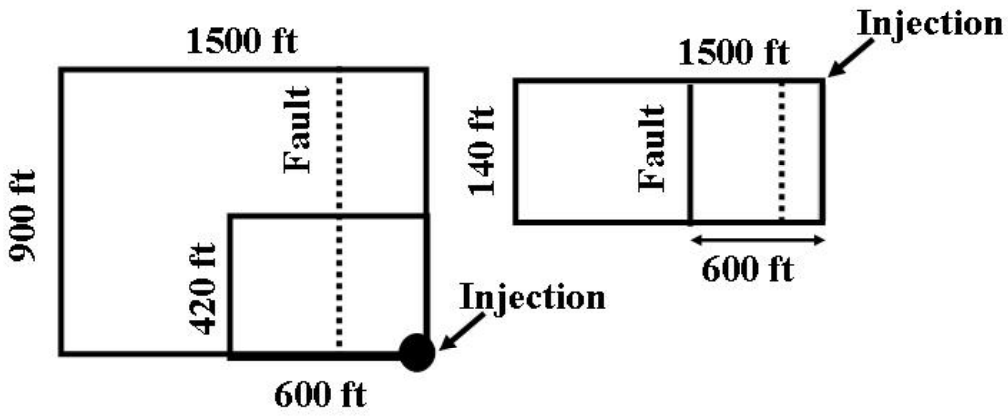

Figure 7.4. Top and front view of the large reservoir simulation model

be between hydrostatic and lithostatic pressure at the aquifer depth. CO_2 is a dense, supercritical fluid at temperatures and pressures considered here. CO_2 would occur as a dense, supercritical fluid phase, and as a dissolved constituent in ground water. The solubility of CO_2 is calculated in water using the equations and coefficients of the Drummond model [43]. Recently, an improved model for calculating CO_2 solubility in pure water and aqueous NaCl solutions from 273 to 533 K and from 0 to 2000 bar was proposed by Duan A and Sun R [44]. Modifying the simulations using the new model would not make much difference in the interpretation of the results in this study. The solubility of CO_2 decreases systematically as salinity increases [44]. Solubility increases with increasing pressure of CO_2. Fluid properties employed in these simulations are at a temperature of 60 ^{0}C (105F).

The project design is to inject the CO_2 waste from a 1000MW thermal power station, resulting in an average daily design injection rate of 100 MSCF/day. This rate is calculated by noting that 1lb mole of CO_2 occupies 379.4 SCF from real gas law at standard conditions. Thus, the injection well uses a rate constraint of 100 MSCF/day. Injection is uniform and is selected to occur over the entire thickness of 140 feet for 500 days, which means the total amount of gas injected is 50,000 MSCF (50 MMSCF). For the case where horizontal injection wells are used, 5 injectors are used to inject CO_2. In the horizontal sealed reservoir, injection is uniform and is selected to occur over the bottom part of the reservoir. The initial conditions in

the model were specified to be in equilibrium, with the initial pressure. The initial water saturation in the model is 100%.

CHAPTER 8

RESERVOIR SIMULATION RESULTS

A sequence of simulations was run to explore how faults/fractures may affect potential CO_2 sequestration.

8.1 High and low permeability faults without seal

Two end member cases for fault permeability structure were studied:

1. A high-permeability fault containing open fractures
2. A low-permeability fault containing deformation bands

The permeability and porosity of the two end member cases and the host rock are shown in Table 8.1. The base case is the homogeneous model with no faults. The two end member cases were analyzed and compared to the base case.

Figures 8.1, 8.2, 8.3, and 8.4 show the top and vertical views of dissolved and free CO_2 distribution, for a deformation band fault case, unfaulted, homogeneous, and isotropic sandstone case, and a fractured fault case after 100 days and 500 days. The injected gas spreads out laterally in the upper layers, since it has a tendency to migrate vertically upward in a liquid filled reservoir. The initial CO2 saturation is assumed to be zero.

Figures 8.1, 8.2, 8.3, and 8.4 clearly illustrate how various fault permeability structures can influence sweep efficiency. In the deformation band type fault (DB fault) case, the gas saturation is highest in the injection interval, the injected gas then finds the fault and migrates vertically upward along the deformation bands, and then spreads out at the top of the reservoir model. As the DB fault acts as a barrier to fluid flow, the injected CO_2 tends to migrate to the bottom layers, since it cannot migrate across the fault easily. This is clearly seen from the vertical view, where the DB fault tends to fill in the bottom layers between the injection

Table 8.1. Permeability and Porosity properties in the three cases where md = milli Darcy.

Case	Permeability (md)	Porosity
Host Rock	500	20%
DB filled Fault	0.05	7%
Fracture filled fault	50000	25%

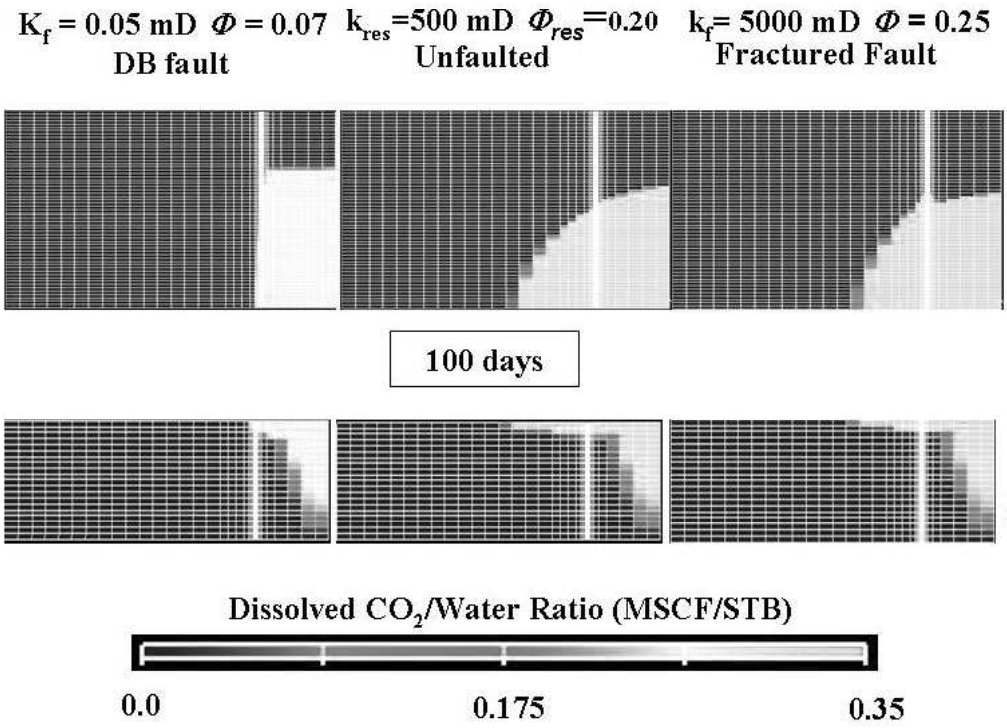

Figure 8.1. Dissolved CO_2 distribution after 100 days of low k, no fault, and high k fault.

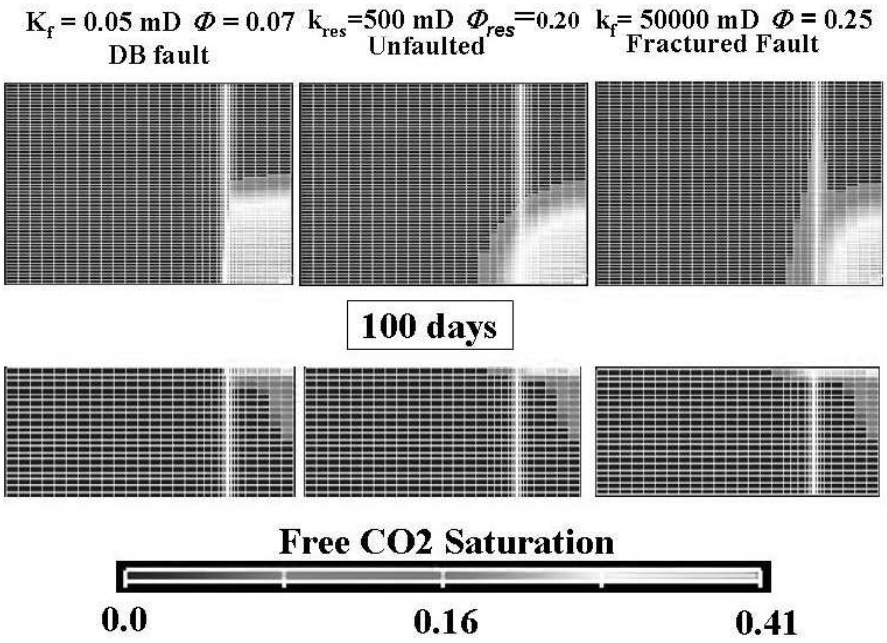

Figure 8.2. Free CO_2 distribution after 100 days of low k, no fault, and high k fault.

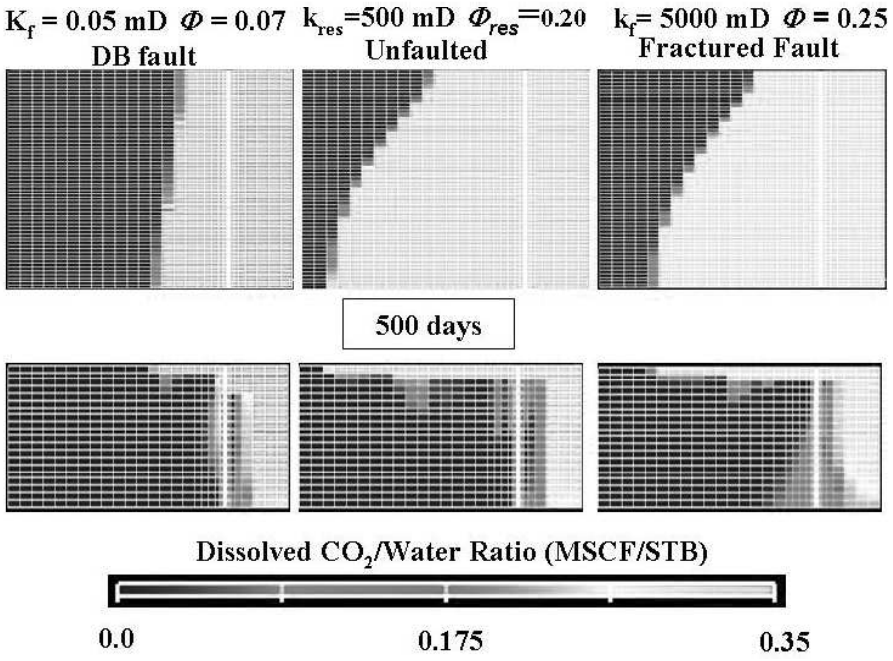

Figure 8.3. Dissolved CO_2 distribution after 500 days of low k, no fault, and high k fault.

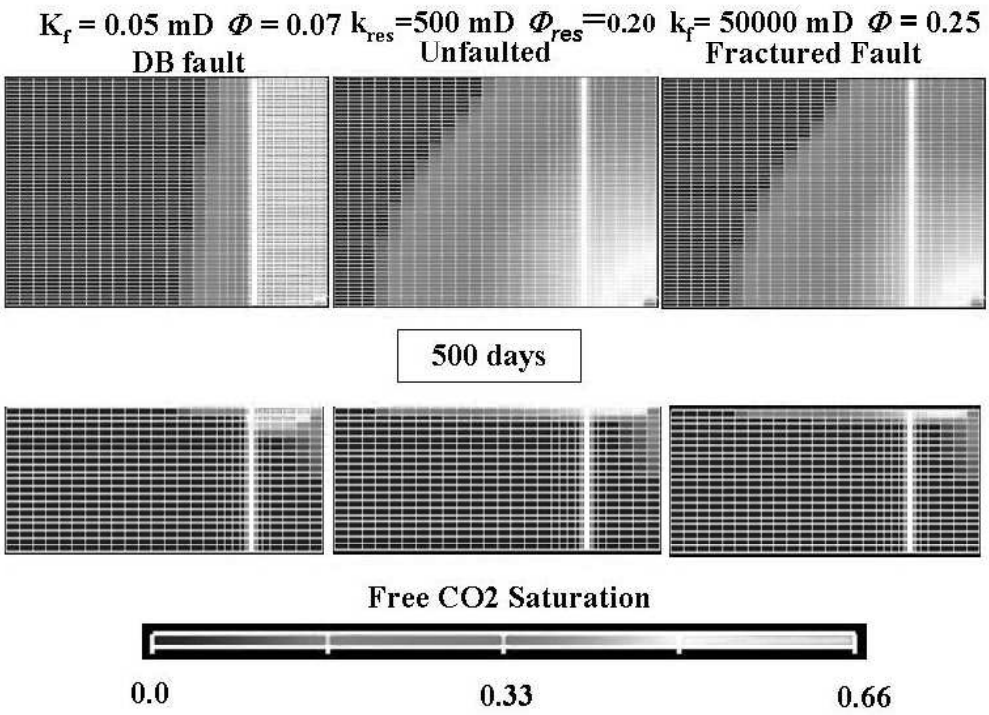

Figure 8.4. Free CO_2 distribution after 500 days of low k, no fault, and high k fault.

well and the fault. Whereas in the fractured fault (high permeability fault), gas migrates across and along the fault and fills the other part of the reservoir model. The injected gas in the fractured fault scenario flows across the fault and sweeps the top layer. When a fractured fault is encountered closer to the injection well, not much of the volume between them fills up with CO_2.

Figure 8.5 shows dissolved and free gas distribution of the reservoir in Zone-1. Table 8.2 shows amount of dissolved and free gas distribution in Zone-1 of the reservoir. In order to evaluate the geochemical effects on rocks, it is necessary to know the amount of CO_2 stored as a dissolved phase in the water and as free CO_2.

The amount of dissolved and free gas in the fractured fault and the unfaulted case are not very different. For a DB fault scenario, 75% of the injected gas both in the dissolved and free states is in Zone-1. The remaining 25% is distributed between Zones 2 and 3. This is because the DB fault acts as a barrier to the fluid flow and does not allow the injected gas to migrate to Zone-3 of the reservoir. This helps

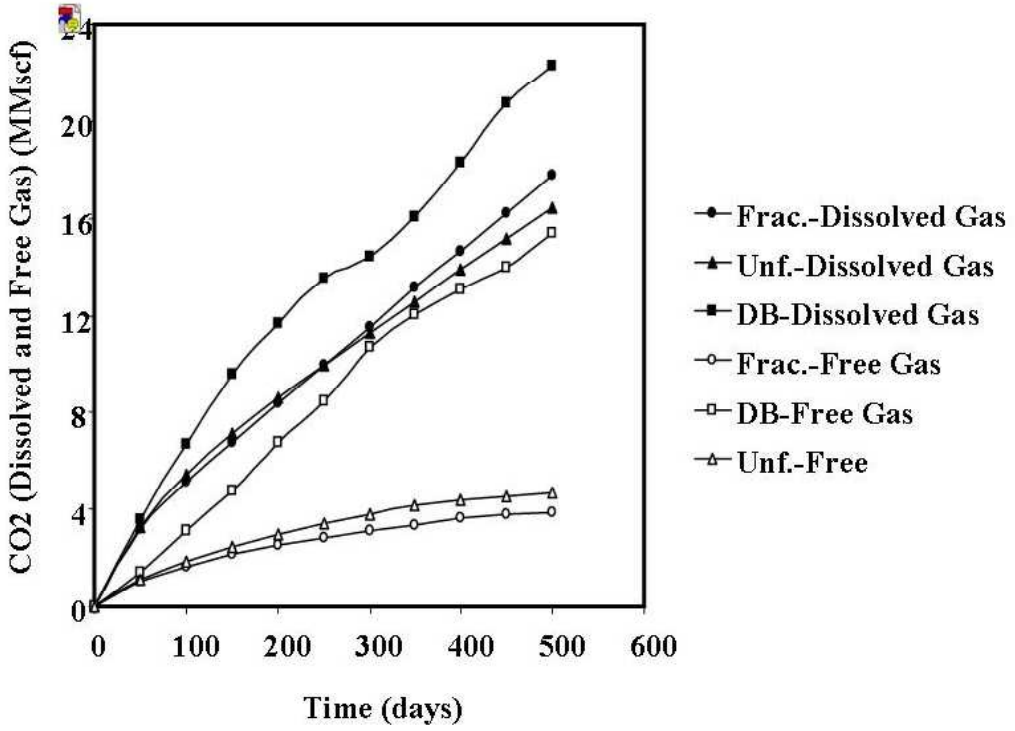

Figure 8.5. Dissolved and Free CO_2 distribution for Zone-1 of the reservoir where, 'Frac' = Fractures , 'DB' = Deformation bands, and 'Unf.' = Unfaulted

Table 8.2. Dissolved and Free Gas in DB filled faults, fractured filled faults, and the Unfaulted case for Zone-1 where 'Ttl'=total, 'Diss'=dissolved.

Case	Diss Gas (MMSCF)	Free Gas (MMSCF)	Ttl Gas (MMSCF)	% Diss Gas	% Free Gas	% Ttl CO_2
Unfaulted	16.45	4.65	21.1	77.97	22.03	42.2
DB filled fault	22.27	15.39	37.66	59.14	40.86	75.32
Fracture filled fault	17.75	3.89	21.64	82.02	17.98	43.28

increase the amount of CO_2 in the region between the fault and the injection well. This is also the main cause for more free gas in a DB fault case. The Zone-1 region has reached maximum gas saturation and would not allow for any more dissolution of injected CO_2, hence results in more free gas in this scenario. The fractured fault allows for gas to flow across the fault and hence, not much of the Zone-1 region is filled up.

From the above results, it is clear that faults affect the fill-up of the gas (CO_2) differently in different parts of the reservoir volume. Presence of DBs increases the amount of CO_2 filled up in Zone-1 of the reservoir volume. The fluid flow in the fractured fault is not very different from the unfaulted case.

Thus, the deformation bands zones restrict flow in the reservoir and compartmentalize the reservoir. Presence of DBs in a reservoir definitely increases the amount of CO_2 sequestered. The DB fault aids in filling up the bottom layers of the reservoir, which is also another advantage from a sequestration point of view. Filling up the bottom layers does not allow for leakage into the atmosphere that is another issue discussed in the next section. The DB faults should be effective sealing layers, thereby avoiding CO_2 leakage into the atmosphere.

The amount of CO_2 sequestered in a fractured fault is similar to that of an unfaulted case. Hence, presence/absence of fractures will have little/no impact on the amount of CO_2 sequestered in this particular scenario except in the case of breaking an upper reservoir seal. The vertical migration as a free phase through fractures could cause the leakage of CO_2 to the atmosphere. This is discussed in detail in Section 8.3.

Figure 8.6 shows the comparison of bottom-hole pressure (BHP) in the above-discussed three scenarios. BHP builds up more rapidly in the DB fault case than the other two cases. Hence, injection has to be stopped earlier in this case because the zone is over-pressured during gas injection/storage operations. The next section will show how horizontal wells can help maximize CO_2 storage operations.

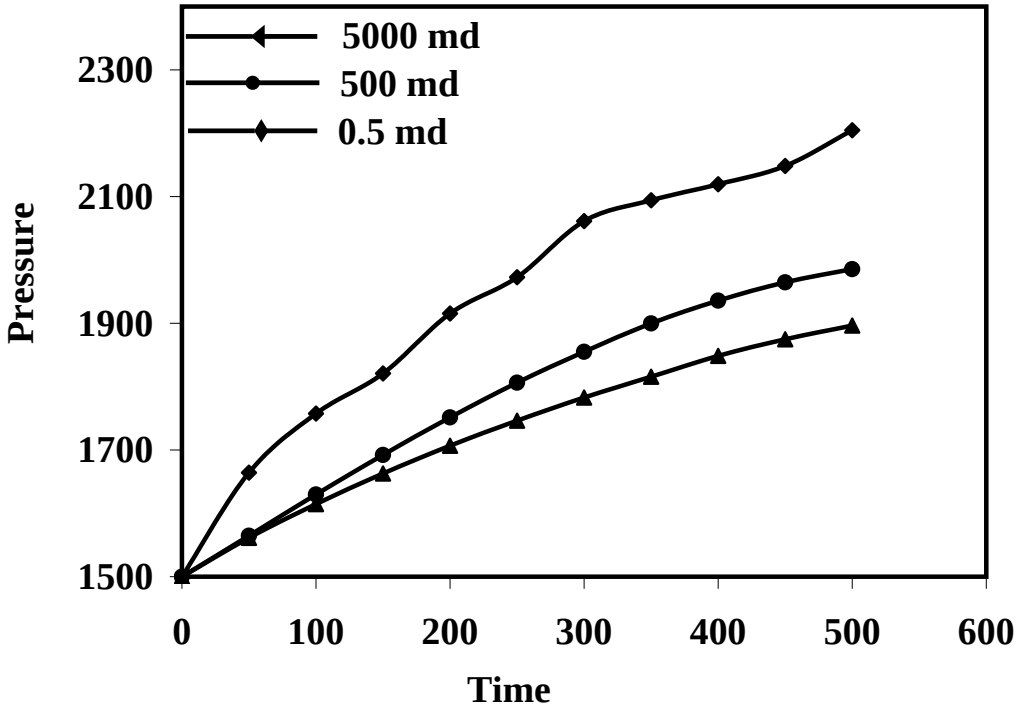

Figure 8.6. Bottom Hole Pressure of low k, no fault, and high k fault.

8.2 Horizontal well injection studies

Horizontal wells are normally used to increase the injectivity in the sequestration process. In the previous section, the bottom hole pressure builds up rapidly in a low permeability deformation band fault case. Injecting CO_2 through horizontal wells would reduce this pressure build up and also increase CO_2 storage.

This section discusses in detail the distribution of CO_2 when horizontal wells are used for injection. The total amount of gas injected for 500 days is 50,000 MSCF (50 MMSCF). Similar reservoir properties were used as in the previous section. The low-permeability fault containing deformation bands is studied in detail here and compared with the scenarios in the previous section with vertical wells.

Figure 8.7 shows the comparison of the dissolved and free gas distribution between horizontal and vertical wells in Zone-1. The amount of dissolved and free gas in the horizontal injection is lower than when vertical wells are used. Horizontal wells aid in CO_2 injectivity in the reservoir by reducing the pressure build up. Figure 8.8 shows the BHP distribution in Zone-1. Injecting CO_2 through horizontal wells

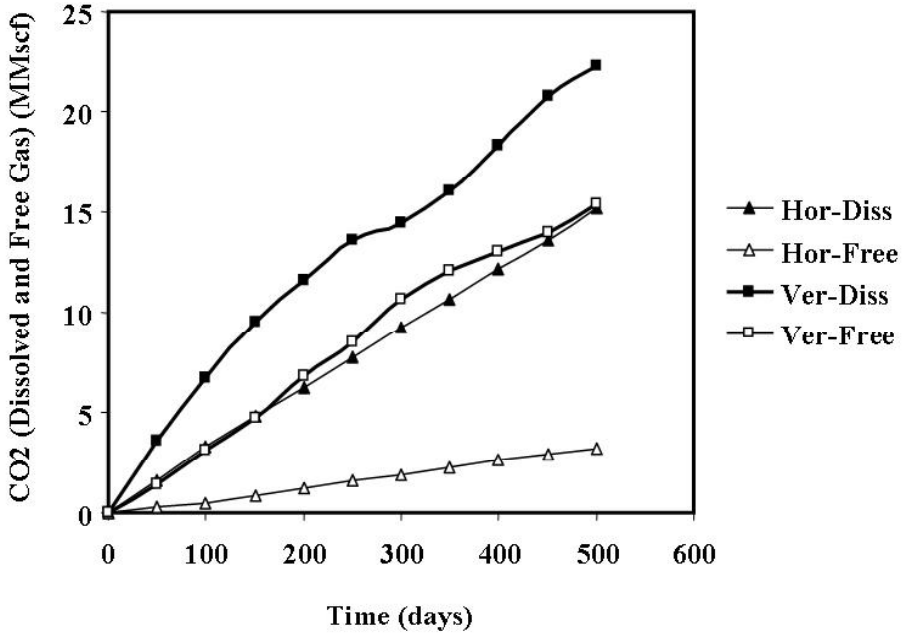

Figure 8.7. Dissolved and Free CO2 distribution for Zone-1 of the reservoir in a deformation band fault case where, 'Hor' = Horizontal Wells, 'Diss' = Dissolved Gas , and 'Ver' = Vertical Wells

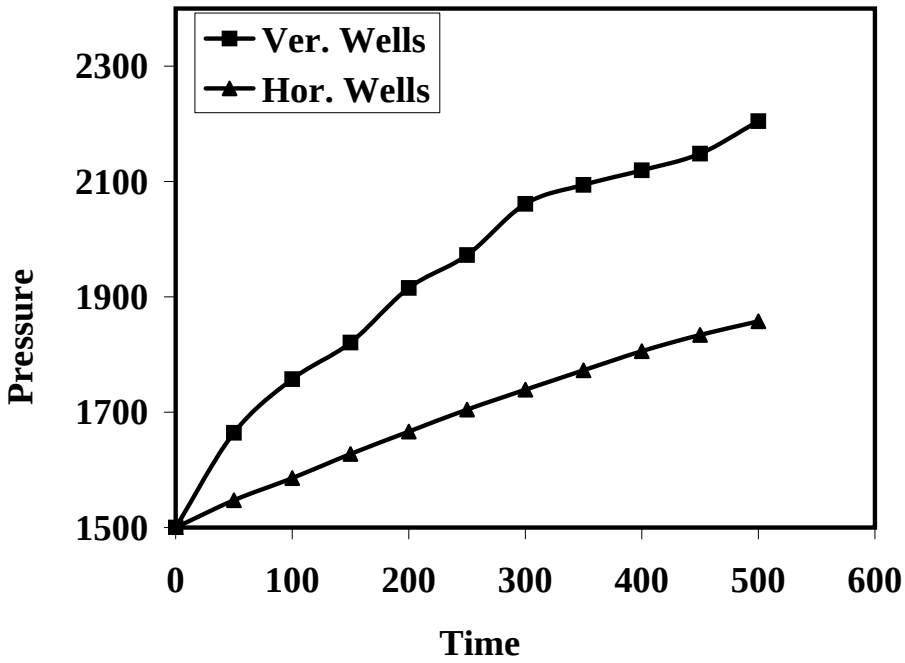

Figure 8.8. Bottom Hole Pressure (BHP) Distribution in the deformation band fault case where 'Ver' = Vertical and 'Hor' = Horizontal

reduces the pressure build up and also increases CO_2 storage.

8.3 Stacked reservoirs with intervening, horizontal seal

The success of CO_2 sequestration by deep injection depends on the ability of upper and lateral seals to confine the overpressured fluid. One potentially serious problem associated with injection into underground formations is the possible leakage of injected CO_2 through or along faults. Over long time scales, these faults/fractures may serve as short-circuit pathways for ultimate leakage into the atmosphere. This is of great concern because leakage of CO_2 in large quantities would compromise safety as well as the objectives of sequestration.

This section discusses in detail the impact of faults on CO_2 leakage to the atmosphere. Permeable fault-related fractures in sandstone can focus CO_2 flow to leakage points where permeable faults breach reservoir-sealing units and enable injected CO_2 to leak towards the ground surface. On the other hand, low-permeability faults can restrict access to fault-bounded CO_2 sequestration volumes.

The total amount of gas injected for 500 days is 50,000 MSCF (50 MMSCF). The top and the bottom layers have the same reservoir properties which match the properties assigned in the previous simulation series. Also, similar permeability and porosity properties were used as in Section 8.1. The sealed middle layer has a permeability and porosity of 0.01md and 7%. The two end member cases for fault permeability structure as discussed earlier were studied, the high-permeability fault containing open fractures and the low-permeability fault containing deformation bands.

Figures 8.9, 8.10, 8.11, and 8.12 show the top and vertical views of dissolved CO_2 distribution for a deformation band and fractured fault case after 100 and 500 days. The injected gas spreads out in the bottom layers and does not escape into the top reservoir due to reservoir seal. A low permeability fault even though cut across the entire reservoir does not allow any leakage of CO_2 into the atmosphere.

Figure 8.13 indicates the volume of CO_2 sequestered in the three layers. In the fractured fault case, CO_2 has leaked to the top layer as opposed to in the

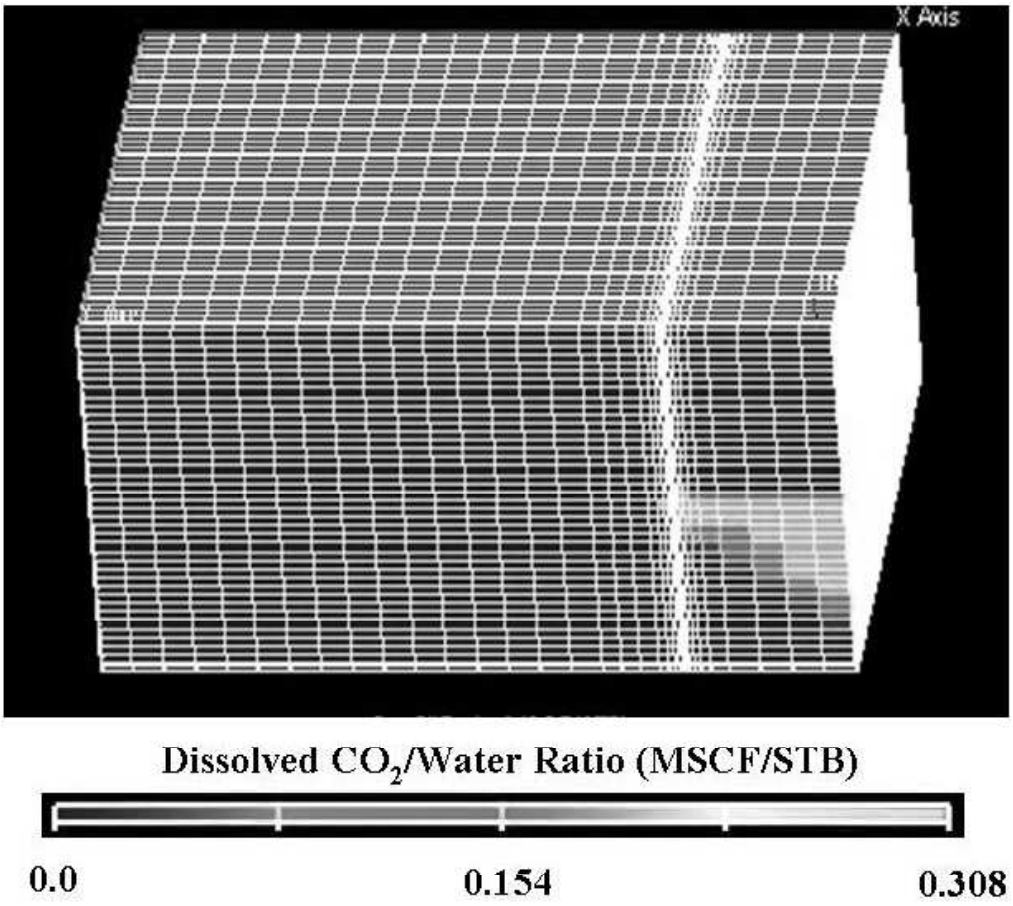

Figure 8.9. Dissolved CO2 distribution in a stacked reservoir system after 100 days for a deformation band fault case.

deformation band fault. The fractured fault broke the seal and migrated into the top layer. About 22.75% of the injected CO_2 has leaked into the upper layer in the fractured fault case, thereby allowing for possible leakage into the atmosphere. On the other hand, in the deformation band fault, 87.3% of the CO_2 resided in the bottom layer. Basically, there is negligible CO_2 migration into the top layer in this case. Hence, the DB fault almost has no leakage into the atmosphere as opposed to the fractured fault.

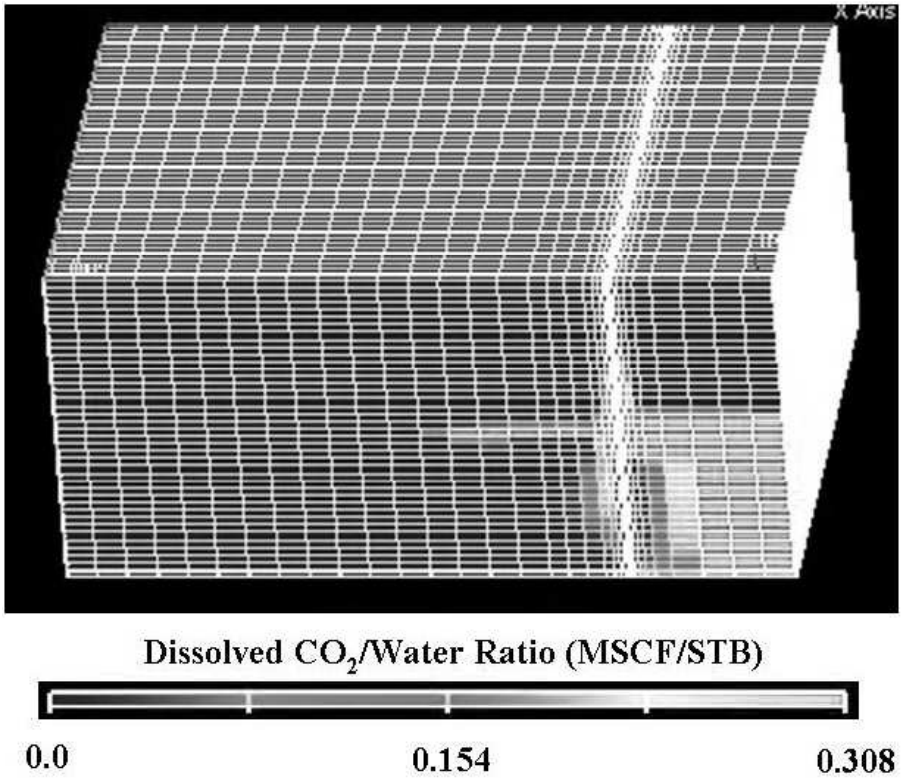

Figure 8.10. Dissolved CO2 distribution in a stacked reservoir system after 500 days for a deformation band fault case.

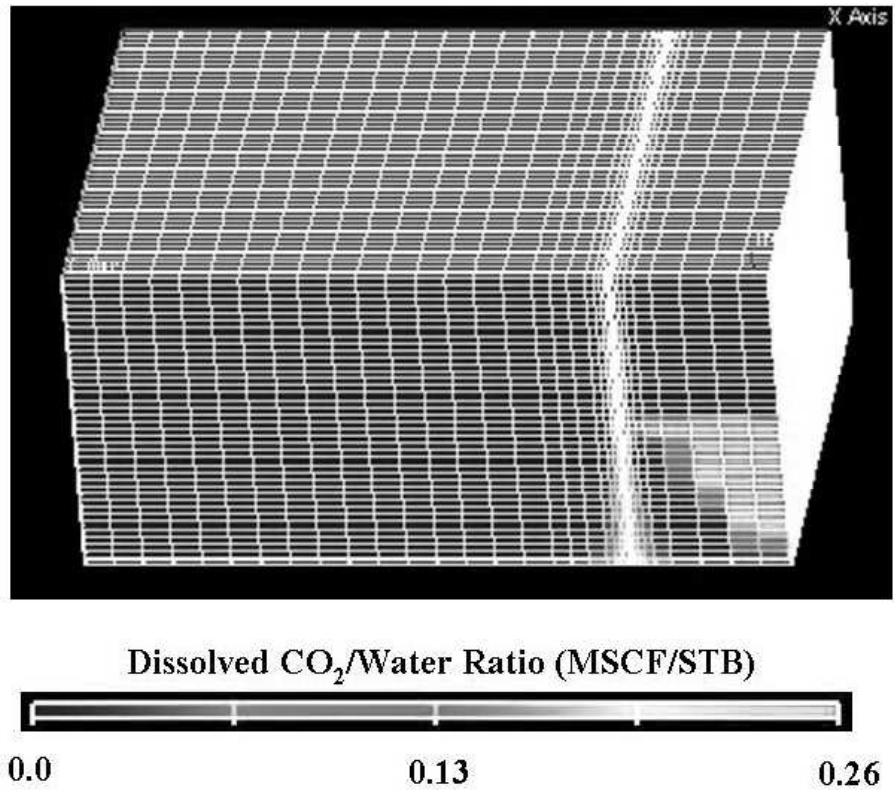

Figure 8.11. Dissolved CO2 distribution in a stacked reservoir system after 100 days for a fractured fault case.

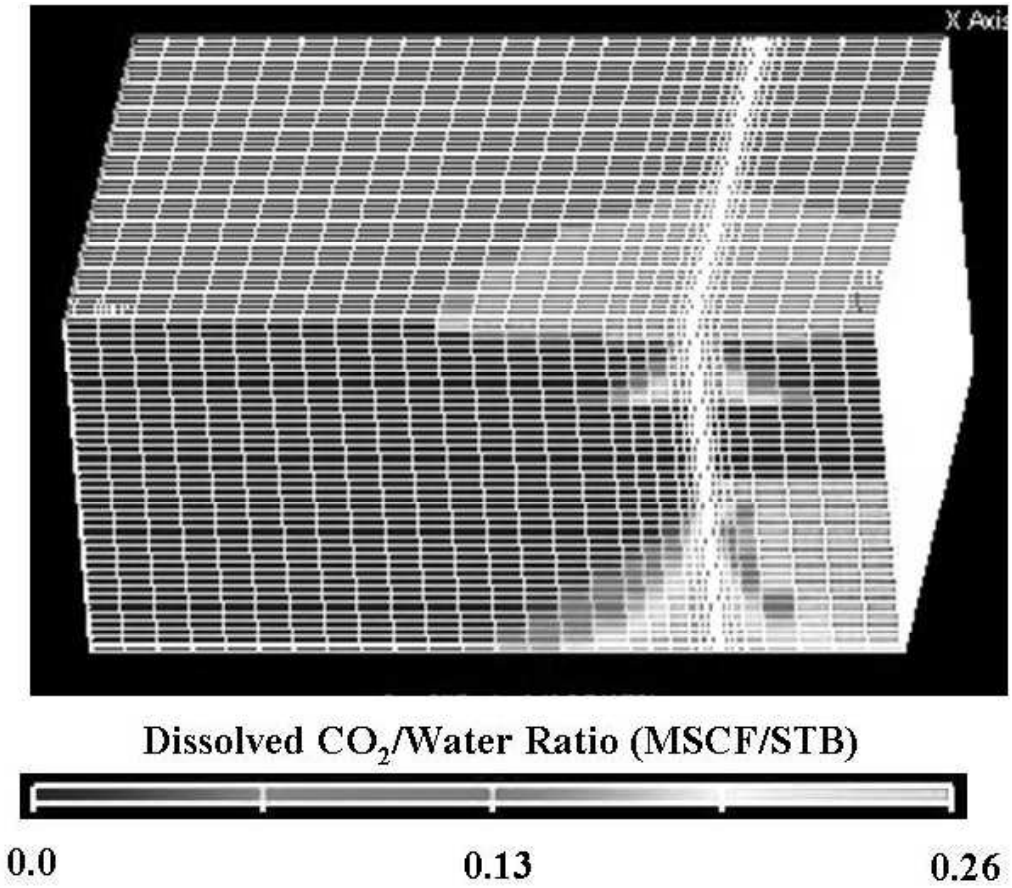

Figure 8.12. Dissolved CO2 distribution in a stacked reservoir system after 500 days for a fractured fault case.

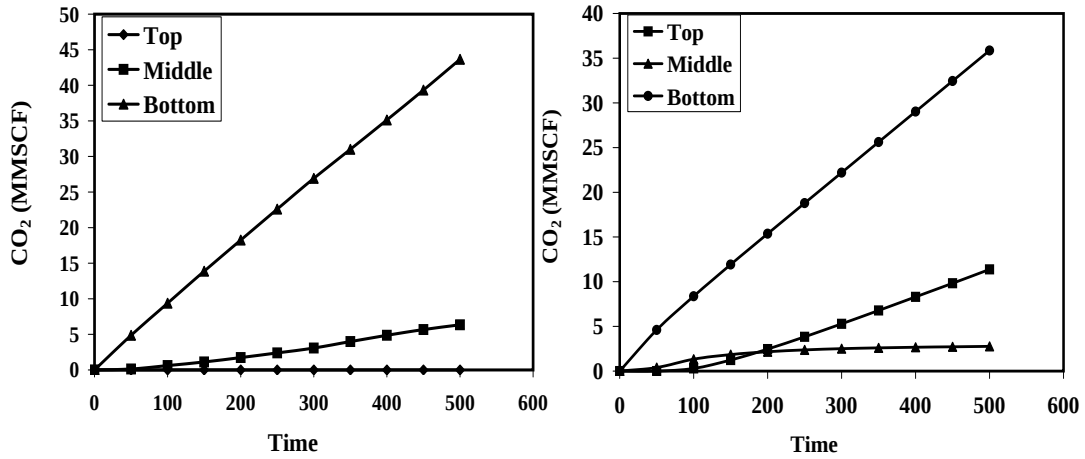

Figure 8.13. Volume of CO2 sequestered in the top, middle, and bottom layers in a deformation band, and a fractured fault case.

8.4 Low permeability sandstone reservoir

The strategy employed in the above discussed sandstone reservoir domain to evaluate fault scenarios is repeated for a low permeability sandstone reservoir. Geologically, it is unlikely that deformation bands form in sandstone with porosity less than 12%. Hence, it would not be logical to analyze a low permeability fault in a low permeability sandstone reservoir and hence, a high permeability fault case is analyzed and compared with the earlier discussed cases for a high permeability sandstone reservoir. This is to study the effect of decreasing/increasing the permeability of the sandstone reservoir (host rock).

A homogeneous isotropic low permeability sandstone reservoir is considered with a permeability and porosity of 5 md and 10%, respectively. In the previous cases, a reservoir with permeability and porosity of 500 md and 20% is considered. The permeability of the permeable, fracture-filled fault is assumed to be 5000md in both cases. The corresponding fault porosity values are calculated from our previous studies and are 12% and 22% for the 5 md and the 500 md scenarios.

Figure 8.14 shows the amount of CO_2 sequestered (both in the dissolved and free states) for the two cases of 5 md and 500 md host rock permeability with a fractured fault case for Zone-1. Table 8.3 illustrates the amounts of CO_2 sequestered.

The amount of dissolved gas in a 500md host rock case is relavtively more compared to the low permeability 5md rock case. The lower porosity of the lower permeability case cannot hold more CO_2 hence less dissolved gas and more free gas in this case.

The total amount of gas (dissolved and free) sequestered is higher in the 5md rock compared to the 500md host rock in Zone-1. This is because, in the 500md host rock case, the CO_2 gas reaches the fault faster and flows across the fault into the other compartment. Whereas in the 5md rock, CO_2 takes longer time to reach the fault because of lower porosity of the sandstone rock and hence restricts flow of CO_2 from Zone-1. Also, increasing the host rock permeability increases the amount of dissolved gas and reduces the free gas.

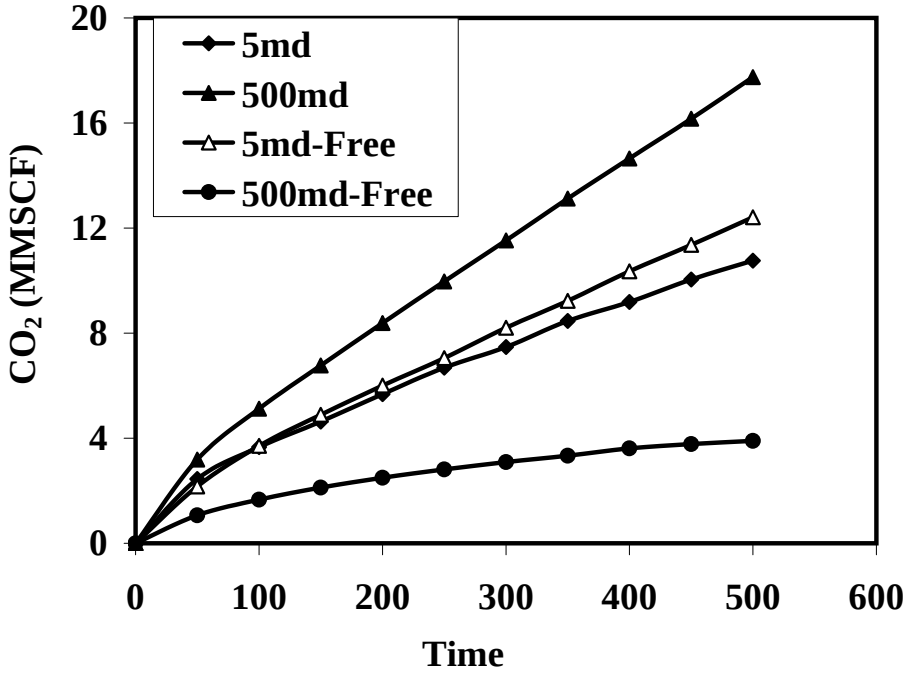

Figure 8.14. Total (Dissolved and Free) CO2 distribution for Zone-1 of the reservoir

Table 8.3. Dissolved and Free Gas in 5md and 500md host rock cases for Zone-1 where 'Ttl'=total, 'Diss'=dissolved

Case	Diss Gas (MMSCF)	Free Gas (MMSCF)	Ttl Gas (MMSCF)	% Diss Gas	% Free Gas	% Ttl CO_2
5md	10.76	12.41	23.17	46.4	53.6	46.34
500md	17.75	3.89	21.64	82.02	17.98	43.28

8.5 Impact of relative permeability relationships

In the simulation results illustrated in Figures 8.1 through 8.5, a single relative permeability relationship was used for both the host rock and the fault (termed as the 'single case'). In the next series of simulations, different relative permeability relationships were assigned for both host rock and fault rock (termed as the 'multiple case'). The same capillary pressure relationships were assigned in all cases.

The goal here is to illustrate the effect of relative permeability curves on the amount of CO_2 sequestered. The two end member fault scenarios discussed earlier are considered. Similar permeability and porosity properties were used as discussed in Section 8.1. The relative permeability curves discussed in Section 6.2 (Figures 6.3, 6.4, and 6.5) are used for the host rock, deformation band faults, and fractured faults, respectively. During gas injection, the residual water saturation S_wr is the most sensitive parameter. From the above figures, the Swr for host rock is 0.3, deformation band fault is 0.22, and fractured fault is 0.0.

Tables 8.4 and 8.5 show the dissolved and free gas in zone-1 for a deformation band filles and fracture-filled fault with single and multiple relative permeability curves. Figure 8.15 illustrates the dissolved and free gas distribution in Zone-1 for a fractured filled fault and a deformation band filled fault scenarios. It is obvious that in a deformation band scenario, there is not a significant change in the dissolved and free gas, distributions for the single and multiple cases.

The residual water saturation for a single and multiple cases in the fractured

Table 8.4. Dissolved and Free gas in zone-1 for a fracture-filled fault with single and multiple relative permeability curves where 'Ttl'=Total and 'Diss'=Dissolved

Case	Diss Gas (MMSCF)	Free Gas (MMSCF)	Ttl CO_2 (MMSCF)	% Diss Gas	% Free Gas	%of Ttl CO_2
Single	17.75	3.89	16.65	56.51	43.49	33.3
Multiple	9.41	7.24	17.98	82.02	17.98	43.28

Table 8.5. Dissolved and Free gas in zone-1 for a deformation band-filled fault with single and multiple relative permeability curves

Case	Diss Gas (MMSCF)	Free Gas (MMSCF)	Ttl CO_2 (MMSCF)	% Diss. Gas	% Free Gas	%of Ttl CO_2
Single	22.27	15.39	37.66	59.14	40.86	75.32
Multiple	22.24	16.42	38.66	57.52	42.48	77.32

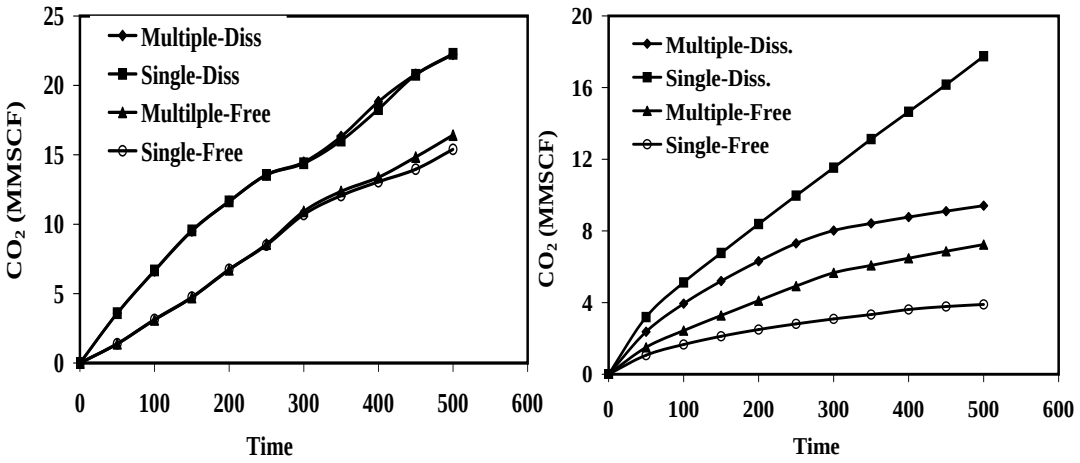

Figure 8.15. Dissolved and Free CO2 distribution in zone-1 for a deformation band and a fractured filled fault scenario where 'Diss' = Dissolved Gas for both single and multiple relative permeability curves.

fault scenario is 0.3 and 0.0. As gas displaces formation water, the residual water will be saturated with CO_2, and so a greater Swr value allows for more dissolved gas and less free gas, whereas in a deformation band fault scenario, the residual water saturation for the single and multiple cases are 0.3 and 0.22. Since the Swr values in the deformation band fault case for single and multiple cases are not very different, there is not much difference in the dissolved and free gas distributions for these cases.

These illustrate the effect of changing the relative permeability curve, and

this is found to be the most important factor. The dissolved gas changes from 35.5% in a single case to 44.55% in a multiple curves scenario. This clearly indicates that relative permeability curves do have an impact on the amount of CO_2 sequestered. Hence, there is a need for laboratory core flood measurements to reduce the uncertainty in the simulation.

8.6 Impact of permeability anisotropy within the fault zone

Permeability measurements in most reservoir rocks are dependent on the direction. The realistic characterization of reservoirs is not an easy task and must include the study of directional variation of permeability.

8.6.1 Homogeneous, anisotropic fault zone permeability

To study the effect of fault zone anisotropy, two categories of studies were performed and analyzed:

1. Firstly, an isotropic permeability case is compared with anisotropic scenario where the permeability is changed within the fault in each of the three orientations (keeping the other two constant) that is adding fault parallel and perpendicular features to determine the dominant directional flow.
2. Secondly, a scenario where the fault architecture is comprised of a high-low-high permeability (isotropic) fault elements. This is compared with the case where the equivalent effective permeability is determined in the three directions that leads to anisotropy.

In the first category, a deformation band type fault is analyzed. Initially, the number of deformation bands in the x-direction is 40 which leads to a permeability of 0.05md, one each in the y-direction and z-direction (permeability of 333.22md), which indicates that there are 40 deformation bands in the plane perpendicular to the z-y plane, one each in the plane perpendicular to the x-y and z-x planes. Geologists suggest that the highest density of deformation bands would be sub-parallel to the fault (x-direction). All of these studies were performed to determine the direction in which the features (DBs/ Fractures) would be dominant and how

they affect the fluid flow. Table 8.6 shows results of the three cases.

Analysis of individual volumes of the reservoir is done to determine how the gas is distributed throughout the entire reservoir like in the previous sections. Figure 8.16 illustrates the dissolved and free gas distributions in Zone 1 of the reservoir. The dotted line in the graphs represents the distributions for the isotropic case in a deformation band type fault.

From the distributions, it is clear that the dissolved and free gas distribution in both the cases closely resemble the isotropic case. Even though the number of features were increased in the other two directions for Case-2, there is very little or no impact on the flow distributions. The number of features in the parallel to the fault (x-direction) has the most impact on the distribution in case of deformation band type faults. Increasing or decreasing the number of features perpendicular to the fault would have little or no impact on the fluid flow in the DB fault case. Therefore, increasing the number of features in the parallel to the fault (x-direction), flow is restricted and has the greatest impact on fluid flow.

Table 8.6. Permeability and Porosity properties of all the three cases where md = milli Darcy, No. = Number, DBs = Deformation Bands, k = Permeability

	Case-1		Case-2		Case-3	
	No. of DBs	k	No. of DBs	k	No. of DBs	k
X	40	0.05	40	0.05	40	0.05
Y	1	333.22	10	83.26	40	0.05
Z	1	333.22	10	83.26	40	0.05

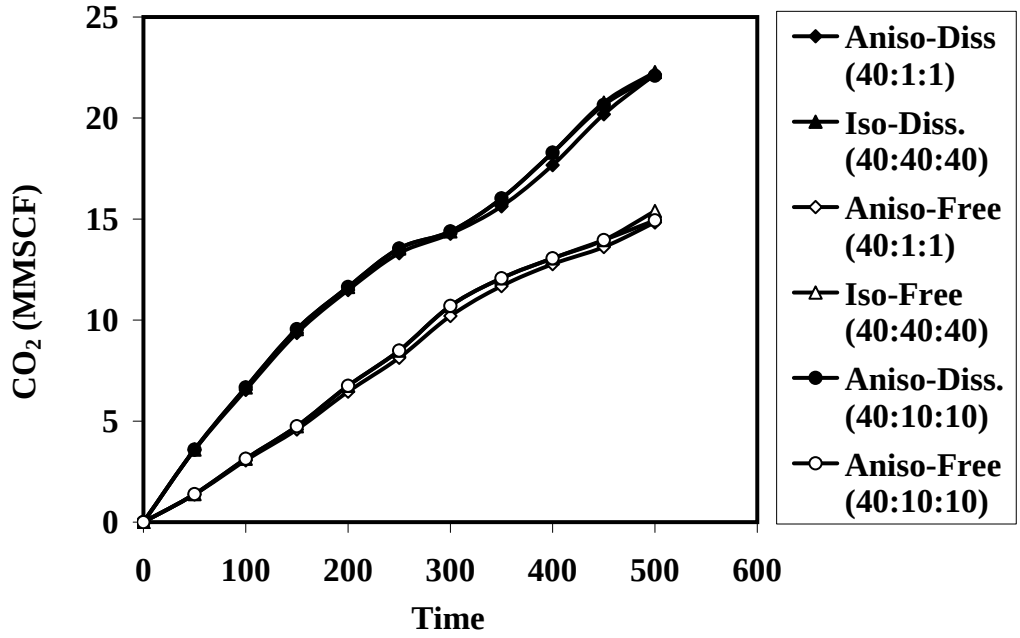

Figure 8.16. Dissolved and Free CO2 distribution for Zone-1 of the reservoir for the isotropic and the two anisotropic cases in a deformation band fault where, 'Aniso'= Anisotropic , 'Iso' = Isotropic, and 'Diss.' = Dissolved

8.6.2 Conduit barrier faults

Fault zone architecture and permeability structures are a primary control on fluid flow in fault zones. As we have seen in the previous sections, injecting CO_2 into a homogeneous oil reservoir causes a complicated series of interactions between CO_2 and water. Injecting CO_2 into a reservoir with fault-derived heterogeneity leads to more complicated fluid interactions. These fault-scale interactions can play an important role in determining CO_2 sequestration.

Faults are comprised of damage elements. Figure 8.17 clearly describes the conduit-baffle type fault and also reflects the nature and distribution of damage elements. The fault is comprised of dark brown features that indicate low permeability fault and the white features indicate high permeability fault. These fault structures together form a fault zone.

The model volume used in the simulations is similar to the previous simulations discussed earlier. The width of the fault is 15.5 feet and is divided into three zones with high-low-high permeability as described in Figure 8.18. The width of each

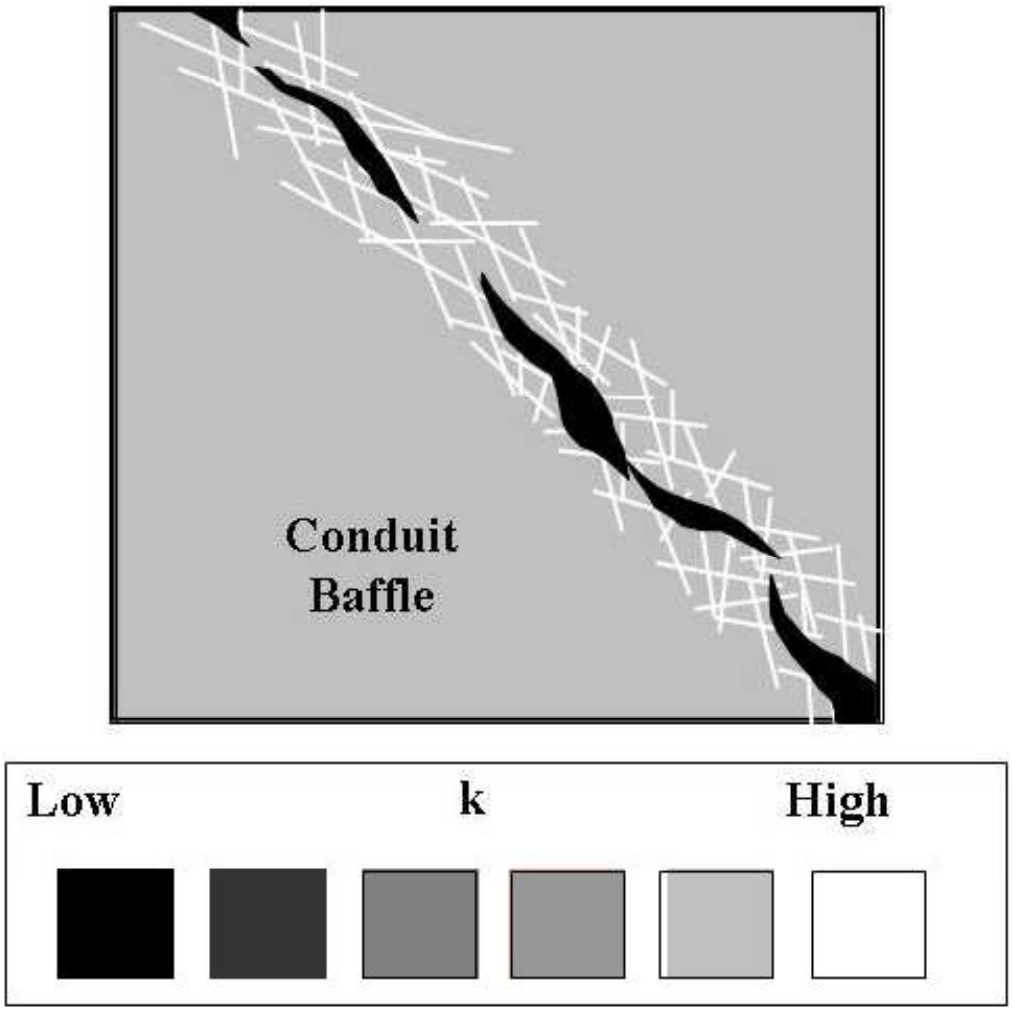

Figure 8.17. Conduit-Baffle fault

zone is 5.75ft, 4.0ft, and 5.75ft, as described in the figure.

In this study, two scenarios were compared and examined. Firstly, a case where the fault is a high-low-high permeability fault and the respective properties (permeability and porosity) were given to the respective zones of the fault as described above and is termed as Case-1. In the next scenario, Case-2, an equivalent permeability is computed. Using the host sandstone permeability, slip fractures, and deformation band permeability, an equivalent k1, k2, k3 is computed. Table 8.7 shows the permeability and porosity properties of the host rock and fault, for the conduit barrier fault cases.

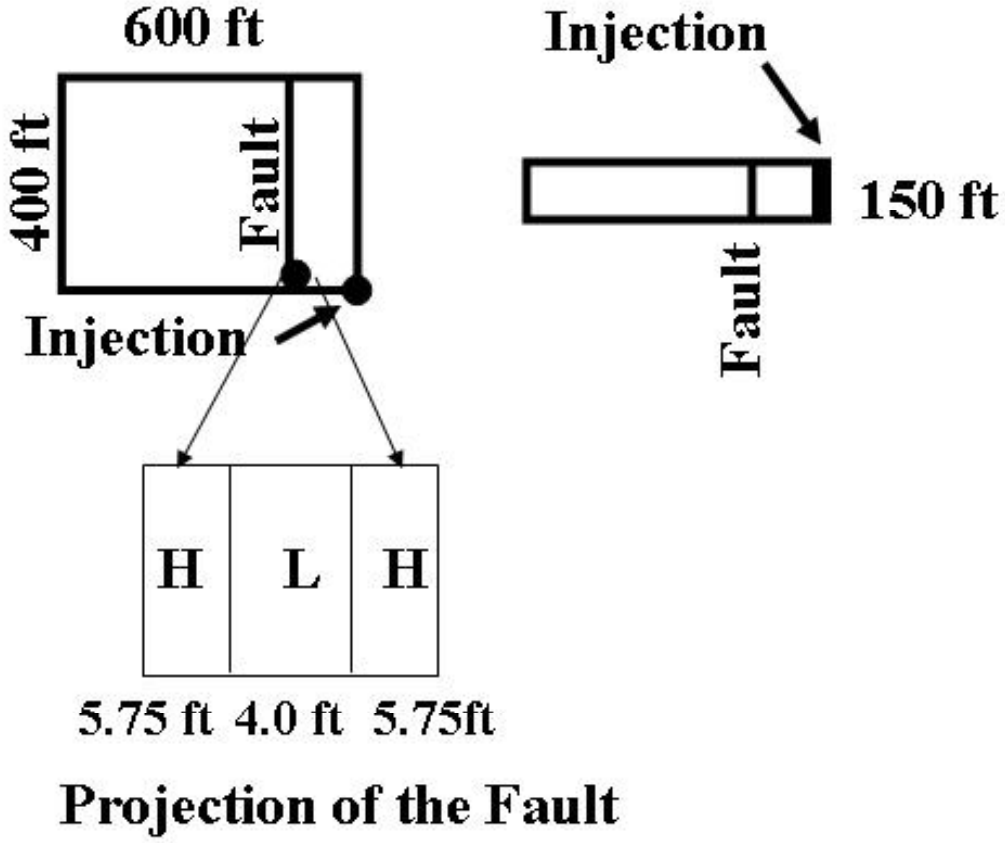

Figure 8.18. Reservoir model design

Table 8.7. Permeability and Porosity properties of the host rock and fault, for the conduit barrier fault case, where md = milli Darcy, k = Permeability

Case	Permeability (md)	Porosity
Host Rock	500	20%
Low-k Fault	0.05	7%
High-k Fault	5000	22%

The weighed arithmetic mean represents the permeability of the fault where flow parallels the fault [38], [39], [40]. In this case:

$$k_{av} = \sum_{n}^{1} \frac{k_i h_i}{\sum h_i} \tag{8.1}$$

where k_{av} is the mean permeability, k_i is the permeability of the i-th fault component, and h_i is the thickness of the i-th component. For flow perpendicular to the fault, the weighed harmonic mean estimates the bulk permeability as:

$$k_{hm} = \frac{\sum_{n}^{1} h_i}{\sum_{n}^{1} \frac{h_i}{k_i}} \tag{8.2}$$

The computed equivalent permeabilities are anisotropic and are determined to be k1=0.193744 md, k2=3709.69000 md, and k3=3709.69000 md. Table 8.8 shows the dissolved and free Gas in Zone-1 of the reservoir volume for the High-Low-High fault, and the equivalent permeability cases.

Figures 8.19, 8.20, and 8.21 show the top and vertical views of dissolved CO_2 distribution for a H-L-H fault and the effective permeability fault after 100 days and 500 days.

Analysis of individual volumes of the reservoir is done to determine how the gas (dissolved and free gas) is distributed throughout the entire reservoir like in the previous sections. Figures 8.19 and 8.20 illustrate the dissolved gas distributions in all three zones as described in Chapter 10.2. The two cases are the high-low-high permeability fault case and equivalent permeability cases.

The fluid flow behavior of Case-2 that is the equivalent permeability case behaves closely to that of a deformation band fault scenario. In the previous section, we have seen that when increasing the number of features in the parallel to the fault (x-direction), flow is restricted and has the greatest impact on fluid flow. In Case-2, a case of anisotropy permeability, the behavior is more like that of a low permeability fault, where $k_x = 0.19$ is the dominant fault feature in this scenario.

Table 8.8. Dissolved and Free gas in Zone-1 of the reservoir volume for the High-Low-High Fault Case, and the Equivalent Permeability Case, where 'Diss'=Dissolved, 'H-L-H' = High-Low-High , 'Equi'=Equivalent, 'k' = Permeability, 'Ttl'=total, 'Diss'=dissolved

Case	Diss Gas (MMSCF)	Free Gas (MMSCF)	Ttl CO_2 (MMSCF)	% Diss Gas	% Free Gas	%of Ttl CO_2
H-L-H	21.68	12.22	33.9	63.95	36.05	67.8
Equi k	21.51	14.19	35.7	60.25	39.75	71.4

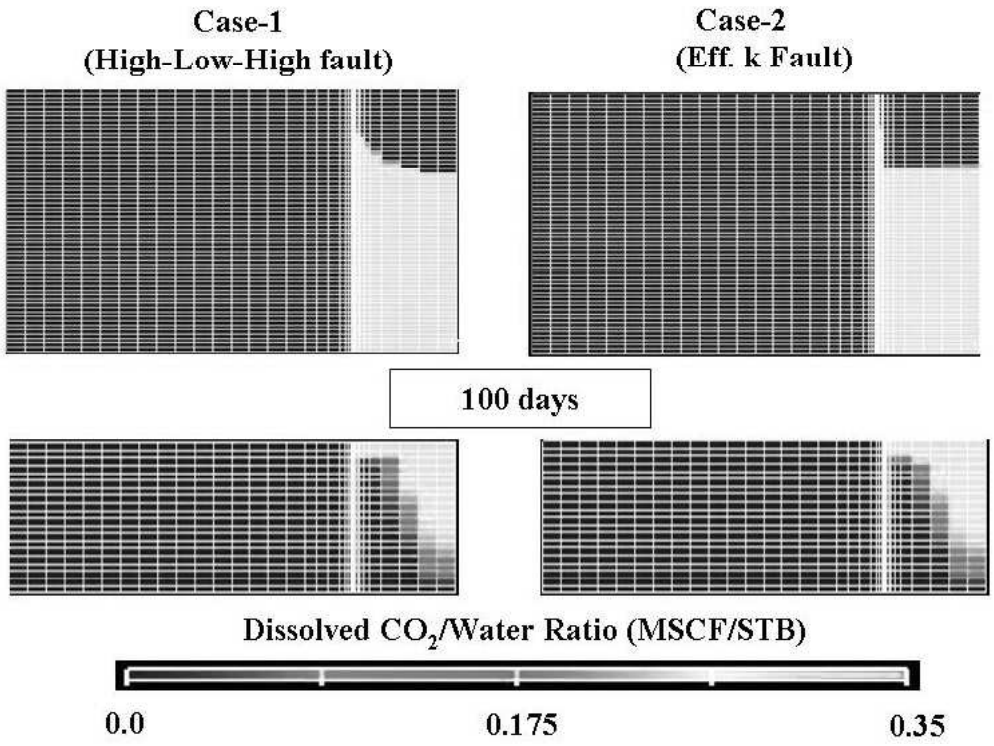

Figure 8.19. Dissolved CO2 distribution after 100 days

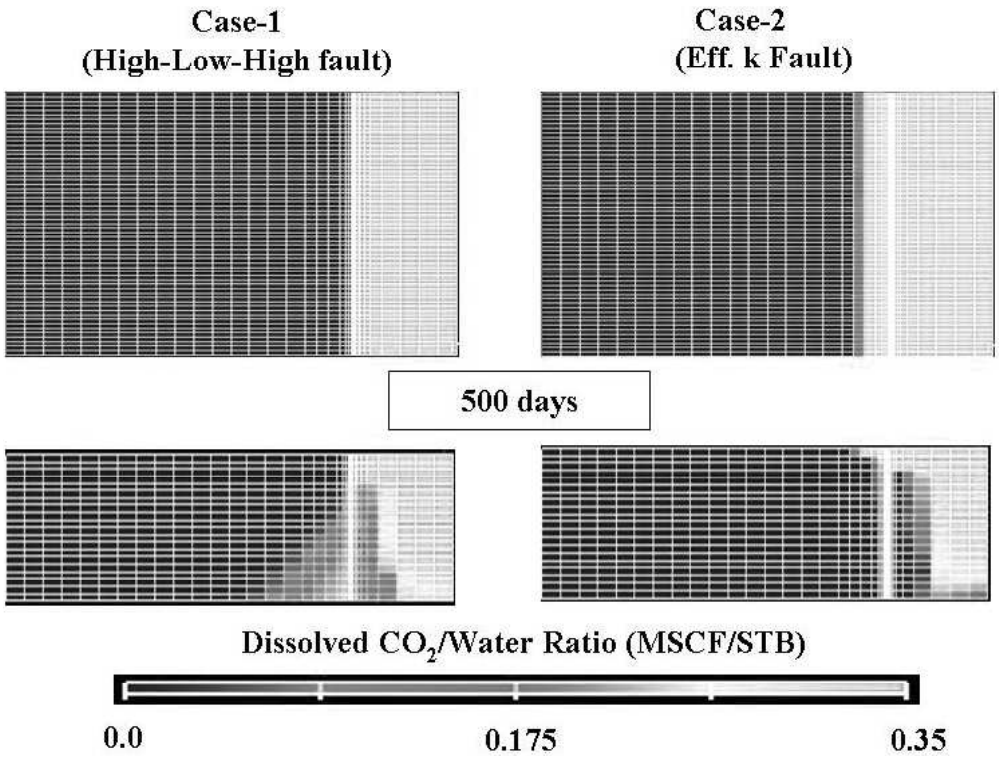

Figure 8.20. Dissolved CO2 distribution after 500 days

8.7 Larger reservoir model

To predict the long term fate of the injected CO_2 requires the use of a much larger model and coarser grid to achieve acceptable computing time. CO_2 is injected into the reservoir for 11 years and then the simulation is run until 30 years to illustrate the CO_2 migration in the reservoir. The two end member types of fault-affected sandstone dominated by fractures or deformation bands were analyzed and compared. Table 8.9 shows the permeability and porosity properties of the host rock and fault, for the larger reservoir case.

Figures 8.22 and 8.23 show the dissolved CO_2 distribution for all three cases after 11 and 30 years. Figures 8.24 and 8.25 illustrate the free CO_2 saturation after 11 and 30 years. The blue color represents initial CO_2 saturation, which is assumed to be zero. The results are very similar as observed in Section 8.1 after 11 years of injection.

The simulation results after 11 years of injection illustrate that the CO_2 bubble

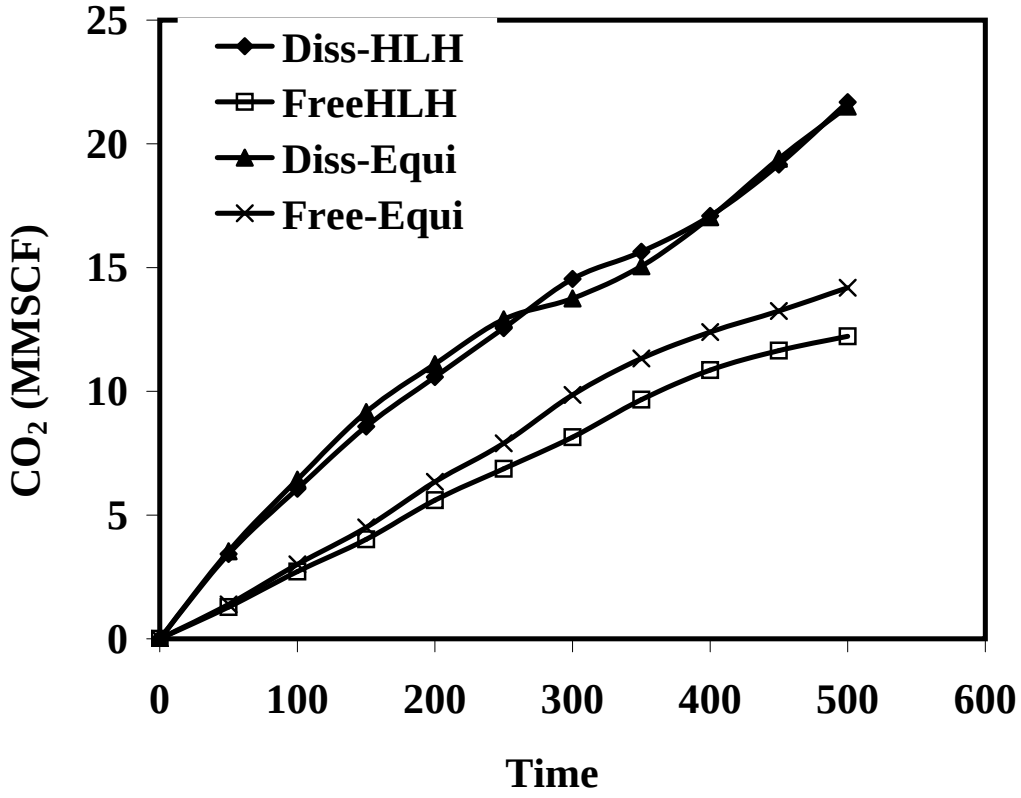

Figure 8.21. Dissolved and Free CO2 distribution in zone-1 of the reservoir volume where 'Diss'=Dissolved, 'H-L-H' = High-Low-High Fault Case, and 'Equi'=Equivalent Permeability Case

Table 8.9. Permeability and Porosity properties of the host rock and fault, for the larger reservoir case, where md = milli Darcy, k = Permeability

Case	Permeability (md)	Porosity
Host Rock	500	20%
Low-k Fault	0.05	7%
High-k Fault	50,000	25%

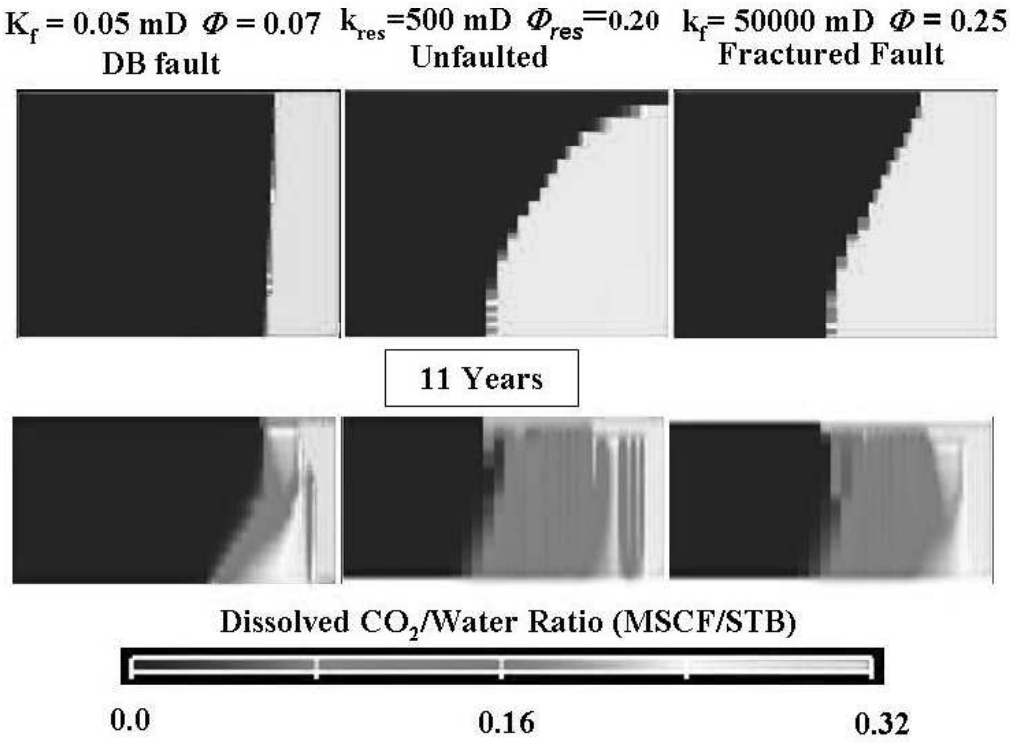

Figure 8.22. Dissolved CO_2 distribution after 11 years

increases in its lateral extension in the reservoir. After injection has stopped, the dissolution is the dominant mechanism resulting in shrinking of the bubble and the bubble gets slowly dissolved into the bottom layers. The importance of gravity effects is evident in the migration of the gas into the bottom layers of the reservoir.

After the injection has stopped, the pressure gradient that was driving the lateral migration quickly relaxes, and the buoyancy driven migration becomes dominant. This in particular allows for the vertical migration of the gas, which then brings the gas in contact with the larger reservoir volume, thereby increasing the proportion of dissolved gas.

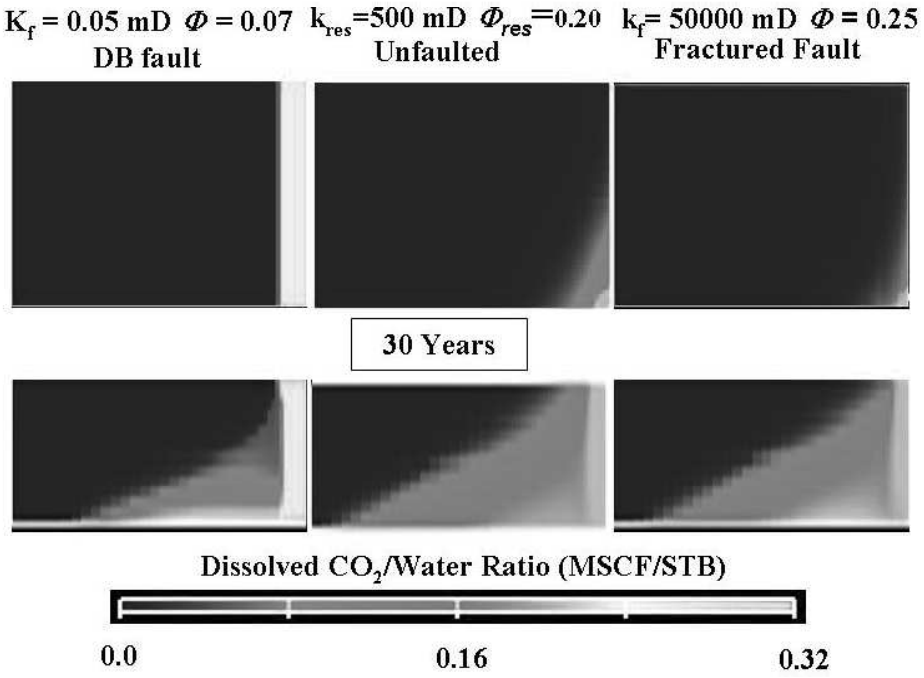

Figure 8.23. Dissolved CO_2 distribution after 30 years

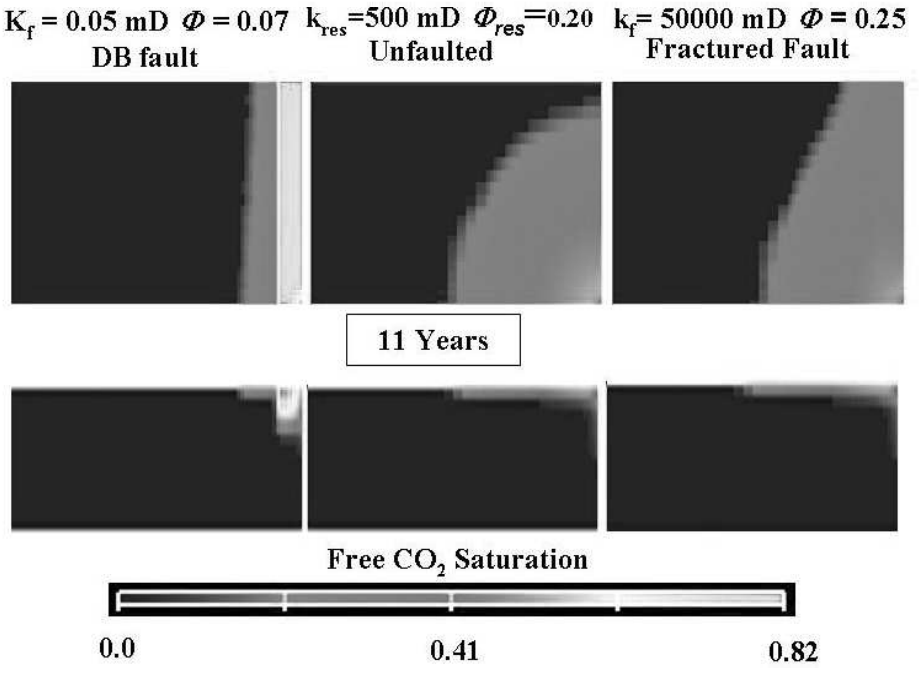

Figure 8.24. Free CO_2 saturation after 11 years.

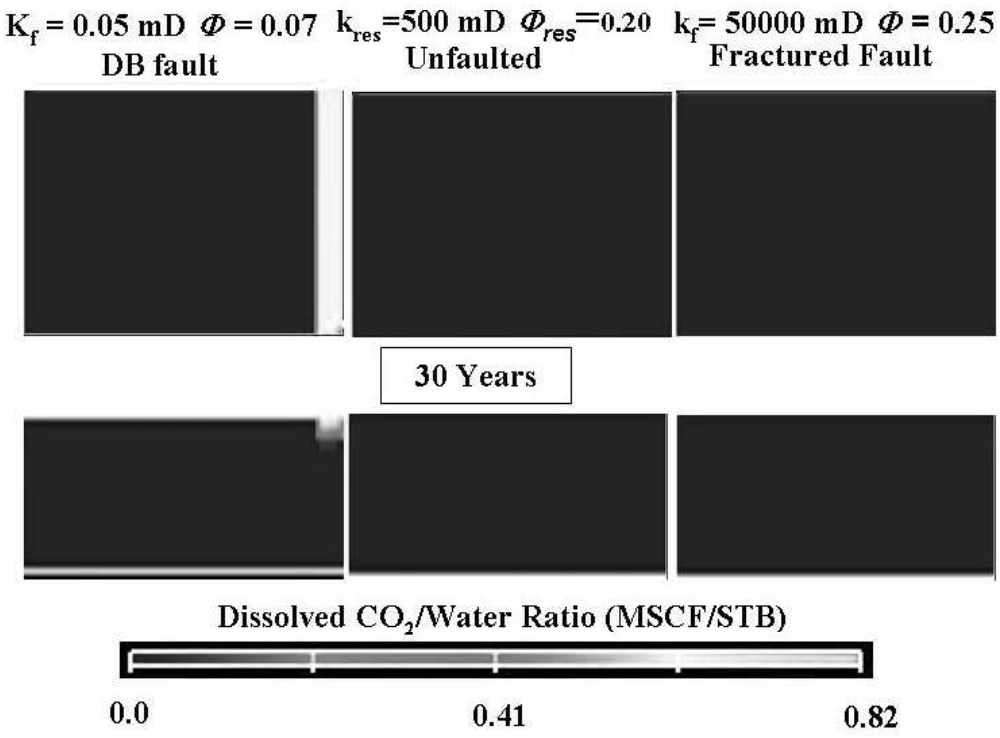

Figure 8.25. Free CO_2 saturation after 30 years.

CHAPTER 9

DISCUSSION

Faults can be important conduits for flow, barriers to flow, or combined barrier-conduit systems. Detailed analysis of various fault scenarios using reservoir simulations provides an insight into the CO_2 storage efficiency and the volumes of CO_2 sequestered. It is difficult to anticipate which type of structural feature will dominate fault-affected rock. In such circumstances, a broad range of uncertainty in permeability must be considered that recognizes the full range of fault-affected permeability. The two end member types of fault-affected sandstone are dominated either by fractures or deformation bands.

Table 9.1 shows the summary of the dissolved gas and free gas in all the simulation cases. The results from the reservoir simulations indicate that fault-related high permeability conduits within a sequestration aquifer closer to the injection well will have little/no impact on the CO_2 storage efficiency. When a fractured fault is encountered closer to the injection well, not much of the volume between them is fills up with CO_2; instead, it flows across the fault and sweeps the other portion of the reservoir. On the other hand, fault barriers in the target aquifer might lead to enhanced storage efficiency because the injected CO_2 is forced to more completely fill fault-bounded high-permeability sandstone compartment before significant CO_2 is transmitted across the fault. The amount of both the dissolved (59%) and free (41%) CO_2, in the compartment is higher when fault barriers are encountered. This region has reached maximum gas saturation and would not allow for any more dissolution of injected CO_2, hence resulting in more free gas in this scenario.

Computed pressure build-up curves help to establish situations where in situ pressure build-up curves obtained during the initial phases of injection will help

Table 9.1. Dissolved and Free Gas in zone-1 of the reservoir volume where 'Diss'=Dissolved, 'H-L-H' = High-Low-High Fault Case, 'Equi'=Equivalent Permeability Case, 'ttl'=total.

High and Low Permeability Faults without Seal

Case	Diss Gas (MMSCF)	Free Gas (MMSCF)	Ttl Gas (MMSCF)	% Diss Gas	% Free Gas	% Ttl CO_2
Unfaulted	16.45	4.65	21.1	77.97	22.03	42.2
DB filled fault	22.27	15.39	37.66	59.14	40.86	75.32
Fracture filled fault	17.75	3.89	21.64	82.02	17.98	43.28

to discriminate between high vs. low permeability of the fault-affected aquifer sandstone. This helps greatly in determining which type of structural feature dominates the rock.

Bottom hole pressure (BHP) builds up rapidly when fault barriers are encountered in a reservoir. Gas injection has to be stopped earlier because the reservoir is overpressured faster. An efficient strategy would be to inject CO_2 from a horizontal well. When horizontal wells are used in the DB fault case, the BHP dropped from 49.1% in the vertical well case to as low as 23.8%. This decrease of the BHP in the horizontal well case is because CO_2 can be transmitted between compartments by horizontal wells, thereby reducing the pressure build-up in the injection compartment.

Depending on the permeability structure of the high permeability fault network, significant CO_2 bypassing of aquifer rocks will result. In case of a fractured fault, 63.5% of the injected CO_2 has leaked into the upper layer, thereby a possibility for leakage into the atmosphere. On the other hand, in the deformation band fault, 89% of the CO_2 resided in the bottom layer. Thus, an efficient strategy would be to inject CO_2 from a horizontal well traversing the base of compartmentalized

sandstone. Thus, CO_2 can be transmitted between compartments by horizontal wells, while the fault barriers work to restrict the lateral leakage to the upper sections of each compartment.

Deformation bands are unlikely to form in sandstone with porosity less than 0.12, thus permeability reduction in fault-affected, lower porosity rock will occur as a consequence of (1) permeability reduction through geochemical alteration, (2) assimilation of clay minerals due to fault slip alternating sequences of sandstone and shale, or (3) direct juxtaposition of sandstone against lower permeability rock. Because these types of low-permeability barriers are likely more geochemically reactive than deformation band barriers, it will be important to resolve the mineralogical composition of these structural features in order to evaluate the potential for CO_2 saturated water to modify porosity or permeability of the fault-affected aquifer sandstone.

The lower porosity of the lower permeability sandstone rock cannot hold more CO_2, hence resulting in more free gas. Thus, higher porosity sandstone aquifers might be preferred sequestration targets in faulted systems where fractures have reduced impact on sequestration efficiency and deformation band barriers are more likely to develop.

In performing the numerical simulations of CO_2 injection, several assumptions are made regarding relative permeability relationships of unfaulted and fault affected sandstone. A comprehensive literature review yielded few data regarding these relationships for the CO_2-water systems. The results of several numerical sensitivity studies performed to assess the impact of uncertainity in knowing relative permeability relationships suggest that the distribution of free and dissolved CO_2 is affected by the residual water saturation (S_{wr}). As gas displaces formation water, the residual water will be saturated with CO_2, and so a greater S_{wr} value allows for more dissolved gas and less free gas. This clearly indicates the need for laboratory core flood measurements to reduce the uncertainty in the simulations.

The simulation results of the permeability anisotropy within the fault zone studies have shown that the number of features in the parallel to the fault (x-direction)

has the most impact on the distribution in case of deformation band type faults. Therefore, increasing the number of features in the parallel to the fault (x-direction), flow is restricted and has the greatest impact on fluid flow.

Complete dissolution of the injection carbon dioxide takes place, depending on the type of faults/fractures. The injected carbon dioxide migrates by gas trapping and dissolution in formation water. In the fractured fault case, the injected CO_2 is completely dissolved 30 years after injection has stopped, unlike when fault barriers are encountered. CO_2 storage efficiency depends on the permeability structure of the fault affected rock, porosity, and the type of injection strategy. These results have important implications for any sequestration site, as aeolian sandstones have many of the attributes required for a candidate sites.

Future work may be to focus on predicting the effects of capillary pressures on CO_2 injection. Also, predictions on the effects relative permeability curves will require laboratory experiments that determine realistic behavior of reservoir rock under in situ conditions. Research on the effects of CO_2 injection on capillary pressures may, for example, focus on predicting CO_2 storage capacity effects for longer time periods after injection.

CHAPTER 10

CONCLUSIONS

The primary objectives of this research effort were

1. To establish conditions at which carbon dioxide-oil systems formed a miscible displacement, and to determine the gravity effects so formed in 2-D studies by a variety of simulation techniques
2. To study the effects of complex faulting/fracturing on CO_2 sequestration in deep aquifers

The main conclusions that can be drawn from the phase equibria effects and the CO_2 sequestration, simulation aspects of this study are outlined below.

10.1 Phase equilibria effects

The success of the carbon dioxide miscible floods (over 90% of the carbon dioxide floods fall into this category) depends on the development of miscibility. Therefore, one of the logical questions that arose in the course of this research was, can the process of miscibility development be determined using numerical simulations?

1. Normalized Compositional paths obtained from numerical simulation studies indicate the compositional behavior in the reservoir, thereby the displacement mechanism the reservoir undergoes
2. Reservoir temperature and displacement pressure determine which mechanism will control the displacement
3. 1-D and 2-D studies have proven that the different layers in 2-D have the same behavior, indicating that the entire reservoir has the same phase behavior
4. The 2-D results indicate that the bottom layer in 2-D also undergoes the same phase behavior, but takes a longer time to achieve the type of displacement the top layer undergoes

5. This indicates that gravity has a little/no effect on the displacement mechanism
6. Recovery plots show that increase in pressure increases the recovery
7. WAG injection helps improve recovery and sweep efficiency of immiscible floods

10.2 CO_2 sequestration

A simple averaging approach is used to compute the equivalent porosity of the fault-affected rock. Greater than 10 through-going structural features per meter (deformation bands or fractures) in three orthogonal directions are required in a cubic meter of sandstone before the equivalent porosity of the sandstone is significantly affected. Adding 100 structural features in each direction yields an intensely damaged rock with correspondingly significant change in effective block porosity (increase of 0.02 with fractures and decrease of 0.05 with deformation bands). Because significant increase, or decrease, in the volume of pore space available for CO_2 sequestration is likely only to be found in limited regions immediately associated with faulting, the actual volume of fault-affected rock likely need not be considered when estimating the total volume available for sequestration.

A simple averaging approach is used to compute equivalent permeability of fault-affected rock. Adding more than 10 through-going structural features per meter (deformation bands or fractures) in three orthogonal directions to a cubic meter of sandstone yields equivalent permeability values ranging from less than $10e^{-14}(m^3)$ for deformation band dominated faults to greater than $10e^{-12}(m^2)$ for fracture dominated faults, regardless of the permeability of the unfaulted sandstone. The more intense the damage caused by faulting (e.g., the greater number of structural features), the wider the range in fault-affected permeability. Where fewer structural features are found, the equivalent permeability of the fault-affected rock depends largely upon the permeability of the unfaulted host rock.

The low-k fault zone exerts the greatest impact on the shape of the advancing CO_2 front and restricts the bulk of CO_2 (both dissolved and free) to the region

upstream of the fault barrier. In lower-permeability aquifers, high permeability fault zones will become more important as pathways for CO_2 to bypass unfaulted sandstone. In such situations, it will be important to determine an optimal injection rate that minimizes bypassing while still injecting at a desirable rate.

Although high-permeability fault conduits might lead to reduced sequestration efficiency, aquifer compartmentalization by low permeability fault barriers may lead to improved efficiency because the barriers restrict lateral CO_2 migration and maximize the volume of CO_2 that might be emplaced in each fault compartment. In such cases, an efficient sequestration strategy might involve injecting CO_2 from a horizontal well traversing the base of compartmentalized sandstone.

REFERENCES

[1] Gunter, W. D.; Perkins, E. H. *Energy Conversion and Management* **1993**, *11*, 941–948.

[2] Bachu, S.; Adams, J. J. *Energy Conversion and Management* **2003**, *44*, 3151–3175.

[3] Law, D. H. S.; Bachu, S. *Energy Conversion and Management* **1996**, *37*, 1167–1174.

[4] Perkins, E. H.; Gunter, W. D. *Aquifer Disposal of Carbon Dioxide. Hydrodynamics and Mineral Trapping;* Geoscience Publishing ltd: Canada, 1996.

[5] van der Meer, L. G. H. *Energy Conversion and Management* **1996**, *95*, 1155–1160.

[6] Pruess, K.; Xu, T.; Apps, J.; Garcia, J. *Society of Petroleum Engineers* **2001**, *13*, 16–17.

[7] Bachu, S.; Gunter, W. D.; Perkins, E. H. *Energy Converstion and Management* **1994**, *35*, 269–279.

[8] Holloway, S. *Annual Reviews of Energy and the Environment* **2001**, *26*, 145–146.

[9] Rathmell, J. J.; Stalkup, F. I.; Hassinger, R. C. *SPE-AIME Forty-Sixth Annual Fall Meeting* **1971**, *24*, 2–4.

[10] Metcalfe, R. S.; Yarborough, L. *SPE-AIME Fifth Symposium on Improved Methods for Oil Recovery* **1978**, *69*, 3–14.

[11] Orr, F. M.; Dinbdoruk, B.; Johns, R. T. *Industrial and Engineering Chemistry Research* **1995**, *34*, 2661–2669.

[12] Zhou, D.; Fayers, F. J.; Orr, F. M. *SPE/DOE Ninth Symposium on Improved Oil Recovery* **1994**, *64*, 6–9.

[13] Shyeh-Yung, J. G. J. *Society of Petroleum Engineers* **1991**, *26*, 12–19.

[14] Warner, H. R. *Society of Petroleum Engineers* **1977**, *19*, 264–273.

[15] Hendriks, C. A.; Blok, K. *Combustion and Flame* **1993**, *34*, 949–957.

[16] Wang, Y.; Orr, F. M. *Petroleum Science and Engineering* **2000**, *27*, 151–164.

[17] Weir, G. J.; White, S. P.; Kissling, W. M. *Energy Conversion and Management* **1995**, *36*, 531–534.

[18] Linderberg, E. *Energy Conversion and Management* **1997**, *38*, 235–240.

[19] McPherson, B. J. O. L.; Cole, B. S. *Journal of Geochemical Exploration* **2000**, *69*, 65–69.

[20] Schechter, R. S. *Oil Well Stimulation;* Prentice Hall: Englewood Cliffs, NJ, 1996.

[21] Bryant, S.; Saripalli, K. P. *Adv.Water Resources* **2000**, *54*, 40–46.

[22] Caine, J. S.; Evans, J. P.; Forster, C. B. *Geology* **1996**, *17*, 1025–1028.

[23] Brown, S. R.; Bruhn, R. L. *Journal of Geophysical Research* **1998**, *103*, 2489–2500.

[24] Forster, C. B.; Smith, L. *Water Resources Research* **1998**, *24*, 1011–1023.

[25] Forster, C. B.; Smith, L. *Journal of Geophysical Research* **1989**, *94*, 9439–9451.

[26] Forster, C. B.; Evans, J. P. *Geophysical Research letters* **1991**, *18*, 979–982.

[27] Lopez, D. L.; Smith, L. *Water Resources Research* **1996**, *132*, 3227–3235.

[28] Lopez, D. L.; Smith, L. *Water Resources Research* **1995**, *31*, 1489–1503.

[29] Caine, J. S.; Froster, C. B. *Geophysical Monograph* **1999**, *113*, 101–127.

[30] Johnson, J. W. *Science and Technology Review Lawrence Livermore National Laboratory* **2000**, *96*, 19–23.

[31] Freethey, G. W.; Cordy, G. E. *U.S. Geologic Survey* **1991**, *1411*, 118–119.

[32] Aydin, A. *Pure and Applied Geophysics* **1978**, *116*, 19–31.

[33] Weigel, J. F. *U.S. Geologic Survey Water-Resources Investigation Report* **1987**, *34*, 68–69.

[34] Cordova, R. M. *Utah Department of Natural Resources, Technical Publication* **1978**, *61*, 66–67.

[35] Chester, F. J.; Logan, J. M. *Pure and Applied Geophysics* **1986**, *124*, 80–106.

[36] Shipton, K. Z.; Evans, J. P.; Robeson, K. R.; Froster, C. B.; Snelgrove, S. *AAPG Bulletin* **2002**, *86*, 863–883.

[37] Manzocchi, T.; Health, A. E.; Walsh, J. J.; Childs, C. *Petroleum Geoscience* **2002**, *8*, 119–132.

[38] Deustch. *SPE Formation Evaluation* **1989**, *4*, 343–348.

[39] Antonellini, M.; Aydin, A. *American Association of Petroleum Geologists Bulletin* **1994**, *78*, 355–377.

[40] Jensen, J. L.; Lake, L. W.; Corbett, P. W. M.; Goggin, D. J. *Prentice Hall PTR* **1997**, *62*, 390–391.

[41] van Genuchten, M. T. *Soil Science Society of America Journal* **1980**, *44*, 892–898.

[42] Corey, A. T. *Water Resources Publications* **1986**, *22*, 231–239.

[43] Drummond, S. E., Ed. *Boiling and Mixing of Hydrothermal Fluids: Chemical Effects on Mineral Precipitation;* Ph. D. Thesis, Pennsylvania State University: University Park, Pa, 1981.

[44] Duan, A.; Sun, R. *Chemical Geology* **2003**, *193*, 257–271.